Charles University

Faculty of Science

Study Program: Macromolecular Chemistry

Ing. Pavel Švec

Responsive Polymer Materials: From Light- to Thermo- and Redox-Responsive Systems

Responzivní polymerní materiály: Od fotoresponzivních po thermo- a redox-responzivní systémy

Doctoral Thesis

Supervisor: prof. Mgr. Martin Hrubý, Ph.D., DSc.

Institute of Macromolecular Chemistry,
Academy of Sciences of the Czech Republic, v.v.i.

Prague, 2024

The research reported in this thesis was supported by the Grant Agency of Charles University (project no. 766119 and project no. 602119).

Tato disertační práce vznikla za podpory Grantové agentury Univerzity Karlovy (projekt č. 766119 a projekt č. 602119).

Declaration:

I hereby declare that I have prepared this thesis independently and have cited all sources and literature used. Neither this thesis nor any substantial part of it has been submitted for the award of any other academic degree.

Prohlášení:

Prohlašuji, že jsem závěrečnou práci zpracoval samostatně a že jsem uvedl všechny použité informační zdroje a literaturu. Tato práce ani její podstatná část nebyla předložena k získání jiného nebo stejného akademického titulu.

Prague, 5th August 2024 Ing. Pavel Švec

Acknowledgement

I would like to express my sincere gratitude to everyone who directly or indirectly supported me in completing this doctoral thesis. First and foremost, I extend my deepest thanks to my supervisor, prof. Mgr. Martin Hrubý, Ph.D., DSc., for his invaluable assistance throughout my studies, his patience, and his profound enthusiasm not only for chemistry but also for science in general.

I am profoundly grateful to all my colleagues from the Department of Supramolecular Polymer Systems. In particular, I wish to acknowledge Ondřej Sedláček, Kristýna Kolouchová, and Ondřej Groborz for their assistance and enriching discussions. I am also thankful to all my friends who consistently and successfully managed to lift my spirits.

My deepest and heartfelt appreciation goes to my beloved partner, Lenka Loukotová, and to our baby son, Pavel, whose warm and endearing smile brings immeasurable joy to my life. Finally, I would like to thank my father Pavel; my mother Anna; and my brother Radim for their unwavering support.

Table of Contents

Abstract

This doctoral thesis focuses on the design, synthesis, and characterization of novel polymer materials responsive to physical and chemical stimuli. The presented findings will serve mainly for improving polymer-based drug-delivery systems (DDSs) and will help in advancing the development of future theranostics – materials combining therapeutic and diagnostic qualities into a single system. The emphasis is put on the bottom-up approach – design and synthesis of new small molecules, including light- and/or redox-responsive compounds, using light- and redox-responsive monomers for creating well-defined responsive polymers through controlled polymerizations, as well as controlling the exact monomer composition along polymer chains to achieve improved drug loading in micelle-like DDSs.

Pyrazinacenes are a specific type of heteroacenes formed from linearly-fused 1,4-pyrazine units. Pyrazinacenes are redox-active, strongly colored, fluorescent compounds that could be potentially used for designing new upconverting materials (*i.e.* conversion of lower energy photons to a higher energy photon) and their complexes with ruthenium could intercalate into DNA in a similar manner as the well-studied DNA probe/photoswitch $[Ru(bpy)_2dppz]^{2+}$. In this work, a novel and scalable one-pot synthesis of phenanthroline-fused pyrazinacenes from relatively inexpensive starting materials is described. The phenanthroline moiety was employed to form pyrazinacene complexes with Ru^{2+} ions and a straightforward *N*-alkylation strategy was developed for future conjugation of pyrazinacene upconversion materials with polymers.

In pursuit of light-responsive micelle-like DDSs, we have studied a model amphiphilic block copolymer based on poly[(2-nitrobenzyl)acrylate] (PNBA). UV-irradiation of the hydrophobic PNBA block led to its photodecomposition to poly(acrylic acid) resulting in polymer hydrophilization and micelle disassembly. We have described the first controlled polymerization of (2-nitrobenzyl)acrylate (NBA) using single-electron transfer living radical polymerization (SET-LRP) leading to polymers with narrow dispersity. We have successfully used the SET-LRP to prepare poly(ethylene oxide)-*block*-PNBA block copolymers, that formed micelle-like particles in aqueous environment and readily disassembled upon UV-irradiation. These block copolymers could serve as a model light-responsive excretable micellar DDSs.

We further moved to responsive fluorinated polymer systems of two different polymer classes – poly[(*N*-(alkyl)acrylamides] and poly(2-oxazolines) (POx). The described fluorinated polymers were designed as potential theranostic materials applicable for stimuli-responsive DDSs traceable *in vivo* by ^{19}F magnetic resonance imaging (^{19}F MRI). The studied thermo-/pH-responsive polymers based on poly[*N*-(2,2-difluoroethyl)acrylamide] (PDFEA) have demonstrated both excellent biocompatibility and highly favorable ^{19}F MRI imaging properties. Furthermore, we have successfully prepared thermo-/redox-responsive micelle-like PDFEA copolymer systems by incorporating ferrocene (Fc) moieties into the PDFEA thermoresponsive/hydrophobic block. The nanoparticles of such polymers disassembled in oxidative environment due to hydrophilization through formation of positively charged ferrocenium moieties (Fc^+). However, in the ferrocene-modified PDFEA polymers there was no significant change in ^{19}F MRI signal upon oxidation, and, therefore, ^{19}F MRI cannot be used for probing the redox state of similar DDSs.

To enable redox sensing, we have designed and synthesized two novel fluorinated ferrocene derivatives bearing an amino group, that was employed for amide coupling with the pending carboxyl groups of poly{[2-methyl-2-oxazoline]-*block*-[2-methyl-2-oxazoline-*stat*-2-(2-carboxyethyl)-2-oxazoline]} polymer. The copolymers decorated with fluorinated Fc moieties formed nanoparticles that disassemble upon oxidation through formation of Fc^+ and converting the diamagnetic fluorinated Fc moieties into paramagnetic Fc^+ changed the relaxation times and chemical shifts of the ^{19}F nuclei distinguishable by ^{19}F MRI.

This thesis also presents a synthesis of novel 2-aryl-2-oxazoline monomers and a first direct comparison of analogous amphiphilic gradient and block polyoxazolines containing 2-aryl-2-oxazoline monomers. DDSs with gradient polyoxazoline copolymers exhibited improved drug loading capacity and higher hydration/mobility of the micelle core (potentially favorable for ^{19}F MRI imaging and the design of new theranostic materials).

In summary, this doctoral thesis advances polymer materials designed to respond to physical and chemical stimuli, while focusing on polymer-based DDSs. Key achievements include the straightforward synthesis of new conjugable pyrazinacenes showing promise as materials for upconversion; the development of the first controlled polymerization of NBA and synthesis of PNBA-based copolymers that disassemble under UV light; and the introduction of pH-, thermo-, and redox-responsive fluorinated polymers for ^{19}F MRI imaging. Novel fluorinated ferrocene derivatives were employed to create redox-responsive polymer sensor systems traceable by ^{19}F MRI. New 2-aryl-2-oxazoline monomers were synthesized and superior properties of their gradient copolymers for DDSs were demonstrated. This work provides valuable insights and methodologies for future improvements in responsive polymer systems.

Keywords: Pyrazinacenes, poly[(2-nitrobenzyl)acrylate], light-responsive, poly[*N*-(2,2-difluoroethyl)acrylamide], ^{19}F MRI, thermoresponsive, ferrocene, redox-responsive, poly(2-alkyl-2-oxazoline), poly(2-aryl-2-oxazoline), drug-delivery systems.

Souhrn

Tato doktorská disertační práce se zaměřuje na návrh, syntézu a charakterizaci nových polymerních materiálů citlivých na fyzikální a chemické podněty. Předkládané výsledky mohou pomoci zejména k vylepšování systémů pro cílenou dopravu a řízené uvolňování léčiv („drug delivery systems“, DDSs) a k vývoji budoucích teranostik – materiálů kombinujících terapeutické a diagnostické aplikace v rámci jediného systému. Důraz je v této práci kladen zejména na „bottom-up“ přístup – tj. na návrh a syntézu nových malých molekul zahrnujících foto- a/nebo redoxně-responzivní sloučeniny, na využití foto- a/nebo redoxně-responzivních monomerů pro přípravu dobře definovaných responzivních polymerů pomocí kontrolovaných polymerací, a také na řízení monomerního složení podél polymerních řetězců pro zvýšení obsahu účinné látky v nanočásticových/micelárních DDSs.

Pyrazinaceny patří do skupiny heteroacenů, které jsou tvořeny lineárně spojenými 1,4-pyrazinovými jednotkami. Pyrazinaceny jsou redoxně aktivní, intenzivně barevné a fluorescenční sloučeniny, jež by v budoucnu mohly být využity pro nové upkonverzní materiály (tzn. přeměna dvou či více fotonů s nižší energií na foton s vyšší energií) a jejich komplexy s rutheniem by se mohly interkalovat do DNA podobným způsobem jako již používaná DNA próba $[Ru(bpy)_2dppz]^{2+}$. V této práci je prezentována nová robustní „one-pot“ syntéza pyrazinacenu s kondenzovaným fenanthrolinovým skeletem vycházející z dobře dostupných výchozích látek. Fenanthrolinový motiv v molekule takto připraveného pyrazinacenu byl dále využit pro tvorbu příslušných komplexů s Ru^{2+}. Také byla vyvinuta jednoduchá metoda spočívající v *N*-alkylaci pyrazinacenů, která umožňuje budoucí konjugaci upkonverzních materiálů na bázi pyrazinacenů s polymery.

Za účelem přípravy fotoresponzivních nanočásticových/micelárních DDSs jsme následně studovali modelový amfifilní blokový kopolymer založený na poly(2-nitrobenzyl)akrylátu (PNBA). UV záření rozkládá hydrofobní PNBA blok na poly(akrylovou kyselinu), což vede k hydrofilizaci systému a rozpadu micel. Uvádíme první řízenou polymerizaci (2-nitrobenzyl)akrylátu za pomoci „single-electron transfer“ živé radikálové polymerace (SET-LRP) vedoucí k vysoce uniformním polymerům. Pomocí SET-LRP jsme úspěšně připravili poly(ethylenoxid)-*block*-PNBA kopolymery tvořící micely/nanočástice podobné micelám, které se rychle rozpadají pod UV-zářením. Tyto blokové kopolymery by mohly posloužit pro modelové fotoresponzivní vyloučitelné DDSs.

Dále jsme se věnovali responzivním fluorovaným polymerním systémům založeným na dvou odlišných třídách polymerů – na poly[(*N*-(alkyl)akrylamidech] a poly(2-oxazolinech) (POx).

Zde popsané fluorované polymery byly navrhnuty jako potenciální teranostické materiály využitelné pro responzivní DDSs sledovatelné *in vivo* pomocí ^{19}F magnetické rezonance (^{19}F MRI). Studované termo-/pH-responzivní polymery založené na poly[*N*-(2,2-difluorethyl)akrylamid]u (PDFEA) vykazovaly výbornou biokompatibilitu a velmi vhodné fyzikální vlastnosti pro zobrazování ^{19}F MRI. Následně jsme také připravili termo-/redox-responzivní nanočásticový/micelární systém tvořený kopolymerem PDFEA obsahujícím ferrocenové skupiny v termoresponzivním/hydrofobním PDFEA bloku. Nanočástice skládající se z tohoto kopolymeru se v oxidačním prostředí rozpadají díky hydrofilizaci vznikajícími kladně nabitými ferroceniovými skupinami (Fc^+). U kopolymerů na bázi PDFEA obsahujících ferrocenové skupiny nicméně nedochází po oxidaci k pozorovatelným změnám v ^{19}F MRI signálu. U těchto systémů a podobných DDSs tedy není možné sledovat jejich redoxní stav pomocí ^{19}F MRI zobrazovacích metod.

Za účelem přípravy redoxně-responzivních polymerních DDSs s redoxním stavem monitorovatelným pomocí ^{19}F MRI jsme navrhli a syntetizovali dva nové fluorované deriváty ferrocenu nesoucí aminoskupinu. Obsažená aminoskupina posloužila pro amidový kaplink s volnými karboxylovými skupinami poly{[2-methyl-2-oxazolin]-*block*-[2-methyl-2-oxazolin-*stat*-2-(2-karboxyethyl)-2-oxazolinu]}. Takto připravené blokové amfifilní kopolymery s fluorovanými ferrocenovými jednotkami (Fc) tvoří ve vodném prostředí nanočástice, jež se po oxidaci rozpadají na unimery díky tvorbě nabitých Fc^+ skupin. Dále je díky transformaci diamagnetických Fc skupin na paramagnetické Fc^+ možné redoxní stav polymeru sledovat pomocí ^{19}F MRI vzhledem ke změně relaxačních časů a chemických posunů ^{19}F signálů.

Tato práce také předkládá syntézu nových 2-aryl-2-oxazolinových monomerů a první přímé srovnání analogických amfifilních gradientových a blokových oxazolinových kopolymerů obsahujících 2-aryl-2-oxazolinové monomery. DDSs na bázi gradientových polyoxazolinů vykazovaly vyšší obsah účinné látky a vyšší hydrataci/mobilitu jádra micely (potenciálně výhodná vlastnost pro ^{19}F MRI a návrh nových teranostických materiálů).

Tato disertační práce přináší nové poznatky v oblasti polymerních materiálů pro DDSs citlivých na vnější fyzikální a chemické podněty. Výsledkem této práce je jednoduchá syntéza nových konjugovatelných materiálů na bázi pyrazinacenů pro upkonverzní systémy a první kontrolovaná polymerizace NBA a syntéza kopolymerů na bázi PNBA, jejichž micely disociují působením UV záření. V rámci této práce jsou prezentovány nové pH-, termo- a redoxně-responzivní fluorované polymery pro zobrazování pomocí ^{19}F MRI. K vytvoření redoxně citlivých polymerních senzorových systémů sledovatelných pomocí ^{19}F MRI byly

použity nové fluorované deriváty ferrocenu. Dalším výsledkem je také syntéza nových 2-aryl-2-oxazolinových monomerů a prokázání výhodných vlastností jejich gradientových kopolymerů pro DDSs. Tato práce poskytuje cenné poznatky pro budoucí vylepšení responsivních polymerních systémů.

Klíčová slova: Pyrazinaceny, poly[(2-nitrobenzyl)akrylát], fotoresponsivní, poly[*N*-(2,2-difluorethyl)akrylamid], ^{19}F MRI, termoresponsivní, ferrocen, redoxně-responsivní, poly(2-alkyl-2-oxazolin), poly(2-aryl-2-oxazolin), cílená doprava a řízené uvolňování léčiv.

List of Abbreviations

AGET-ARP	activator generated by electron transfer atom transfer radical polymerization
AIBN	2,2′-Azobis(2-methylpropionitrile)
APS	ammonium peroxydisulfate
ARGET-ATRP	activator regenerated by electron transfer atom transfer radical polymerization
ATRP	atom transfer radical polymerization
Boc	*tert*-butyloxycarbonyl protecting group
bpy	2,2′-bipyridine
BuOPhOx	2-(4-butoxyphenyl)-2-oxazoline
BuPhOx	2-(4-butyphenyl)-2-oxazoline
CAC	critical association concentration
Cbz	benzyloxycarbonyl protecting group
CMC	critical micelle concentration
CROP	cationic ring-opening polymerization
cryo-TEM	cryogenic transmission electron microscopy
CTA	chain transfer agent
CV	cyclic voltammetry
Đ	dispersity
D–A	donor-acceptor interaction
DADCP	2,3-diamino-5,6-dicyanopyrazine
DCM	dichloromethane
DDSs	drug-delivery systems
DFEA	*N*-(2,2-difluoroethyl)acrylamide
D_h	hydrodynamic diameter
DIPEA	*N*,*N*-diisopropylethylamine
DL	drug loading capacity
DLS	dynamic light scattering
DMF	*N,N*-dimethylformamide
DMSO	dimethyl sulfoxide
DNA	deoxyribonucleic acid
DOSY	diffusion-ordered NMR spectroscopy

DP	degree of polymerization
dppz	dipyrido[3,2-a:2',3'-c]phenazine
DSSC	dye-sensitized solar cell
EE	entrapment efficiency
EPR	enhanced permeance and retention effect
Fc	ferrocene
FcCEA	*N*-[2-(ferrocenylcarboxamido)ethyl]acrylamide
FID	free induction decay
FWHM	full width at half maximum
GSH	glutathione
GSSG	glutathione disulfide
GTP	group transfer polymerization
HEA	*N*-(*2*-hydroxyethyl)acrylamide
HIF-1α	hypoxia-inducible factor 1-α
HOMO	highest occupied molecular orbital
HPLC	high-performance liquid chromatography
ICAR-ATRP	initiators for continuous activator regeneration atom transfer radical polymerization
ICRTG-ATRP	initiators containing radically transferable groups atom transfer radical polymerization
ImPA	*N*-[3-(*1H*-imidazol-1-yl)propyl]acrylamide
ISET	inner sphere electron transfer mechanism
J-V	current density-voltage characteristic
LCROP	living cationic ring-opening polymerization
LCST	lower critical solution temperature
LED	light-emiting diode
LiHDMS	lithium bis(trimethylsilyl)amide
log*P*	logarithm of octanol-water partition coefficient
LRP	living radical polymerizations
LUMO	lowest unoccupied molecular orbital
MADIX	macromolecular design via the interchange of xanthates
Me$_6$TREN	tris[2-(dimethylamino)ethyl]amine
MeOTs	methyl 4-methylbenzenesulfonate

MeOx	2-methyl-2-oxazoline
MestOx	2-(3-methoxy-3-oxopropyl)-2-oxazoline
MLCT	metal-to-ligand charge-transfer
M_n	number average molar mass
MR	magnetic resonance
MRI	magnetic resonance imaging
mRNA	messenger ribonucleic acid
MRS	magnetic resonance spectroscopy
MTT	3-(4,5-dimethylthiazol-2-yl)-2,5-diphenyltetrazolium bromide
MU	monomeric unit
M_w	mass average molar mass
MW	microwave radiation
NBA	(2-nitrobenzyl)acrylate
NHDF	normal human dermal fibroblast
NMP	nitroxide-mediated radical polymerization
NP	nanoparticle
OFET	organic field-effect transistor
OLED	organic light-emitting diode
OSET	outer sphere electron transfer
PAP	poly[(*N*-acryloyl)pyrrolidine]
PBS	phospate-buffered saline
PC3	human prostate cancer cell line
PDEA	poly[(*N*,*N*-diethyl)acrylamide]
PDFEA	poly[*N*-(2,2-difluoroethyl)acrylamide]
PEG	poly(ethylene oxide)
PEO	poly(ethylene oxide)
PhOx	2-phenyl-2-oxazoline
PHPMA	poly[*N*-(2-hydroxypropyl)methacrylamide]
pK_a	acid dissocitation constant
PMeOx	poly(2-methyl-2-oxazoline)
PNBA	poly[(2-nitrobenzyl)acrylate]
PNIPAM	poly[(*N*-isopropyl)acrylamide]
POx	poly(2-oxazolines)

PRE	paramagnetic relaxation enhancement
PyBOP	(benzotriazol-1-yloxy)tripyrrolidinophosphonium hexafluorophosphate
RAFT	reversible addition–fragmentation chain transfer polymerization
RDRP	reversible deactivation radical polymerization
ROMP	ring-opening metathesis polymerization
ROS	reactive oxygen species
SARA-ATRP	supplemental activator and reducing agent atom transfer radical polymerization
SARS-CoV-2	severe acute respiratory syndrome coronavirus 2
SEC	size-exclusion chromatography
SET-LRP	single-electron transfer living radical polymerization
SI	supporting information
SRMP	stable-radical-mediated polymerization
T_1	spin–lattice relaxation time
T_2	spin-spin relaxation time
T_2^*	apparent transverse relaxation time
T_{CP}	cloud point temperature
TCSPC	time correlated single photon counting
TFA	trifluoroacetic acid
TFT	thin-film transistor
T_{g}	glass-transition temperature
THF	tetrahydrofuran
TMBQ	trimethyl-locked benzoquinone
TMM-LRP	transition-metal-mediated living radical polymerization
UCST	upper critical solution temperature
UTE	ultrashort echo time
UV	ultraviolet radiation
vis	visible light

List of Publications and Conference Contributions

Publications Included in This Thesis

1. Švec, P.; Webre, W.; Richards, G.; Labuta, J.; Wakayama, Y.; Miklík, D.; Karr, P.; Mori, T.; Ariga, K.; D'Souza, F.; Hill Jonathan, P., Phenanthroline-fused Pyrazinacenes: One-pot Synthesis, Tautomerization and a Ru(II)(2,2'-bpy)2 Derivative. *Eur. J. Inorg. Chem.* **2018**, 2541-2548. **Times Cited: 4; IF = 2.58.**

2. Sedláček, O.; Filippov, S. K.; Švec, P.; Hrubý, M., SET-LRP Synthesis of Well-Defined Light-Responsible Block Copolymer Micelles. *Macromol. Chem. Phys.* **2019**, *220* (19), 1900238. Times **Times Cited: 10; IF = 2.34.**

3. Kolouchová, K.; Jirák, D.; Groborz, O.; Sedláček, O.; Ziolkowska, N.; Vít, M.; Šticová, E.; Gálisova, A.; Švec, P.; Trousil, J.; Hájek, M.; Hrubý, M., Implant-forming polymeric ^{19}F MRI-tracer with tunable dissolution. *J. Control. Release* **2020**, *327*, 50-60. **Times Cited: 21; IF = 9.78.**

4. Kolouchová, K.; Groborz, O.; Černochová, Z.; Škárková, A.; Brábek, J.; Rosel, D.; Švec, P.; Starčuk, Z.; Šlouf, M.; Hrubý, M., Thermo- and ROS-Responsive Self-Assembled Polymer Nanoparticle Tracers for ^{19}F MRI Theranostics. *Biomacromolecules* **2021**, *22* (6), 2325-2337. **Times Cited: 26; IF = 6.98.**

5. Švec, P.; Petrov, O. V.; Lang, J.; Štěpnička, P.; Groborz, O.; Dunlop, D.; Blahut, J.; Kolouchová, K.; Loukotová, L.; Sedláček, O.; Heizer, T.; Tošner, Z.; Šlouf, M.; Beneš, H.; Hoogenboom, R.; Hrubý, M., Fluorinated Ferrocene Moieties as a Platform for Redox-Responsive Polymer ^{19}F MRI Theranostics. *Macromolecules* **2022**, *55* (2), 658-671. **Times Cited: 9; IF = 5.46.**

6. Loukotová, L.; Švec, P.; Groborz, O.; Heizer, T.; Beneš, H.; Raabová, H.; Bělinová, T.; Herynek, V.; Hrubý, M., Direct Comparison of Analogous Amphiphilic Gradient and Block Polyoxazolines. *Macromolecules* **2021**, *54* (17), 8182-8194. **Times Cited: 15; IF = 6.06.**

Publications not Included in This Thesis

7. Groborz, O.; Kolouchová, K.; Pankrác, J.; Keša, P.; Kadlec, J.; Krunclová, T.; Pierzynová, A.; Šrámek, J.; Hovořáková, M.; Dalecká, L.; Pavlíková, Z.; Matouš, P.; Páral, P.; Loukotová, L.; Švec, P.; Beneš, H.; Štěpánek, L.; Dunlop, D.; Melo, C. V.; Šefc, L.; Slanina, T.; Beneš, J.; Van Vlierberghe, S.; Hoogenboom, R.; Hrubý, M. Pharmacokinetics of

Intramuscularly Administered Thermoresponsive Polymers. *Adv. Healthc. Mater.* **2022**, *11* (22), 2201344. **Times Cited: 7; IF = 10.0.**

8. Miklík, D.; Fatemeh Mousavi, S.; Burešová, Z.; Middleton, A.; Matsushita, Y.; Labuta, J.; Ahsan, A.; Buimaga-Iarinca, L.; Karr, P. A.; Bureš, F.; Richards, G. J.; Švec, P.; Mori, T.; Ariga, K.; Wakayama, Y.; Morari, C.; D'Souza, F.; Jung, T. A.; Hill, J. P., Pyrazinacenes exhibit on-surface oxidation-state-dependent conformational and self-assembly behaviours. *Comm. Chem.* **2021**, *4*, 29. **Times Cited: 10; IF = 7.21.**
9. Kolouchová, K.; Lobaz, V.; Beneš, H.; de la Rosa, V. R.; Babuka, D.; Švec, P.; Černoch, P.; Hrubý, M.; Hoogenboom, R.; Štěpánek, P.; Groborz, O., Thermoresponsive properties of polyacrylamides in physiological solutions. *Polym. Chem.* **2021**, *12* (35), 5077-5084. **Times Cited: 13; IF = 5.36.**
10. Švec, P.; Nový, Z.; Kučka, J.; Petřík, M.; Sedláček, O.; Kuchař, M.; Lišková, B.; Medvedíková, M.; Kolouchová, K.; Groborz, O.; Loukotová, L.; Konefał, R. Ł.; Hajdúch, M.; Hrubý, M., Iodinated Choline Transport-Targeted Tracers. *J. Med. Chem.* **2020,** *63* (24), 15960-15978. **Times Cited: 4; IF = 7.45.**
11. Groborz, O.; Poláková, L.; Kolouchová, K.; Švec, P.; Loukotová, L.; Miriyala, V. M.; Francová, P.; Kučka, J.; Krijt, J.; Páral, P.; Báječný, M.; Heizer, T.; Pohl, R.; Dunlop, D.; Czernek, J.; Šefc, L.; Beneš, J.; Štěpánek, P.; Hobza, P.; Hrubý, M., Chelating Polymers for Hereditary Hemochromatosis Treatment. *Macromol. Biosci.* **2020,** *20* (12), 2000254. **Times Cited: 5; IF = 4.98.**
12. Reyes-Gutiérrez, P. E.; Amatov, T. T.; Švec, P.; Císařová, I.; Šaman, D.; Pohl, R.; Teplý, F.; Pospíšil, L., Helquats as Promoters of the Povarov Reaction: Synthesis of 1,2,3,4-Tetrahydroquinoline Scaffolds Catalyzed by Helicene-Viologen Hybrids. *ChemPlusChem* **2020,** *85* (10), 2211-2211. **Times Cited: 7; IF = 2.86.**
13. Brus, J.; Czernek, J.; Hrubý, M.; Švec, P.; Kobera, L.; Abbrent, S.; Urbanova, M., Efficient Strategy for Determining the Atomic-Resolution Structure of Micro- and Nanocrystalline Solids within Polymeric Microbeads: Domain-Edited NMR Crystallography. *Macromolecules* **2018,** *51* (14), 5364-5374. **Times Cited: 17; IF = 6.00.**
14. Kostiv, U.; Lobaz, V.; Kučka, J.; Švec, P.; Sedláček, O.; Hrubý, M.; Janoušková, O.; Francová, P.; Kolářová, V.; Šefc, L.; Horák, D., A simple neridronate-based surface coating strategy for upconversion nanoparticles: highly colloidally stable ^{125}I-radiolabeled NaYF$_4$:Yb^{3+}/Er^{3+}@PEG nanoparticles for multimodal in vivo tissue imaging. *Nanoscale* **2017,** *9* (43), 16680-16688. **Times Cited: 59; IF = 7.23.**

15. Švec, P.; Hrubý, M., Radiopharmaceuticals for diagnostics and therapy of neuroendocrine tumors. *Chem. Listy* **2017,** *111* (1), 3-10. **Times Cited: 1; IF = 0.26.**

16. Hrubý, M.; Agrawal, K.; Policianová, O.; Brus, J.; Skopal, J.; Švec, P.; Otmar, M.; Džubák, P.; Štěpánek, P.; Hajdúch, M., Biodegradable system for drug delivery of hydrolytically labile azanucleoside drugs. *Biomedical Pap.* **2016,** *160* (2), 222-230. **Times Cited: 3; IF = 0.89.**

17. Severa, L.; Jirásek, M.; Švec, P.; Teplý, F.; Révész, Á.; Schröder, D.; Koval, D.; Kašička, V.; Císařová, I.; Šaman, D., Counterion-Induced Inversion of Conformer Stability of a [5]Helquat Dication. *ChemPlusChem* **2012,** *77* (8), 624-635. **Times Cited: 9; IF = 3.24.**

18. Vávra, J.; Severa, L.; Švec, P.; Císařová, I.; Koval, D.; Sázelová, P.; Kašička, V.; Teplý, F., Preferential Crystallization of a Helicene–Viologen Hybrid – An Efficient Method to Resolve [5]Helquat Enantiomers on a 20 g Scale. *Eur. J. Org. Chem.* **2011,** *2012* (3), 489-499. **Times Cited: 31; IF = 3.34.**

Patents:

1. Švec, P.; Hrubý, M.; Kučka, J.; Sedláček, O.; Petřík, M.; Nový, Z.; Hajdúch, M. Iodinated Analogs of Choline, Methods of Preparation Thereof, and Use Thereof as Medicaments. Patent WO2017148455A1, September 8, 2017.

2. Cígler, P.; Grantz-Šašková, K.; Vaněk, V.; Hejdánková, Z.; Loukotová, L.; Švec, P.; Priss, A.; Petrezselyova, S. Cyclohexane Lipidoids for Nucleic Acid Transfection and Use Thereof. 2023. Patent WO2023001323A1, January 26, 2023.

Contributions at International Conferences:

1. Švec, P.; Loukotová, L.; Vaněk, V.; Priss, A.; Diederichs, A.; Grantz-Šašková, K.; Cígler, P. XMaNs - Universal Lipid Nanoparticles for Nucleic Acid Delivery. *European Colloid & Interface Society Conference /36./ - ECIS 2022. Chania, Greece,* **4.9.-9.9.2022**; oral presentation. *Oral Abstract Book. Chania: European Colloid and Interface Society, 2022, p. 231.*

2. Švec P.; Kolouchová K.; Groborz O.; Sedláček O.; Hrubý M. Samouspořádané polymerní systémy nesoucí fluorované deriváty ferrocenu. *Zjazd chemikov /71./. Horný Smokovec, Vysoké Tatry, Slovakia*, **9.9.-13. 9.2019**; poster. *ChemZi. Roč. 15, 1 (2019), p. 206 (6Po16).*

3. Švec P., Nový Z., Kučka J., Petřík M., Sedláček O., Hajduch M., Hrubý M. Radioiodinated Aromatic Choline Analog Tracers. *ACS National Meeting & Exposition /257./. Orlando, USA,* **31.03-04.04.2019**; poster. *Abstracts of Papers of the American Chemical Society (part: MEDI Graphical Abstracts). Orlando: American Chemical Society, 2019. MEDI-177.*

4. Švec P., Kučka J., Hrubý M., Nový Z., Petřík M., Hajdúch M. New Choline Transporter-Targeted Theranostics. *Meeting on Self Assembly Structures in Solution and at Interfaces /6./ - AutoOrg 2018. São Pedro, Brazil,* **7.-9.11.2018**; poster.

5. Švec P., Sedláček O., Gálisová A., Jirátová M., Jirák D., Hrubý M. Studium geometrie a kinetiky degradace injikovatelných dep na bázi poly(*N*-isopropylakrylamidu). *Zjazd chemikov /67./. Horný Smokovec, Vysoké Tatry, Slovakia*, **7.9.-11. 9.2015**; poster. *ChemZi. Roč. 11, 1 (2015), p. 160.*

1 Introduction

1.1 Polymer Materials in Biomedicine

The research in the field of biomedical polymer materials is driven not only by the ever-increasing clinical demand for modern therapies but also by pure scientific curiosity and a need to understand the properties and behaviors of biological systems. [1, 2] These scientific efforts already account to a well-documented therapeutic potential and clinical applications of drug-delivery systems, [3, 4] polymer-coated biomaterials, [5] tissue engineering scaffolds, [6, 7] and wound dressings. [8, 9] The recent approval of mRNA vaccines for SARS-CoV-2 has also rekindled interest in the development of polymers as non-viral gene delivery platforms. [10, 11] This doctoral thesis discusses polymer systems responsive to physical and chemical stimuli – including not only the preparations of such well-defined polymers through controlled polymerizations but also the synthesis and design of novel light-sensitive and redox-sensitive small molecules and design and synthesis of new monomers.

1.1.1 Self-Assembly in Nature

Molecular self-assembly is prevalent in nature. [12] The programmed assembly of molecular structures requires information[13, 14] that controls the reproducible formation of a particular structure selected from countless possibilities. [15]

Protein synthesis inside living cells is a prime example of two distinct assembly strategies employed by living organisms. These strategies are different in the way they use and store the necessary information. With one approach, information is stored in a blueprint (in this case DNA) and is executed by an external agent (ribosome translating the primary structure of a protein synthesized from “incomplex” amino acids). The second distinct approach uses the information stored in the system components and enables spontaneous physico-chemical processes that lead to three-dimensionally ordered structures (spontaneous protein folding or self-assembly and formation of *e.g.,* protein-protein complexes - disregarding the role of chaperones). [15]

Self-assembly employs the information coded into the individual building blocks (*e.g.*, in their shape, charge, hydrophobicity, *etc.*) that determine the nature of interactions among the single components. The building block design in this way pre-determines the properties and functions of the self-assembled system. [16] However, it is important to distinguish between self-assembly and self-association in its broader meaning. [17] Self-associated phases held together by noncovalent interactions may exhibit rather low organization. The components of a self-assembled system must be mobile to reach their steady-state positions, where attractive and repulsive forces are balanced out. Molecular self-assembly employs noncovalent interactions (van der Waals, electrostatic, and hydrophobic interactions) or weak covalent interactions (hydrogen and coordination bonds). Equilibration between aggregated and non-aggregated states of the system is usually necessary to obtain ordered structures. [16] Further well-known examples of bottom-up self-assembly processes include double helix formation upon mixing complementary DNA strands, bilayer structures formed from phospholipids in aqueous environment (*e.g.*, cytoplasmic membrane) or the formation of highly ordered protein-protein complexes (*e.g.*, tetrameric hemoglobin[18]).

1.1.2 Self-Assembly of Polymer Amphiphiles

The self-organization of amphiphilic small molecules into 1-, 2- and 3-D structures has been studied for decades[19] and many different morphologies have been observed both in solutions and in bulk materials. [19] The common morphologies include spherical micelles ("classical micelles"), cylindrical micelles, lamellar structures and vesicles as well as bicontinuous structures. [12] In contrast to the simplistic view of classical micelles, the hydrophobic core of micelles is highly hydrated well beyond the first few carbons adjacent to the headgroup and contains non-polar pores and deep water-accessible wedges. [20]

The packing parameter, $p = V / (a_0 l_c)$ (V is the volume of the hydrophobic segment, a_0 is the head group area, and l_c is the hydrophobic segment length) is the main factor determining amphiphile aggregate morphology (Figure 1). [21] With $p < 1/3$, spherical micelles are formed; $1/3 < p < ½$ leads to cylindrical (wormlike) micelles; when $1/2 < p < 1$ lamellar or vesicular structures (*e.g.*, liposomes) are observed; and $p = 1$ produces planar lamellae. When $p > 1$, similar morphologies with but inverted arrangement of hydrophobic and hydrophilic groups can be observed (*e.g.*, micelles with a hydrophilic core and a hydrophobic surface). [12, 21]

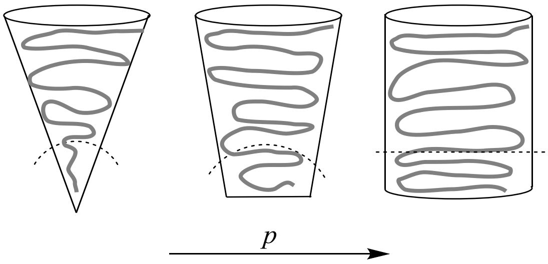

Figure 1. A representation of surfactant unimer shape based on its packing parameter.

Based on these principles, amphiphilic block copolymers[12] as well as asymmetric copolymers[22] (*e.g.,* gradient copolymers) form aggregates reminiscent of those of small-molecule amphiphiles. Amphiphilic surfactants now play a crucial role in drug-delivery. [23, 24] However, one of the fundamental challenges of micellar drug-delivery systems is that all conventional micelles disassemble into free unimers upon dilution. [23] Compared to small-molecule amphiphiles, polymer-based surfactants exhibit significantly greater tendency to form micelles (expressed as critical micelle concentration – CMC, or more generally as critical association concentration CAC) which in part helps to overcome the inherent instability of micellar drug-delivery systems. CAC is the lowest concentration of the amphiphile required to self-assemble into micelles /nanoparticles in solution. When the surfactant concentration reaches the CAC, both the bulk phase and interface become saturated with unimers and micelles /aggregates begin to form. [25] Lower CAC value indicates easier formation of micelles. Amphiphilic block copolymers typically exhibit low CAC $10^{-7} - 10^{-6}$ M (but can be even as low as $< 10^{-9}$ M) [24] due to the more thermodynamically favorable micellization compared to small-molecule surfactants (CAC on the order of $10^{-4} - 10^{-3}$ M). [26]

However, more recently, it was realized that in contrast to the case of small-molecule amphiphiles, block copolymer aggregates were often not so dynamic. [27] This fact stems from the high activation energy needed for the hydrophobic block to escape from the hydrophobic core. [22] This is especially true for polymer systems studied at temperatures below the glass-transition temperature of the hydrophobic block. [27] Aggregates that are kinetically "frozen" are therefore sometimes referred to as "nanoparticles" and the term micelle is used solely for systems in thermodynamic equilibrium. [27] The irreversibility of block copolymer association can be circumvented by preparing asymmetric (*e.g.*, gradient) copolymers with hydrophilic units incorporated into the hydrophilic block, which leads to a decrease of interfacial tension between the hydrophobic block and the solvent. [22]

1.1.3 Polymer Drug Delivery Systems

Since the first public use of the term "magic bullet" by Paul Ehrlich at a Harben Lecture in London in 1908, [28, 29] the major obstacles in delivery of small-molecule chemotherapeutics remain unchanged: optimizing drug clearance, improving water solubility, and passively or actively releasing the drug at its "target site". [30] Development of a new drug in the 21st century involves a substantial scientific effort and a very significant investment before the drug candidate can be approved for clinical use. [31] Only about 1 in 10 000 molecules is successfully introduced into clinics; after accounting for the costs of failed trials, the median capitalized research and development investment to bring a new drug to market was estimated at $1.1 billion. [32]

Sufficiently lipophilic small-molecule drugs (see Lipinski's rule of five[33]) are in principle able to rapidly diffuse across cell membranes and through many other biological barriers. [34] However, the capacity to permeate to the desired biological compartment[35] may still be hampered by low solubility in biological fluids. [36] Indeed, poor aqueous solubility low bioavailability of drug candidates determine key decisions on lead optimization during drug discovery[37] and represent a formidable hurdle for pharmaceutical industry. [30] The purpose of all (polymer) drug delivery systems (DDSs) is to improve therapeutic efficacy by increasing solubility, improving drug accumulation in the target tissue, improving patient compliance, reducing off-target drug concentration, increasing circulation time (*i.e.*, altering many aspects of the small-molecule drug pharmacokinetics). [36] Polymer systems with their tunable physico-chemical properties potentially offer efficient shielding, transport, and specific release of the drug cargo. [30] The specific release of the drug cargo in supramolecular DDSs can be achieved for example through employment of stimuli-responsive polymer materials[30, 38, 39] (see chapter 1.1.4) and by active[40] or passive targeting (*e.g.*, by optimizing system size for targeting into specific immune cells[38] or utilizing tumor-specific phenomena such as enhanced permeance and retention effect – EPR [ref. 41, 42]).

Following the discovery of enhanced permeance and retention effect (EPR) by Maeda in the 1980s, [43] EPR was the first and most pursued strategy for passive targeting to the tumor environment. [42, 44] Briefly, EPR effect was proposed to be based on the hyperpermeable tumor vasculature allowing its enhanced permeability for large particles compared to healthy tissues (macromolecules, micelles, liposomes, and other objects large enough to avoid renal clearance). This hyperpermeability in combination with impaired tumor lymphatic drainage would elicit the accumulation of those particles in the tumor interstitial space (Figure 2). [44] Unfortunately, the easy-to-grasp concept of EPR led to a heavily oversimplified perception of tumor physiology by the scientific community. [44, 45] In this regard, EPR was viewed as the "magic bullet" for tumor treatment without the high systemic toxicity present in conventional therapies. These hopes led to billions of dollars being invested into countless projects and platform designs. [44, 46] However, these efforts have largely failed to translate into clinics and there are only as little as 17 nanomedicine cancer therapeutics approved by the authorities for human use.[47, 48] Only 14% of the nanomedicines reaching phase III clinical trials have been successful at demonstrating efficacy.[49, 50]

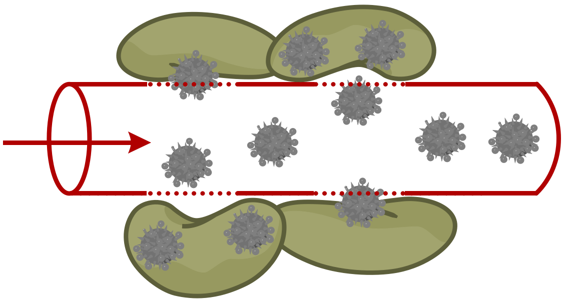

Figure 2. Highly fenestrated vascular epithelium as a part of the proposed EPR mechanism.

Indeed, while the EPR effect has been well documented in small animal models, clinical data is much less clear. In particular, murine tumor models are strikingly different from human cancers in many aspects - the rate of growth, the size relative to host, metabolic rates, host lifespan, and a different tumor microenvironment.[51] Recent studies have shown that EPR effect cannot be considered as a general strategy in cancer targeting due to high variability in nanoparticle accumulation (*e.g.*, biodistribution of ^{64}Cu-labeled liposomes[52]) in different tumor types.[51] It has now also been demonstrated that endothelial fenestration may not be responsible for the accumulation of nanoparticles in solid tumors but that the predominant mode of entry is an active process (transcytosis) through endothelial cells.[53, 54] The past enthusiasm of the scientific community about the EPR effect is clearly understandable. However, if nanoparticle DDSs are about to be included in the future cancer treatments, it is imperative to always justify the therapeutic gains for the target tumor type in a clinical setting.[44, 55]

1.1.4 Stimuli-Responsive Polymer Materials

The maintenance of biological function and sustenance of life requires specialized molecular assemblies and interfaces that provide distinct chemical behavior and structure, and which are responsive towards environmental stimuli.[56] Artificial systems based on synthetic polymers that partially mimic the behavior and function of biomacromolecular assemblies are being prepared and studied for a plethora of applications,[57] such as functional surfaces and biointerfaces;[58-61] polymer micro- and naoactuators[62-66] inspired by the action of muscles; particle or thin film sensing;[67, 68] and controlled drug-delivery and release systems.[69] Similarly to biomolecules, synthetic polymer materials can be designed to respond not only to a single environmental parameter but to be multi-stimuli responsive, *e.g.* temperature-light, pH-redox, pH-temperature, or even triple-responsive for example temperature-pH-redox responsive.[70, 71]

The responsiveness of synthetic polymer systems towards external stimuli is often achieved through an abrupt change in the features of the hydrophobic part of the molecule responsible for self-assembly. These features include for example hydrophobic-hydrophilic balance, conformation, and solubility. [70]

Stimuli-responsive polymer materials described in the literature primarily exploit lower critical solution temperature (LCST) or, less frequently, the upper critical solution temperature (UCST). [72, 73] Polymers that exhibit LCST transition phase sperate upon heating, whereas polymers possessing UCST transition phase separate upon cooling. However, UCST and LCST transitions are caused by different phenomena. [73, 74] According to the Flory-Huggins theory, a phase separation occurs only in systems with unfavorable interaction enthalpy between polymer segments and solvent molecules. The driving force behind the formation of a single phase is the polymer-solvent mixing entropy which at low polymer concentrations outbalances the positive enthalpic contribution. The phase separation in LCST is driven by a gain of overall entropy when the highly ordered water solvation shell of the polymer chain is released into bulk water with increasing temperature. In the case of UCST transition, the entropic contribution of polymer-solvent mixing gradually decreases with decreasing temperature and the unfavorable enthalpic term outweighs the entropic contribution. [73, 74] Arguably, one of the most prominent examples of thermoresponsive polymers with LCST close to human body temperature is the poly[(*N*-isopropyl)acrylamide] (PNIPAM). [75, 76] Some other examples of polyacrylamides exhibiting LCST close to body temperature include poly[(*N*-2,2-difluoroethyl)acrylamide] (PDFEA), poly[(*N*,*N*-diethyl)acrylamide] (PDEA), or poly[(*N*-acryloyl)pyrrolidine] (PAP). [77] It is noteworthy that LCST and UCST polymers can be also combined into diblock (or multiblock) copolymers exhibiting dual thermoresponsive behavior. [78, 79]

Light responsiveness of self-assembled polymer systems can be achieved *via* numerous chemical and physical processes caused by irradiation at a specific wavelength. These processes may be either reversible or irreversible and involve formation or cleavage of bonds, rearrangement reactions or cis–trans isomerism. [69, 80] For example, the hydrophobic block of an amphiphilic poly(meth)acrylate copolymer can be hydrophilized upon UV-light irradiation when the side chains of poly(meth)acrylate bear photodegradable hydrophobic ester groups such as, poly(2-nitrobenzyl acrylate) (PNBA), [81] poly(1-pyrenemethyl methacrylate) [82] or poly([7-(diethylamino)coumarin-4-yl]methyl methacrylate). [83] A straightforward example of photoisomerization reactions employed in light-responsive polymer systems is spiropyran photoisomerization from its closed hydrophobic form to a hydrophilic zwitterionic open merocyanine.[84] This isomerization reaction can be initiated by UV-light and reversed by visible light irradiation.[84, 85] Another well-known examples of photoswitch polymer systems are based on formation of polar cis-azobenzene induced by UV-light and reversed back to less polar trans-isomer by visible light.[86]

The polymer systems responsive towards changes in pH are polyelectrolytes designed to incorporate into the (partially) hydrophobic block basic or acidic functions whose ionization depends on pH.[87] These functional groups include for example carboxyl, phosphate, phosphonate, boronic acids, pyridine, amines and basic heterocycles such as imidazole. The pH-responsive polymers with basic functions are cationic polyelectrolytes under acidic conditions and polymers with acidic functions are anionic polyelectrolytes under basic conditions.[87, 88] Depending on the type of the pH responsive polymer, the generated cations or anions lead to electrostatic repulsion between the monomeric units of the polymer chain causing extension of coiled chains and change in conformation, hydrophilicity, and solubility in an aqueous solution.[89] Furthermore, the "nanobuffering effect"[90, 91] of pH-responsive polymers means that they are able to maintain a local pH range around their nanoscale systems which can differ from the environmental pH.[90] One of the notable applications of pH responsive materials is the class of Eudragit® polymers employed in selective dissolution of oral pharmaceutical formulations. Eudragit® excipients are anionic, cationic, or neutral copolymers of methacrylic acid and methacrylic co-monomers used for enteric coating and precise temporal release.[92]

Redox-responsive systems can be divided into two basic groups – oxidation-responsive and reduction-responsive polymers. This division predetermines the necessary toolbox of their chemistries. The polymer systems responsive to redox potential changes are inherently intriguing especially for biomedical applications because of their ability to distinguish differences in redox potentials between intracellular and extracellular environment.[17, 93] The strong reducing agent glutathione (L-glutamyl-L-cysteinyl-glycine; GSH) in its reduced form (in contrast with the oxidized form GSSG) is the most abundant low-molecular-mass thiol in animal and plant cells.[94, 95] Intracellular GSH concentrations can reach up to 10 mM, whereas extracellular levels in animals are one to three orders of magnitude lower.[94] Furthermore it has been shown that tumor tissues shows at least 4-fold higher concentrations of GSH compared with normal tissues.[96] Reduction-responsive polymers usually employ disulfide (−S−S−) or less commonly diselenide linkages (−Se−Se−) that cleave to free thiols and selenols upon reduction.[97] Other more exotic functional group sensitive towards reduction is for example trimethyl-locked benzoquinone (TMBQ).[98, 99]

Both physiological (cell signaling, immune response, and aging) and pathological (cancer) processes are associated with reactive oxygen species (ROS). ROS include hydroxyl radicals ($^{\bullet}OH$), alkyl peroxy radicals ($ROO^{\bullet}$), superoxide radicals ($^{\bullet}O_2^{-}$),hydrogen peroxide (H_2O_2), hypochlorous acid (HClO), and peroxynitrite ($ONOO^{-}$).[100-102] Cancer cells, in particular, may exhibit increased levels of ROS. These increased levels of ROS stabilize hypoxia-inducible factor 1-α (HIF-1α), [103-105] which is required for cell survival under the hypoxic conditions of solid tumor microenvironments and for rapid tumor neovascularization. [106] On the other hand, human neutrophils selectively generate HClO and ONOO– during oxidative burst and netosis[107, 108] (production of neutrophil extracellular traps), which are vital defense mechanisms against pathogens. [109]

Oxidation responsive polymers for biomedicine rely on the activity of ROS. [93] The chemical toolbox for design of oxidation-sensitive polymer systems includes poly(alkyl/aryl-sulfides) or poly(alkyl/aryl-selenides) which are oxidized to more hydrophilic sulfoxides and sulfones or selenoxides and selenones, respectively; [110] diselenides (both oxidation and reduction responsive); [111] boronic acid esters; [112, 113]; aromatic oxalates[114, 115] (oxidized to CO_2 and the corresponding phenols) and metallocenes[116] with the most prominent congener being ferrocene (oxidation to a more hydrophilic ferrocenium ion). [109, 117-119]

1.1.5 Pyrazinacenes and Upconversion Materials in Drug-Delivery Systems

Acenes are a class of polycyclic conjugated hydrocarbons composed of linearly fused benzene rings. [120] For polycyclic hydrocarbons of the same size, acenes exhibit the smallest energy difference between the highest occupied and lowest unoccupied molecular orbitals (HOMO–LUMO gap) [121, 122] and attract significant attention because of their applications in organic electronics. Acenes are most commonly exploited in devices such as organic field-effect/ thin-film transistors (OFETs/ TFTs) and organic light-emitting diodes (OLEDs) [123] but it has to be noted that pentacene and higher acenes usually suffer from chemical instability (*e.g.*, cycloaddition reactions, instability towards oxygen, and light-sensitivity) that increases with the number of fused benzene rings. [124-127] However, the reactivity of these compounds detrimental in optoelectronic applications can be of great value for designing stimuli-responsive materials based on acenes (polymer crosslinking or grafting, singlet oxygen sensing, and designing new drug delivery systems). [127]

Acene compounds are also employed in organic triplet-triplet annihilation upconversion[128] materials, *i.e.*, systems which convert two or more lower-energy photons into one higher-energy photon. Triplet-triplet annihilation was first discovered in anthracene solutions[129] and acene-based upconversion materials[130, 131] along with lanthanide upconversion materials are being developed for biosensing, drug delivery, and theranostics. [128, 132] Upconversion materials enable the use of lower energy photons for triggering processes that would otherwise require high-energy photons that are not within the biological transparency window[133] (*e.g.*, near-infrared light-triggered dissociation of poly(4,5-dimethoxy-2-nitrobenzyl methacrylate) micelles[134]).

Nitrogen substituted heteroacenes (*N*-heteroacenes[135]) have electronic properties different from acenes and enable additional possibilities for chemical modifications such as acid/base reactions, reduction to amines, or *N*-alkylation. [126] Pyrazinacenes are a specific group of *N*-heteroacenes that contain linearly fused 1,4-pyrazine units. [136, 137] In solid state, pentacene is a *p*-type semiconductor, whereas pyrazinacenes are promising candidates for *n*-type semiconductors with exceptionally high stability towards oxidation due to their high electron affinities. [126, 138] Pyrazinacenes are also being developed as potential fluorescent dyes for bioimaging and for example tetradecaazaheptacene chromophore was found to have an absorption and emission spectrum which overlaps with the biological transparency window (650-900 nm). [139]

In this thesis, we describe the one-pot synthesis of phenanthroline appended pyrazinacene from commercially available reagents. [137] The phenanthroline moiety in pyrazinacenes can be employed to form complexes with Ru^{2+} ions similarly to the well-studied $[Ru(bpy)_2dppz]^{2+}$ DNA molecular "light-switch" and intercalator. [137] This thesis also presents a straightforward *N*-alkylation strategy that was developed for potential future conjugation of pyrazinacene materials with polymers. [137] The *N*-alkylation approach presented in this thesis was now recently used for solubilization of pyrazinacenes in aqueous/ polar solvents through introduction of oligoethylene moieties to create pyrazinacene-based fluorescent colloidal systems. [140]

1.2 Synthesis of Highly Defined Polymers

Until the year 1920, many naturally occurring organic substances, such as cellulose, rubber or proteins, seemed difficult to categorize. The most eminent chemists in Europe had long proclaimed these materials consisted of small-molecule aggregates, loosely bound together by noncovalent interactions. [141] The "Age of Polymers" dawned more than 100 years ago, when the German chemist Hermann Staudinger published his seminal article "Über Polymerisation"

[142, 143], where he argued that polymer materials are composed of extremely large molecules linked by “standard” covalent bonds. The 1920 publication “Über Polymerisation” [142, 143] together with the Staundinger’s 1922 article “Über Isopren und Kautschuk” [144], where he introduced the term “Makromolekel” (macromolekule) for the first time, are considered as the founding stones of “macromolecular science” as a new field. [143]

The first ever purely synthetic polymers were prepared either by condensation reactions of small di(poly)functional molecules or by free radical polymerization of vinyl monomers. [145] Unlike biopolymers, for example most proteins, the chains of synthetic polymers prepared by conventional step-growth or chain polymerization reactions are not the same length – *i.e.*, such synthetic polymers have a highly non-uniform number of mers (repeating units). Eventually, polymer chemists realized that the properties of natural polymers (*e.g.*, silk, tendons–collagen) were in certain ways superior to synthetic polymer materials due to the nature’s ability to create polymers with (almost)identical chain lengths. However, to achieve this goal, new synthetic methods were needed. [145]

1.2.1 Living and Controlled Polymerizations

The term “living polymerization” that is now central to contemporary synthetic polymer chemistry was coined in 1956 by Szwarc, [146] who studied anionic styrene and isoprene (co)polymerization. [147] It denotes an ideal polymerization where an impurity-free monomer and initiator are converted under thermodynamically favorable conditions into polymer chains, with the same average growth rate for each chain and with no irreversible transfer or termination reactions. Thus, the produced polymer has a narrow molecular weight distribution, and the polymer end-groups are determined only by the choice of the initiating and terminating species. In this case, the phrase “thermodynamically favorable conditions” means that the entropically unfavorable joining of many monomer molecules together into just a few polymer chains must be outweighed by the enthalpic gain of converting double bonds to single bonds or by the release of ring strain through opening cyclic monomers. [148] Apart from the ability to prepare polymers with a narrow molecular weight distribution, living polymerization techniques equip polymer chemists with other powerful tools crucial for advanced polymer design: the synthesis of (multi)block copolymers (sequential monomer addition) and the high end-group fidelity of end-functionalized polymers (selective initiation and termination by appropriate reagents). [145]

The synthesis of polymers with precise functionalities, intricate architectures and well-defined length and compositions has now long been of great importance in polymer chemistry. [149]

However, only a few monomers polymerized by even fewer specific techniques fit the description of living polymerization almost perfectly. Nevertheless, a large number of other methods is now sufficiently close to living polymerization to be considered "good enough" and immensely useful for the synthesis of a plethora of polymer chain structures. [145, 148] The polymerizations which enable to at least partially achieve the main practical characteristics of living polymerizations, such as high polymer uniformity and end-group fidelity but which inherently include certain degree of termination and transfer reactions are sometimes also described as "living" – or more preferably "controlled polymerizations" (*e.g.*, controlled radical polymerizations). [150, 151] Living and controlled polymerization techniques currently comprise methods such as anionic, cationic, Ziegler–Natta, [152, 153] ring-opening metathesis (ROMP), group transfer (GTP), nitroxide-mediated radical (NMP), reversible addition–fragmentation chain transfer (RAFT), and supplemental activator and reducing agent atom transfer radical-/ single-electron transfer-living radical- (SARA-ATRP/ SET-LRP) polymerization. [148]

In this thesis, we have prepared well-defined polymers by means of SARA-ATRP/SET-LRP polymerization of acrylates, RAFT polymerization of acrylamides and by living cationic ring-opening polymerization (LCROP or CROP) of 2-alkyl/aryl-2-oxazolines. Therefore, we will discuss these methods in further detail.

1.2.2 Cationic Polymerization of 2-Alkyl/Aryl-2-Oxazolines

2-Oxazolines are commonly used in organic synthesis not only as protecting groups for carboxylic acids[154] but also as coordinating ligands in asymmetric catalysis, and activating moieties. [155] The LCROP of 2-oxazolines and 2-oxazines, two specific examples of living ring-opening polymerizations of heterocyclic monomers, [156] were reported for the first time in 1966[157, 158] – ten years after the seminal work on 'living' (anionic) polymerization by Swarc. [147] Poly(2-alkyl/aryl-2-oxazoline)s (POx) can be regarded as synthetic peptidomimetics or pseudo-peptides due to their structural analogy with polypeptides (isomeric polyamides). [159] There is a significant scientific effort dedicated to the use of POx in drug-delivery systems and biomedical applications, for example as functional and more versatile alternatives to poly(ethylene oxide) (PEG). [160]

Because most five- and six-membered rings are not strained, [161] the driving force behind LCROP of 2-oxazolines overriding the unfavorable entropy of polymerization is the formation of a tertiary amide that is comparably more stable than its parent cyclic imino ether. [160] The

LCROP of 2-oxazolines follows a classical chain-growth polymerization mechanism (Scheme 1).[160]

Scheme 1. Basic mechanism of LCROP of 2-oxazolines (termination side reactions omitted).[160]

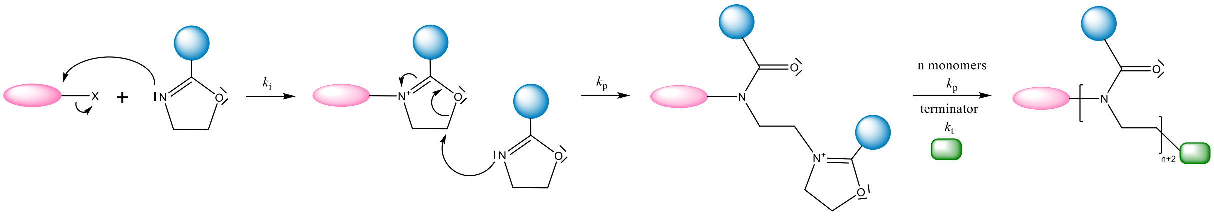

In the first reaction step, the electrophilic initiator (*e.g.*, alkyl sulfonates, alkyl/benzyl halides, Lewis acids, and oxazolinium salts) undergoes a nucleophilic attack by the nitrogen lone pair of the monomer, resulting in the formation of an oxazolinium cation (*initiation*). In the propagation step, the nitrogen lone pair of 2-oxazoline monomer attacks the cationic oxazolinium intermediate at the $-CH_2-$ group next to the oxygen atom, leading to the formation of an amide *via* ring-opening, while the living oxazolinium chain-end is regenerated. The livingness of the 2-oxazoline polymerization results in a narrow molar mass distribution and in low dispersity ($Đ$), provided that the initiation is fast. A β-elimination chain transfer reaction[162] and oxazolinium chain-end tautomerisation[163] become an issue for high molar mass POx causing divergence from the ideal living polymerization. However, if necessary, these chain transfer reactions can be nearly mitigated by lowering the polymerization temperature to 40 °C and increasing the reaction time to weeks, enabling the synthesis of low-dispersity polymers with molar mass up to 300 kDa.[163]

1.2.3 Controlled Radical Polymerization Methods (RAFT, ATRP)

The development and understanding of reversible deactivation radical polymerizations (RDRP), also called controlled or living radical polymerizations (LRP), has equipped polymer chemists with a control over polymer architecture comparable to traditional ionic living polymerizations.[148, 164, 165] However, at the same time RDRP modalities offer functional group and reaction conditions tolerance similar to conventional radical polymerizations.[166] The three major RDRP methods include stable-radical-mediated polymerization (SRMP: for example nitroxide-mediated polymerization - NMP[167]), reversible addition–fragmentation chain transfer polymerization (RAFT), and atom transfer radical–/ single electron transfer living radical polymerization (ATRP /SET-LRP).[168] The SRMP mechanism is the simplest of the three abovementioned RDRP methods: the propagating polymer radicals (P·) are reversibly deactivated through reaction with a stable radical (T·).[167] In this work, RAFT and ATRP /SET-LRP were the two RDRP methods chosen for the synthesis of well-defined acrylamide- and acrylate-based block copolymers and will, therefore, be discussed in further detail.

The roots behind the discovery of many living polymerization reactions can be traced directly to methods developed by synthetic organic chemists. The precise preparation of any given well-defined polymer calls for a single highly efficient reaction that can occur many times over without side reactions. This feature of living polymerizations is common also with the synthesis of complex organic molecules. Successful synthesis of intractable organic molecules usually requires efficient transformations of a broad spectrum of functional groups, and, at the same time, such transformations have to be orthogonal to a plethora of different functionalities present in complex organic molecules. [148] The discovery of RAFT polymerization (also called "macromolecular design via the interchange of xanthates" – MADIX; xanthate is the trivial name for an *O*,*S*-dithiocarbonate) was based on a friendly argument between two respected organic chemists (Sir D. H. R. Barton and A. L. J. Beckwith) about the exact mechanism behind the Barton−McCombie deoxygenation reaction. [169]

Barton−McCombie reaction involves deoxygenation of secondary alcohols via the reaction of their *S*-methyl xanthates with tris(*n*-butyl)stannane (Scheme 2). [169, 170] In the first 1975 Barton and McCombie report of the reaction, the $Bu_3Sn·$ radical was proposed to attack the thiono sulfur. [171] In 1984, based on electron paramagnetic resonance experiments, Barker and Beckwith suggested a different mechanism where the $Bu_3Sn·$ radical attacks the sulfide sulfur. [172] A mechanistic study was designed using cholestanyl-derived *S*-methyl and *S*-isopropyl xanthates to compete for 1 equivalent of stannane, where the potential attack on the thiono sulfur would not be affected by steric environment but a slower rate would be observed because of the bulkier *i*-Pr group, provided the reaction took place on the sulfide sulfur. [173] In this experiment, the *S*-isopropyl xanthate reacted unexpectedly much faster than *S*-methyl xanthate, and the product was surprisingly stannyl xanthate and propane instead of the expected cholestane resulting from reduction of cholestanyl radical by *n*-Bu_3SnH. [169, 173] This indicated a fast but reversible reaction of the stannyl radicals on the thiono sulfur. This observation was key in the discovery of RAFT /MADIX polymerization because at the time it was already known that carbon-centered radicals react with thionocarbonyl derivatives at a similar rate as do stannyl radicals. [169, 174]

Scheme 2. The mechanism of Barton-McCombie deoxygenation (reproduced from Zard, 2020 [ref. 169]).

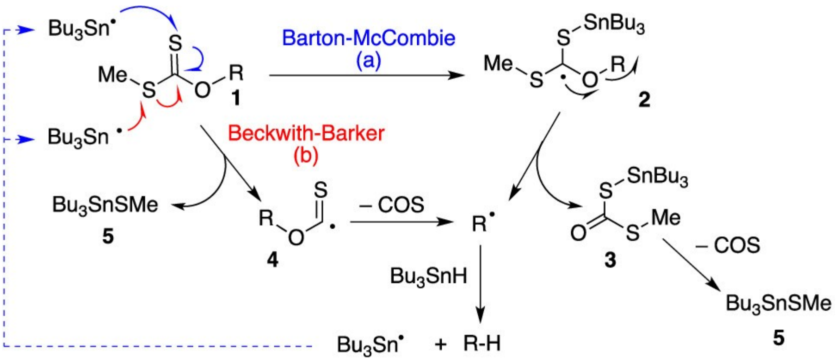

The mechanism of RAFT polymerization is depicted in Scheme 3. [175] The control over the molecular weight distribution in RAFT polymerization is enabled by a degenerative radical transfer mechanism that allows fast and efficient switching between active and dormant growing polymer chains. [168] This means the rate of addition/fragmentation at the functional chain end-group (typically thiocarbonylthio compounds such as dithioesters, dithiocarbamates, trithiocarbonates, and xanthates; Z–C(═S)S-R) is supposed to be higher than that of the propagation. Ideally, less than one monomer unit is added per activation cycle and all growing chains will necessarily have a similar degree of polymerization (DP) - that is, if we neglect radical-radical termination reactions. [175] Therefore, the overall process is a repeated insertion of monomers between the R- and Z–C(═S)S-groups of the RAFT agent and the theoretical DP is determined by the [Monomer]/[CTA] ratio (CTA – chain transfer agent). [168, 176] An often-overlooked key aspect of RAFT polymerization is that the number of dead chains resulting from bimolecular termination reactions in conventional RAFT directly corresponds to the amount of the used radical initiator; *i.e.*, number of radicals introduced into the system. [175]

Scheme 3. The mechanism of RAFT polymerization (reproduced from Perrier, 2017 [ref. 175]).

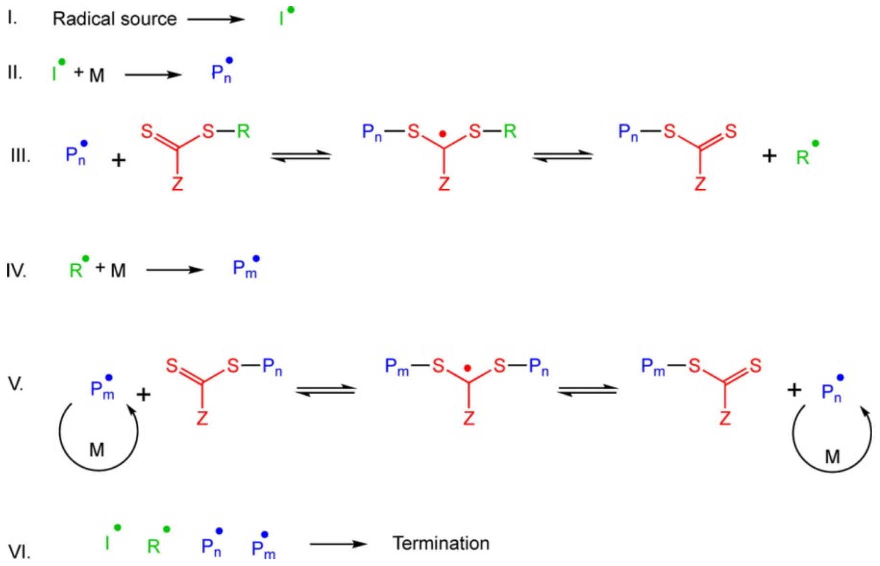

RAFT is applicable for most monomers employed in free radical polymerization with exception of monomers containing strongly nucleophilic substituents such as primary and secondary amines (although this can be at least partially remedied for example by protonating the amino group). [175] The RAFT literature mostly focuses on polymerization of (meth)acrylates, (meth)acrylamides, and styryl derivatives. However, RAFT can be used also for polymerization of more challenging monomers including *N*-vinylpyrrolidone and vinyl acetate or even for polymerization of ethylene under milder conditions[177] and a reduced extent of branching through the "backbiting" mechanism. [175] RAFT techniques allow for a straightforward synthesis of block copolymers by sequential RAFT polymerization or by thiocarbonylthio functionalization of a polymers prepared by other methods to form a macro-RAFT. Such pre-synthesized macro-RAFT agents are subsequently used in a standard RAFT polymerization. [178] RAFT chemistry also enables synthesis of polymers modified with a wide range of α- and ω-end functional groups with a relatively high end-group fidelity. [175, 176, 179]

Similarly to RAFT discovery, the roots of ATRP polymerization lie in a method originally developed by synthetic organic chemists – atom transfer radical addition (ATRA) catalyzed by Fe^{III} or Cu^{II} salts. [180-183] ATRP or more generally the so-called transition-metal-mediated living radical polymerization (TMM-LRP) was first described by Sawamoto[184] and Matyjaszewski[182] in 1994. [165] In TMM-LRP the radical center necessary for polymerization reaction is usually generated by a reversible reaction of an alkyl halide with a transition metal center. The first two metals described in TMM-LRP by Sawamoto[184] and Matyjaszewski[182] were ruthenium and copper, respectively. However, many other transition metals have been utilized as well, [185] namely iron, [186] nickel, [187] rhodium, [188] or the comparably less efficient palladium, [189] rhenium,

[190] and molybdenum. [191] Because of its low cost, large availability and ease of handling, copper is currently the most studied transition metal in TMM-LRP. When copper, rather than other metals is used, the process is typically termed ATRP. [165]

Scheme 4. The mechanism of ATRA addition and ATRP polymerization (reproduced from Matyjaszewski, 2016 [ref. 181]).

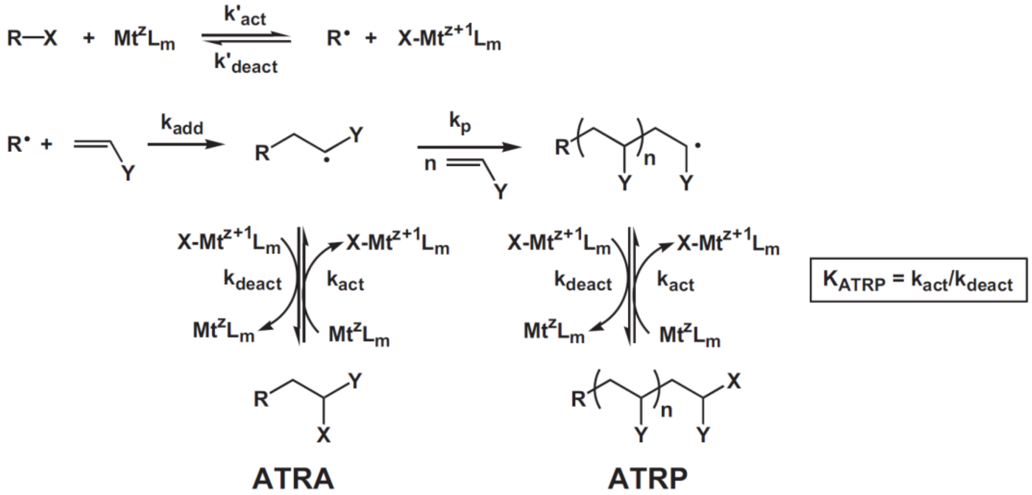

The general mechanism for ATRP is depicted in Scheme 4. [149, 181] In ATRP the radicals (the growing polymer centers), are created through a reversible redox reaction between a transition metal complex (M^n-L_y, where L is a ligand or the counterion) and an alkyl (pseudo)halide (R-X, P-X). This metal complex undergoes a single electron transfer with a simultaneous abstraction of a (pseudo)halide atom (X,) from an initiator R-X or dormant polymer chains P-X. Polymer chains (P·) are growing through the addition monomers to the generated radicals in the same manner as in a conventional free radical polymerization but they are reversibly deactivated back to P-X by a reaction with the higher oxidation state metal complex (X-M^{n+1}-L_y) . Termination reactions occur in ATRP mainly by radical disproportionation and coupling. However, in a properly optimized ATRP only a few percent of the growing polymer chains undergo termination. [149]

ATRP is considered to occur through an inner sphere electron transfer mechanism (ISET), where the formation of the radical and the higher oxidation state metal complex (deactivating species) proceed through the concerted homolytic atom transfer of the halide radical from the dormant species/initiator (R-X, P-X) to the activating species (M^n-L_y). [165] ISET mechanism has been pointed out by *ab initio* calculations to be more energetically favorable compared to the possible outer sphere electron transfer (OSET). [192] Interestingly, in “initiators containing radically transferable groups” ATRP (ICRTG-ATRP) a dithiocarbamate or dithiobenzoate can be used as the “(pseudo)halide” group in the initiator molecule R-X, which allows for an elegant synthesis of block copolymers through a sequential combination of ATRP and RAFT polymerization with ATRP non-polymerizable monomers (e.g., vinyl acetate). [193, 194] Since its discovery, also many other variations of ATRP methodology have been developed such as, reverse-ATRP, activator generated by electron transfer (AGET-ATRP), activator regenerated by electron transfer (ARGET-ATRP), initiators for continuous activator regeneration (ICAR-ATRP), and supplemental activation reducing agent (SARA-ATRP).

In 2006, more than 20 years after the discovery of ATRP polymerization, Percec and co-workers published the ultrafast synthesis of ultrahigh molar mass polymers from monomers containing electron-withdrawing groups by SET-LRP using elemental copper. [195] Percec proposed the polymerization process was similar to ATRP but with the key difference that Cu^0 was the activating species acting through outer sphere electron transfer mechanism (Scheme 5).

Scheme 5. The comparison of SARA-ATRP and proposed SET-LRP mechanism by Percec (reproduced from Konkolewicz, 2014 [ref. 196]).

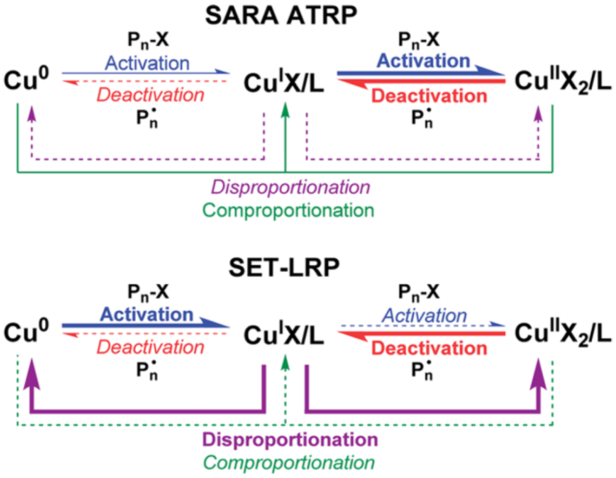

However, the literature debate regarding whether the mechanism of controlled living radical polymerization in the presence of Cu^0 is consistent with SET-LRP or with SARA-ATRP[197-199] is considerable. [196, 200-202] The accumulated evidence now strongly leans towards the SARA-ATRP mechanism but the Cu^0-mediated polymerization systems are very complex and the speciation of the present copper species is varied and rather complicated. [165, 202]

2 Aims of the Thesis

1. Development of a scalable one-pot synthetic procedure towards new phenanthroline-fused pyrazinacenes. Demonstration of the ability of the phenanthroline-fused pyrazinacenes to form complexes with Ru^{2+} and testing their photosensitizing properties. Development of a straightforward derivatization strategy for solubilization or conjugation of a phenanthroline-fused pyrazinacene with polymers.

2. Development of a controlled polymerization procedure for the preparation of well-defined poly[ethylene oxide-*block*-(2-nitrobenzyl)acrylate] (PEO-*block*-PNBA) that could serve as a model light-responsive drug-delivery system. Demonstration of the PEO-*block*-PNBA nanoparticle disassembly upon UV irradiation.

3. Studying the properties of thermoresponsive fluorinated copolymers based on poly[*N*-(2,2-difluoroethyl)acrylamide] and assessing their potential as ^{19}F MRI tracers and drug-delivery systems. Introduction of ferrocene moieties into PDFEA copolymers to induce redox responsivity.

4. Development of supramolecular fluorinated redox-responsive systems based on amphiphilic poly(2-alkyl-2-oxazolines) with their redox state traceable by ^{19}F MRI, namely:

Designing the structure of two fluorinated ferrocene compounds bearing a pendant amino group and possessing different hydrophobicities and redox potentials. Developing a multigram synthetic procedure towards these compounds.

Development of an amide coupling methodology for the block poly(2-alkyl-2-oxazolines) modified with different ferrocene moieties and synthesis of polymers with various fluorinated ferrocene contents.

Studying electrochemical properties of prepared polymers, nanoparticle formation and disassembly by oxidation, testing of ^{19}F MRI properties and probing the redox state by ^{19}F MRI.

5. Synthesis and development of a scalable multigram procedure towards two new 2-aryl-2-oxazoline monomers. Studying the corresponding gradient and block copolymers of 2-aryl-2-oxazolines with 2-methyl-2-oxazoline and comparing the drug loading capacity of their nanoparticles.

3 Results and Discussion

3.1 Phenanthroline-Fused Pyrazinacenes

As outlined in the introduction of this thesis, pyrazinacenes are under development as fluorescent dyes for bioimaging among other applications. Notably, the tetradecaazaheptacene chromophore has demonstrated absorption and emission spectrum overlapping with the biological transparency window (650-900 nm). Because acene compounds are also utilized in organic triplet-triplet annihilation upconversion materials, pyrazinacene-based upconversion materials present significant potential for photoactivatable DDSs by enabling tissue illumination using long-wavelength light in the biological transparency window and subsequently generating more energetic short-wavelength photons *in situ*. Furthermore, the upconversion process provides enhanced spatial precision for the light-triggered DDS photoactivation, as the upconversion efficiency scales with the square of the light flux. This ensures that the upconversion occurs almost exclusively in areas directly targeted by the laser rather than in regions exposed to scattered laser light.

3.1.1 One-pot Synthesis and Derivatization of Phenanthroline-Fused Pyrazinacenes

The initial condensation of a phenanthrene-9,10-quinone with substituted 1,2-phenylenediamine, although normally promoted by acid catalysts, can also proceed in polar solvents at elevated temperature.[203] This dehydration reaction yields a 1,4,5,8-tetraazanaphthalo-2,3-nitrile derivative, which is sufficiently electron deficient that its nitrile groups act as effective leaving groups in nucleophilic substitution reactions. Bearing these points in mind, we investigated the reaction of phenanthroline-9,10-quinone with 2,3-diamino-5,6-dicyanopyrazine (DADCP) in DMSO at different temperatures.

To our satisfaction, the main product of reactions performed at 140 °C was 6,13-dihydrodipyrido[3,2-a:2′,3′-c]-5,6,7,8,11,12,13,14-octaazapentacene-9,10-dicarbonitrile (**2**), when using two equivalents of DADCP in the presence of 2 equiv. of base (Na_2CO_3) to neutralize the HCN generated during the 2nd step of the reaction (Scheme 6). This reaction represents a straightforward method for preparing unusual phenanthroline-appended pyrazinacene compounds, whose attributes are incidentally suitable for applications mentioned in chapter *1.1.5.* and chapter *3.1*. We also successfully prepared the corresponding bis(benzo)-pyrazinacene derivative **1**. Both compounds **1** and **2** are quite insoluble in common solvents (or their mixtures) and are, therefore, difficult to purify. Nevertheless, **1** could be partially purified by column chromatography but in turn became so insoluble that it was impossible to record satisfactory NMR spectra – only ^{1}H NMR spectrum in neat [D$_1$]TFA could be recorded. The ^{1}H and ^{13}C NMR spectra of **2** could be obtained after purification either by column chromatography followed by precipitation or by Soxhlet extraction. Compounds **1** and **2** could not be sufficiently purified even by sublimation in ultrahigh vacuum.

Scheme 6. One-pot synthesis of substituted octaazapentacene derivatives **1** and **2** (reproduced from Švec, 2018 [ref. 137]).

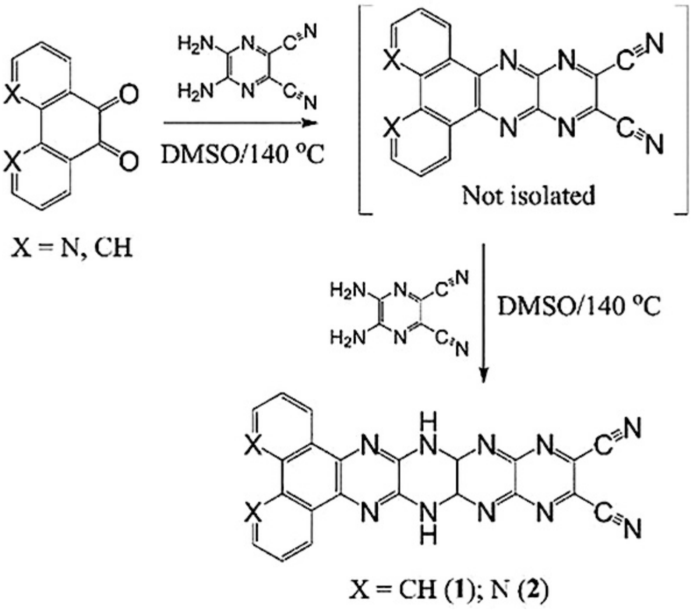

3.1.2 Pyrazinacene Derivatization for Solubilization or Conjugation

Due to the relative insolubility of compounds **1** and **2** in common solvents, we considered modification by *N*-alkylation to improve their solubility. These compounds can undergo protic tautomerization[204, 205] and *N*-alkylation generally yields complex mixtures of isomeric products. The isomeric products are generally restricted to isomers with one *N*-alkyl group on each side of the pyrazinacene core with *N*-alkylation disfavored at end pyrazine groups of the pyrazinacene molecule (even with a further fused benzo group present). We attempted the *N*-alkylation of compound **2** using higher *n*-alkyl bromides or 3,4,5-tris(dodecyloxy)benzyl chloride. However, the solubility sufficiently increased only with 3,4,5-tris(dodecyloxy)benzyl derivatives and separation of the resulting isomer mixture remained unfeasible with both *n*-$C_{12}H_{25}$ and 3,4,5-tris(dodecyloxy)benzyl modified compounds. Nevertheless, the higher solubility of the 3,4,5-tris(dodecyloxy)benzyl derivatives **3** opened the possibility to study the isomeric composition and identities of the products.

Figure 3 depicts the ^{1}H NMR spectra of of bis[3,4,5-tris(dodecyloxy)benzyl] derivatives isomeric mixture purified by gel permeation chromatography. The spectrum was decomposed according to the magenta fitted spectrum. The isomer structures were assigned based on the expected position of the NH protons in **2**, which should be present on the pyrazine ring neighboring to the ring with nitrile groups. However, the extension of donor–acceptor (D–A) interaction over another pyrazine ring ought to further stabilize the molecule although existence of the protons on a terminal pyrazinacene ring (*i.e.*, one that does not have two adjacent fused pyrazine groups) is not favored. [137, 204, 205] Therefore, the protons reside with highest probability on the third pyrazine ring remote from the nitrile groups. This assignment is supported by an X-ray crystallographic study of a similar compound, which indicates that this shift occurs. [136, 137] Using the assignment above, the calculated **3a**, **3b**, and **3c** isomer ratio is 37:22:41. The results of this initial pyrazinacene derivatization/solubilization study were used in a follow-up research to prepare pyrazinacene-(oligoethylene glycol) conjugates that are soluble in polar solvents. [140]

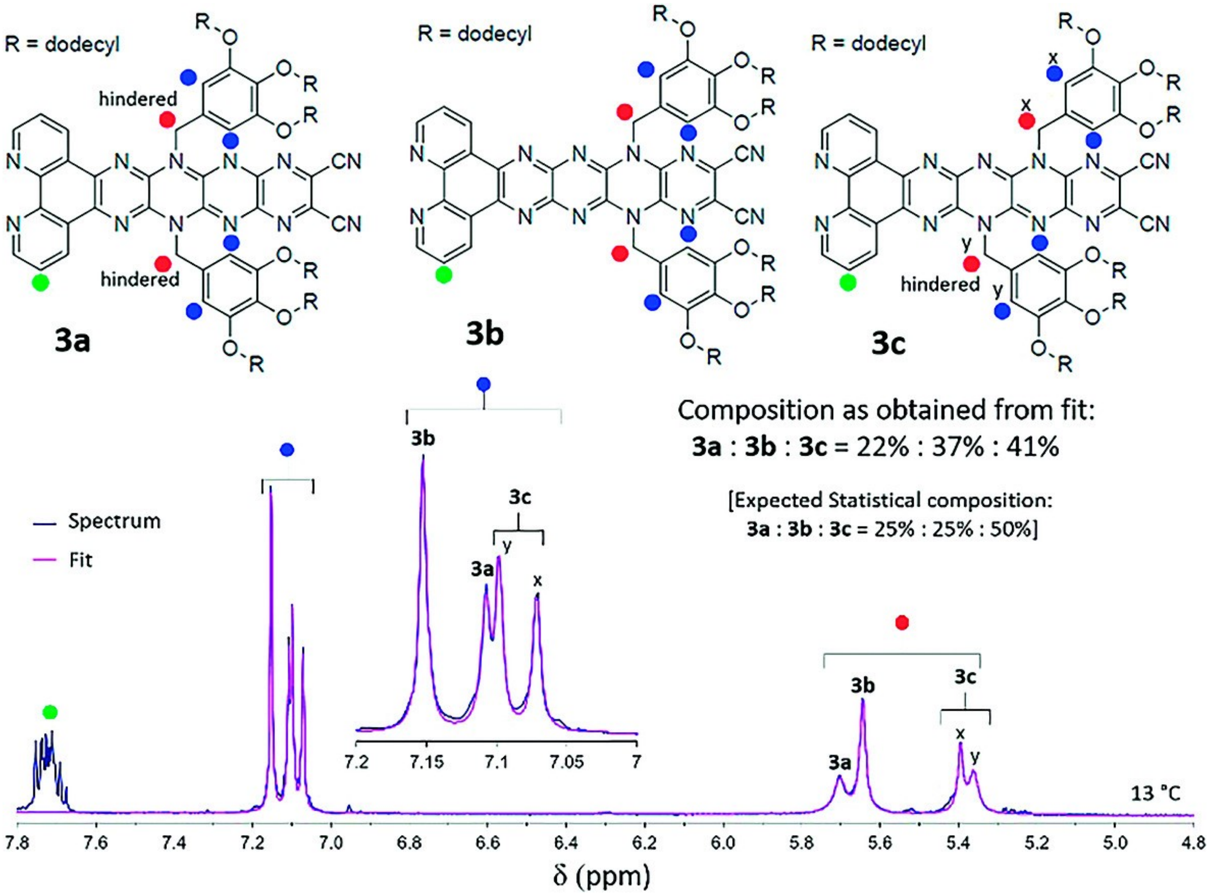

Figure 3. Analysis of the **3a-c** isomer mixture based on ^{1}H NMR spectroscopy. The fitted spectroscopic data is shown in magenta and is based on the structures **3a**–**c** at top. Other isomers may be present in small quantities and were neglected for this analysis. Peaks in the ranges 7.2–7.0 and 5.8–5.3 ppm are signals of the *N*-substituent ortho protons and benzylic protons, respectively. Expected percentage statistical composition is **3a**:**3b**:**3c** = 25 %:25 %:50 %. R = *n*-$C_{12}H_{25}$ (reproduced from Švec, 2018 [ref. 137]).

3.1.3 Ru^{II} Complexation and Photosensitizing Properties

Although our efforts towards obtaining pure examples *N*-alkylated **2** have not yet been successful, we decided to explore the question whether the properties transition metal complexes with pyrazinacene-based ligands could be of interest. For this reason, we have designed and synthesized the ruthenium complex **6** (Scheme 7) with the pyrazinacene ligand **4**, which possesses a phenanthroline moiety at a fluorubine core. Compounds similar to compound **4** are known to form only centrally *N*-alkylated isomers[206] (*N*-alkylation of terminal pyrazines is negligible in pyrazinacenes). The ruthenium complex **6** was prepared by treating *cis*-bis(2,2′-bipyridine)dichlororuthenium(II) complex with the alkylated compound **5** under standard literature conditions.[207] Complexes similar to **6** have attracted considerable attention due to their DNA-intercalating properties[208, 209] and it is known that the replacement of the fused benzo groups with fused pyrazino units can have a profound effect on the properties of the resulting complexes.[210]

Scheme 7. Synthesis of compounds **4**, **5**, and **6**. The product **4** was used as isolated without further purification (reproduced from Švec, 2018 [ref. 137]).

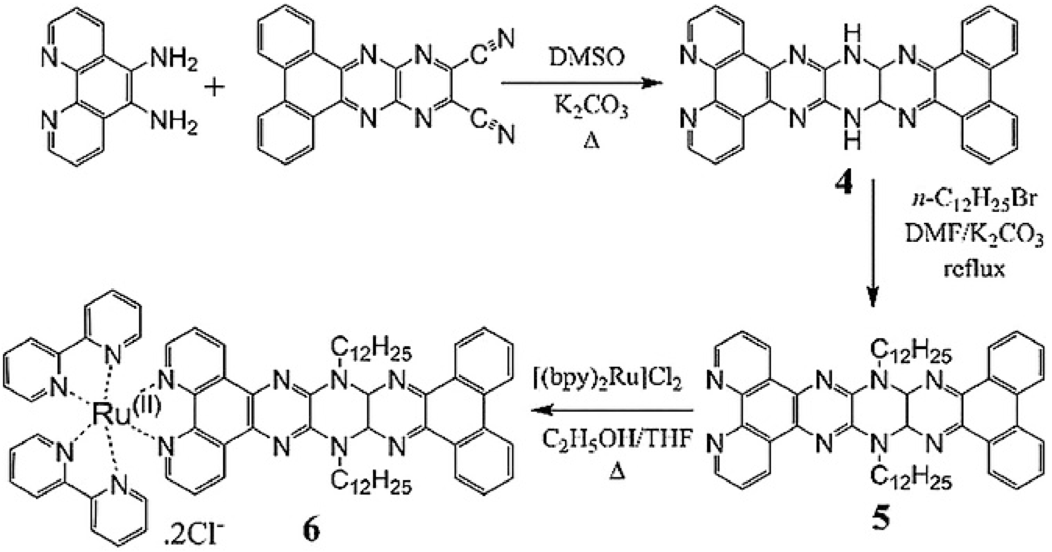

The compound **6** was obtained an orange amorphous powder soluble in common solvents despite the large π-electron surface of the tetrabenzofluorubine core. The electronic spectrum of **6** (Figure 4a) features bands assignable to the bipyridine ligands (300 nm) as well as to the acene with a four-band structure with λ_{max} at 472 and 503 nm. The weak fluorescence presents a broad band at 600 nm. An excitation spectrum was recorded by holding the emission monochromator at 531 nm and scanning the excitation monochromator revealed peaks at 460 and 492 nm (see Appendix 1 – Supporting Information), that largely resembled the absorption spectrum. Compound **6** undergoes two reversible one-electron oxidations at 1.15, 1.51 and three reversible one-electron reductions at –1.10, –1.36 and –1.75 V vs. Ag/AgCl (Figure 4b) some of them involving the pyrazinacene unit.[136] The electrochemical HOMO–LUMO gap was determined to be 2.25 eV, which is similar to the values reported for $Ru^{II}(bpy)_3$ in the literature.[211] *O*-dichlorobenzene served as the solvent for electrochemical measurements because the use of acetonitrile led to surface adsorption and process irreversibility.

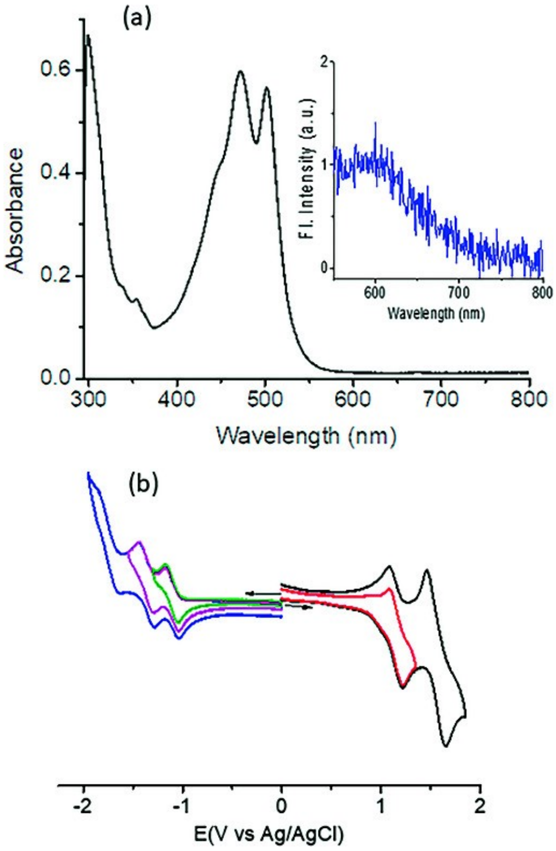

Figure 4. a) Electronic absorption spectrum of **6** in *o*-dichlorobenzene (figure inset shows the emission spectrum, λ_{ex} = 503 nm). (b) Cyclic voltammograms of **6** in *o*-dichlorobenzene containing 0.1 M $Bu_4N(ClO_4)$; (reproduced from Švec, 2018 [ref. 137]).

A dye-sensitized solar cell (DSSC) was prepared employing the compound **6** – the relevant data is presented in Figure 5.[212] TiO_2 with adsorbed compound **6** and I/I_3^- as the mediator were used in a typical DSSC configuration. It is noteworthy that the addition of a TiO_2 slurry to the solution of compound **6** led to profound fluorescence quenching, suggesting that electron injection from the excited state of **6** into the TiO_2 conduction band was taking place. The absent anchoring groups (*e.g.*, carboxyl groups) in **6** led to weaker adsorption onto TiO_2, and resulted in a rather modest performance of the DSSC.[213] It is possible that **6** is chemisorbed at the TiO_2 surface with the pyrazinacene moiety of our dye. This point will be investigated in future work by introducing other anchoring groups such as pyridyl or carboxyl at different points on the structure. The average performance metrics of two cells are presented in Figure 5a with open circuit potential = 0.42 V, short circuit current = 0.58 mA cm^{-2}, fill factor = 0.45 and η = 0.11%. Despite the modest DSSC performance, **6** proved to be a robust DSSC sensitizer, showing excellent reproducibility of voltage and current switching. Figure 5b shows the visualization of the calculated structures of the highest occupied molecular orbital (HOMO) and lowest unoccupied molecular orbital (LUMO) for compound **6**. The HOMO lies predominantly on the pyrazinacene ligand while the LUMO is accommodated on the Ru(bpy)$_2$ moiety, suggesting directional electron transfer by means of push-pull effect. [214]

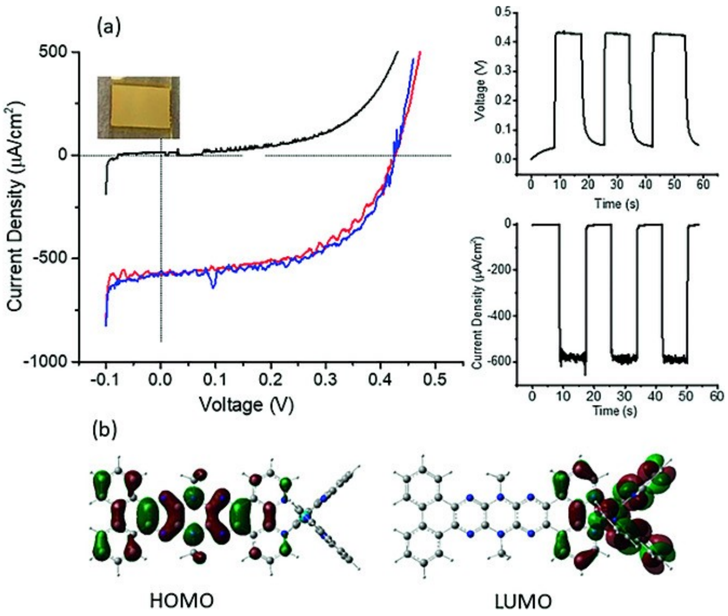

Figure 5. a) Current density vs. voltage (*J–V*) curves of DSSC constructed from **6**. Voltage and current switching plots are shown in the righthand panels. (b) Structures of the HOMO and LUMO for **6**; (reproduced from Švec, 2018 [ref. 137]).

Improving photochemical properties of **6** could be addressed by various means that have already been described by other workers. [215-217] For example, the incorporation of extended aromatic ligands has been thoroughly studied for the corresponding Ru^{II} complexes. Those works have provided insight into the structural parameters affecting the materials' performances, [218-220] and the studied compounds themselves remain highly relevant. [221, 222] The π-extended phenanthroline ligands have been extensively studied[223-226] in relation to dye-sensitizers. However, the introduction of ligands with pyrazinacene moieties to these dyes presents some prospects for developing highly fluorescent compounds with easily modifiable substituents both at the (bpy)$_2$Ru^{II} moiety (as has previously been done) and at the pyrazinacene moiety where lateral substituents at the nitrogen atoms could be employed for tuning the adsorption/interaction of the dye-sensitizer with TiO$_2$. Using different *N*-substituents could also be important for reducing any detrimental aggregative processes. NMR spectroscopy of **6** at different concentrations revealed its significant tendency to aggregate through interactions at the pyrazinacene moiety (probably π–π stacking), as manifested by the upfield shift of the corresponding NMR proton signals at higher concentrations. Our findings about the ruthenium-pyrazinacene complex **6** adds valuable extension to the previously reported compounds.

3.2 Model Light-Responsive Drug Delivery System

In this section, we introduce a novel protocol for the rapid synthesis of light-sensitive poly[ethylene oxide-*block*-(2-nitrobenzyl)acrylate] (PEO-*b*-PNBA) amphiphilic diblock copolymers with a narrow molar mass distribution, crucial for achieving tailorable, well-defined, and reproducible micellar structures and uniform biological behavior. The synthesis was performed using SET-LRP of the (2-nitrobenzyl)acrylate (NBA) monomer initiated by a PEO-containing macroinitiator. Despite the previous reports on PEO-*b*-PNBA copolymers, [227, 228] this represents the first instance of synthesizing the PNBA block via a controlled radical polymerization, resulting in copolymers with low dispersity. The micellization behavior of this copolymer was analyzed using dynamic light scattering (DLS), and its light responsiveness was demonstrated through the successful disassembly of its micelles in aqueous solutions upon UV irradiation. This system could serve as a model for biologically excretable DDS systems or be combined with upconverting materials to enable disassembly triggered by lower-energy photons within the biological transparency window.

3.2.1 Highly Defined Poly[ethylene oxide-block-(2-nitrobenzyl)acrylate]

We performed a series of test polymerizations to explore the viability of SET-LRP polymerization for the synthesis of amphiphilic PEO-*b*-PNBA copolymers (Table 1, Scheme 8, Figure 6). PEO-Br was utilized as the macroinitiator while maintaining the weight/volume ratio of NBA/DMSO at 1:2 to ensure full solubility of PEO-Br. $CuBr_2$ additive was employed to eliminate the formation of high molar mass by-products. The length of the elemental copper wire catalyst highly influenced the polymerization rate. High conversions and short reaction times (81% in 60 min) were achieved using a 5 cm wire ($d = 0.8$ mm) but the dispersity of the resulting polymer was relatively high ($Đ = 1.57$). In contrast, with a shorter copper wire (1.5 cm) an excellent control over the polymerization was achieved (Table 1).

Scheme 8. SET-LRP synthesis of PEO-*b*-PNBA copolymers (reproduced from Sedláček, 2019 [ref. 81]).

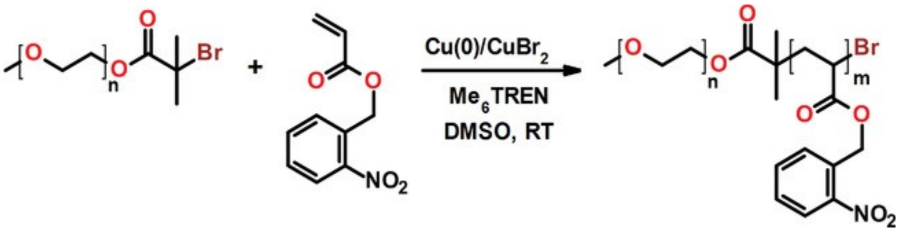

Table 1. Characteristics of PEO-*b*-PNBA copolymers

Entry[a)]	**Cu(0) wire length [cm]**	**Time [min]**	**Conversion**[b)] **[%]**	**DP(NBA)**[b)]	$M_{n(theo)}$[c)] **[Da]**	$M_{n(SEC)}$[d)] **[Da]**	$Đ_{(SEC)}$[d)]
1	5	60	81	40	13500	26500	1.57
2	3	60	75	37	12300	20900	1.35
3	1.5	60	52	26	10500	12300	1.1
4	1.5	120	8.3	4	13700	19100	1.26

a) Initial monomer feed ratio $[NBA]_0$:$[PEO\text{-}Br]_0$:$[Me_6TREN]_0$:$[CuBr_2]_0$ = 50:1:1:0.1 in DMSO $[NBA]_0$ = 1.61 m; b) Determined by ^{1}H NMR spectroscopy; c) Calculated by formula $M_{n(theo)} = [([NBA]_0/[PEO\text{-}Br]_0 \times \text{conversion} \times M_{NBA}] + M_{PEO\text{-}Br}$; d) Determined by size-exclusion chromatography (SEC).

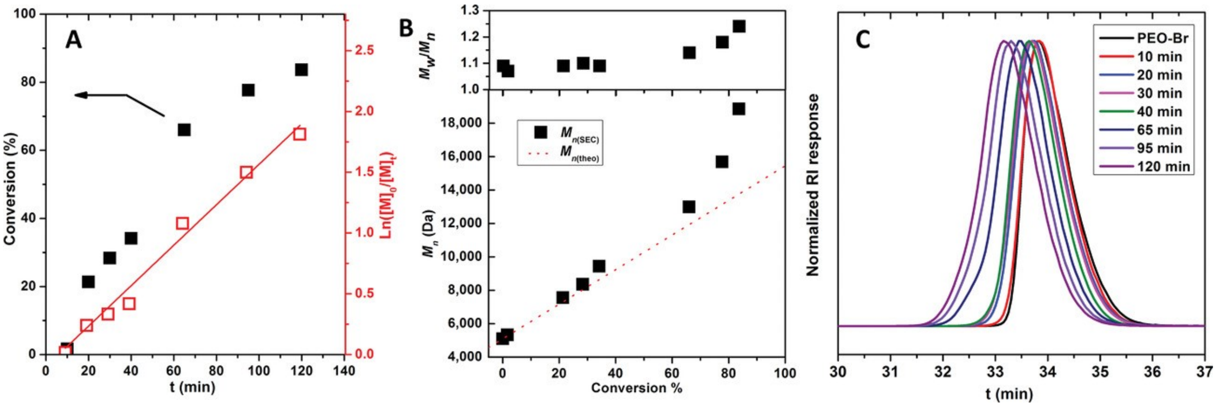

Figure 6. SET-LRP of NBA using $[NBA]_0$:$[PEO\text{-}Br]_0$:$[Me_6TREN]_0$:$[CuBr_2]_0$ = 50:1:1:0.1 in DMSO at 25 °C, initiated with 1.5 cm 20-gauge copper wire, using 3 g of NBA. A) Conversion plot of NBA monomer. B) Plot of molar masses and dispersities. C) SEC chromatograms of PEO-*b*-PNBA copolymers; (reproduced from Sedláček, 2019 [ref. 81]).

The polymerization kinetics was studied by ^{1}H NMR and size-exclusion chromatography (SEC). Following an induction period, the polymerization proceeds by pseudo-first-order kinetics with respect to the NBA monomer (Figure 6A). The apparent propagation rate constant determined by the linear fit of the kinetic plot was $k_p = 8.6 \pm 0.4 \times 10^{-3}$ L mol^{-1} s^{-1}. The reported in this work is approximately one order of magnitude higher than the previous results by Six *et al.* who polymerized NBA using ethyl-2-bromoisobutyrate initiator. [229] The herein described polymerization rate constant as well as the shorter induction period (t_{ind} = 7 min) could be explained by a more effective activation of the copper wire surface using hydrazine solution. [229, 230] The first-order kinetics was observed for monomer conversions up to ≈65%. At higher than conversions, the chain-chain coupling led the molar mass deviation towards the higher values and to increased polymer dispersity (Figure 6B). The final polymer, PEO_{114}-*b*-$PNBA_{26}$, was also characterized by diffusion-ordered NMR spectroscopy (DOSY, Figure 7). The DOSY spectra revealed identical diffusion coefficients for each ^{1}H NMR polymer peak and confirmed the block structure of the synthesized copolymer.

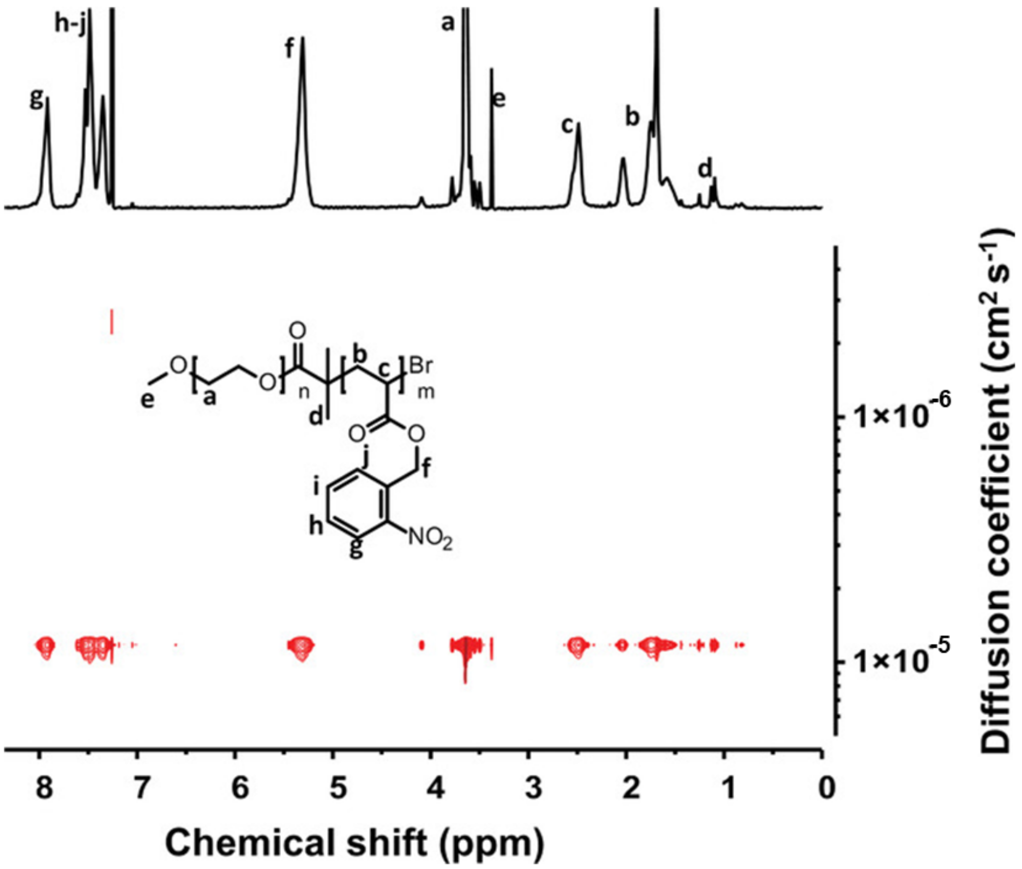

Figure 7. ^{1}H NMR (top) and DOSY (bottom) spectra of PEO_{114}-*b*-$PNBA_{26}$ in $CDCl_3$ (adapted from Sedláček, 2019 [ref. 81]).

3.2.2 Nanoparticles and UV Induced Disassembly

The irradiation studies were performed with a diblock polymer of composition PEO$_{114}$-*b*-PNBA$_{26}$, where the weight ratio of hydrophilic to hydrophobic blocks is approximately equal. Nanoprecipitation of the PEO$_{114}$-*b*-PNBA$_{26}$ copolymer in water or PBS (pH = 7.4) led to nanoparticles with an average hydrodynamic diameter of 25 nm. The CAC of the block copolymer was obtained in PBS by fluorescence spectroscopy using pyrene. The CAC value of PEO$_{114}$-*b*-PNBA$_{26}$ (CAC = 8.1 mg L^{-1}) was similar to previously reported values for similar block copolymers. [231]

Irradiation of the micellar solution by UV light (mercury lamp) led to the hydrophilization of the whole polymer system by inducing photo-cleavage of the hydrophobic *o*-nitrobenzyl groups. The photodecomposition of *o*-nitrobenzyl esters can be observed by UV–vis spectroscopy. The intense *o*-nitrobenzyl ester absorption at 275 nm decreases, whereas the band of the formed *o*-nitrosobenzaldehyde appears at 326 nm (Figure 8A). [229] Therefore, we used the absorption at 326 nm to determine the extent of UV-triggered PNBA block photodecomposition in both water and in PBS (Figure 8B). The disassembly of micelles irradiated in pure water was slightly faster (but not statistically significant; $p > 0.1$). Furthermore, ^{1}H NMR spectra of the UV-irradiated (10 min) and subsequently freeze-dried samples were measured (Figure 9). The part of the spectrum corresponding to aromatic photodecomposition products was relatively complex but the signal at δ = 10.4 ppm confirmed the presence of *o*-nitrosobenzaldehyde. The degree of photodecomposition was calculated based on the change in the intensity ratio of the PNBA signals (-O-$\mathbf{CH_2}$-Ph, δ = 5.4 ppm) to the PEO signal at δ = 3.6 ppm.

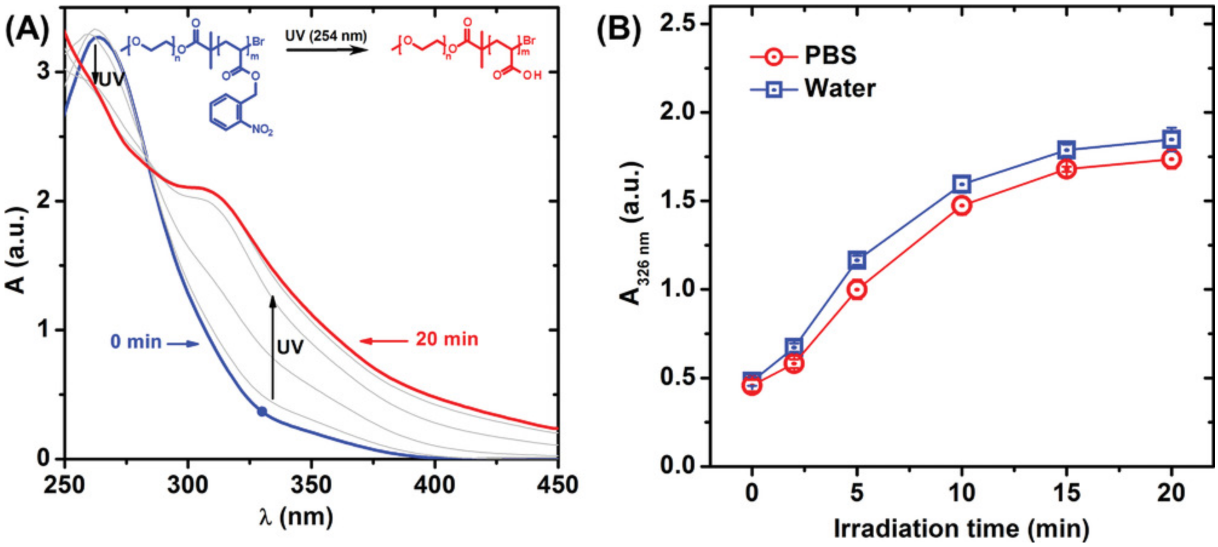

Figure 8. Absorption spectra measured following irradiation of PEO_{114}-*b*-$PNBA_{26}$ micelles in PBS ($c = 0.5$ mg mL^{-1}) (A). The initial (blue line) and final (red line) spectra are highlighted. Dependence of polymer absorption at 326 nm on irradiation time (B); (reproduced from Sedláček, 2019 [ref. 81]).

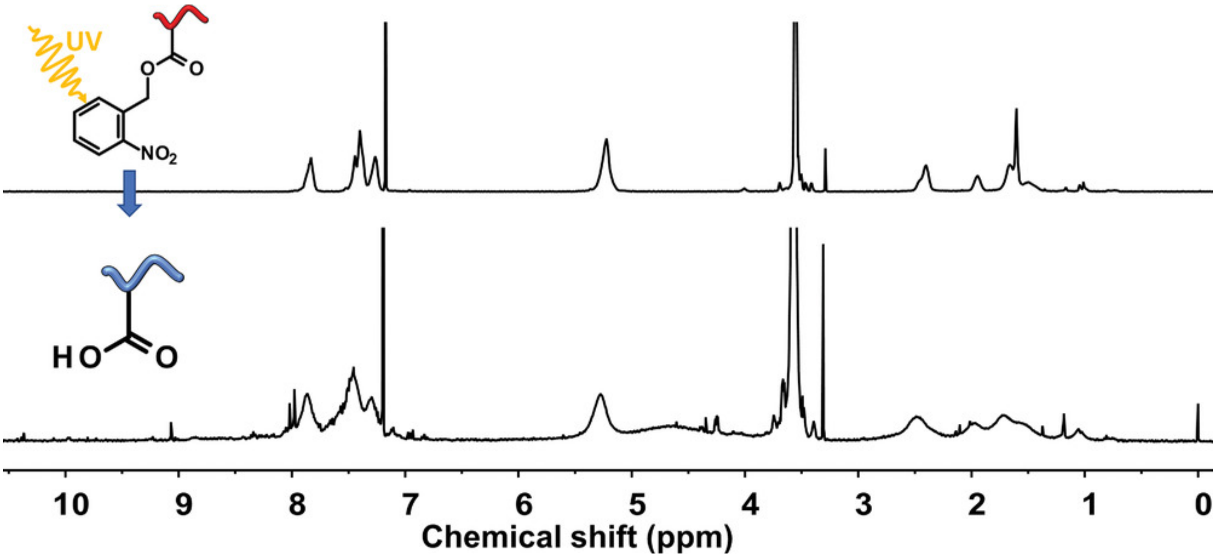

Figure 9. ^1H NMR spectra of PEO_{114}-*b*-$PNBA_{26}$ micelles before (top) and after (bottom) UV-irradiation in water for 10 min. Spectra measured in $CDCl_3$ (reproduced from Sedláček, 2019[81]).

The UV-induced disassembly the polymer micelles was also studied by DLS (Figures 10 and 11). The scattered light intensity is the most intuitive parameter for analyzing nanoparticle disassembly due to its power law dependence on the size of the nanoparticle/micelle. Indeed,

Figure 10A gives proof of the disassembly process triggered UV-light irradiation. Considering this finding, we have analyzed the hydrodynamic diameter distribution functions at different irradiation timepoints. At short irradiation times, the PEO_{114}-*b*-$PNBA_{26}$ copolymer in water showed a monomodal peak with D_h approximately 25 nm (Figure 10B,C). We attributed this peak to micelles. With longer irradiation times, the peak shifted to lower D_h, as a result of the polymer hydrophilization and micelle disassembly. In the PBS-buffered solution, the D_h value rapidly dropped to ≈9 nm and did not change during further irradiation. This behavior can be explained by constant pH of the buffered solution during irradiation, where the acrylic acid units are ionized and negatively charged. This led to stronger hydrophilization and micelle disassembly.

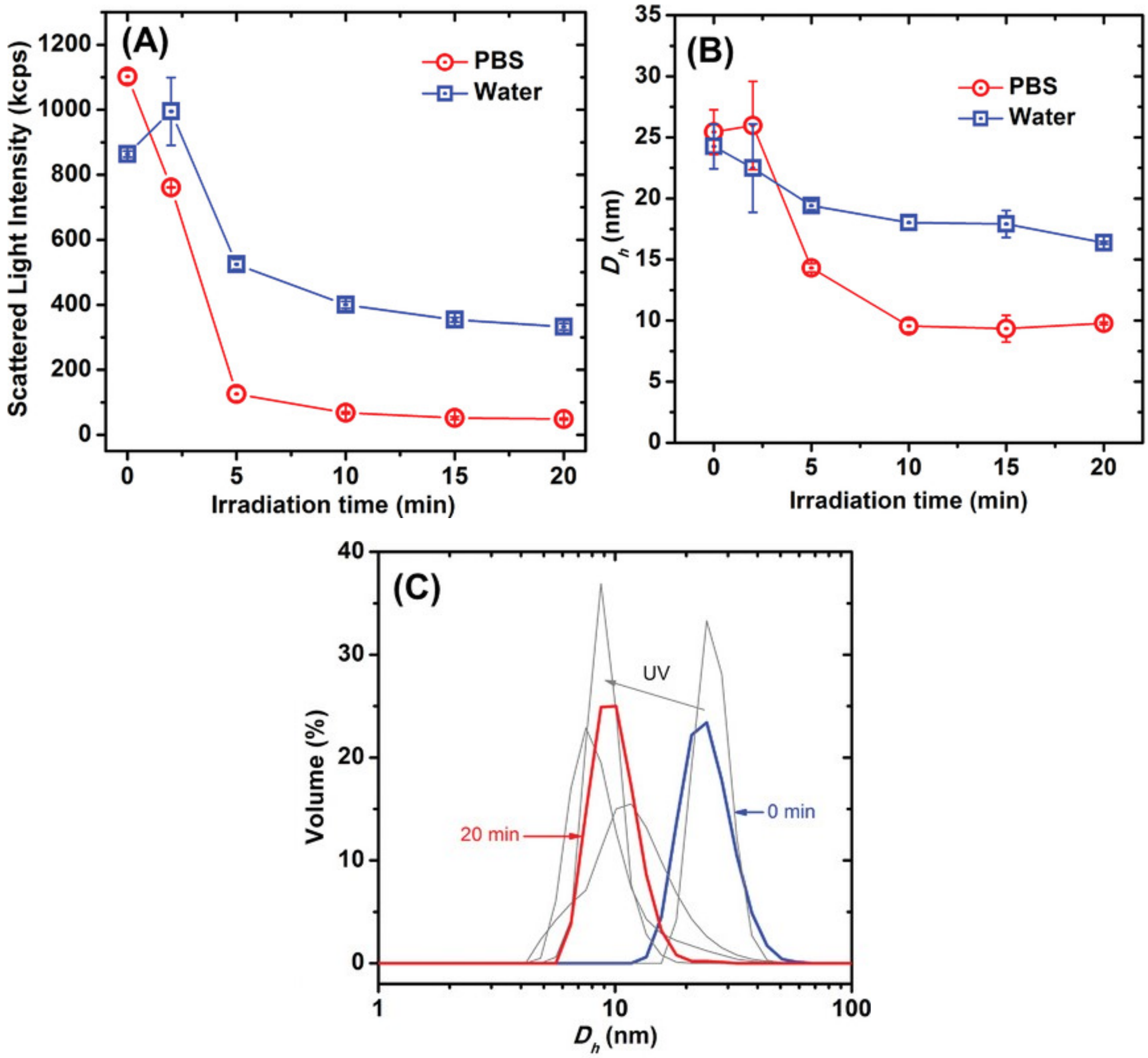

Figure 10. UV-light responsive degradation of the PEO_{114}-*b*-$PNBA_{26}$ micelles in water in PBS buffer. Dependence of the scattered light intensity (A) and hydrodynamic diameter (B) on the irradiation time. Hydrodynamic diameter distribution functions at different irradiation times in PBS (C); (adapted from Sedláček, 2019 [ref. 81]).

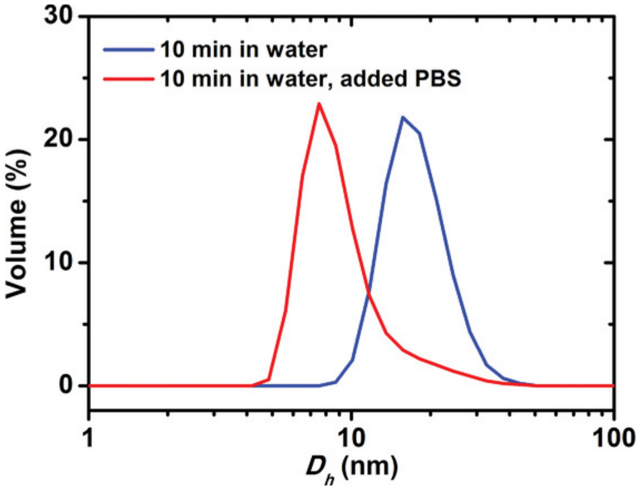

Figure 11. Hydrodynamic diameter distribution functions PEO_{114}-*b*-$PNBA_{26}$ micelles irradiated 10 min in water before (blue) and after (red) consequential addition of PBS (reproduced from Sedláček, 2019 [ref. 81]).

On the other hand, irradiating the micelles in pure water led to a drop in pH, gradual micelle disassembly and formation of larger objects with D_h around 17 nm. We have experimentally confirmed that the pH dropped below the pK_a of the acrylic acid units after 10 minutes (pH = 4.26) and 20 minutes (pH = 4.01) of irradiation. Moreover, low pH not only leads to decreased hydrophilicity of the poly(acrylic acid) block but also promotes aggregation through formation of the hydrogen-bonded poly(acrylic acid)-PEO polyplexes. Similar behavior was described with mixtures poly(acrylic acid) and PEO homopolymers. [232] To support this hypothesis, we irradiated the micelle solution in pure water for 10 min and subsequently adjusted solution pH to 7.4 by adding a PBS tablet. This led to a drop of D_h value measured by DLS from 18 to 8 nm (Figure 11). Surprisingly, with the sample irradiated for longer time (20 min) the pH adjustment did not result in micelle disassembly, but larger objects with an average D_h of 36 nm were observed (see Appendix 2 - Figure S3, Supporting Information). This could be ascribed to a UV-mediated crosslinking of the assembled micelles during longer irradiation at low pH. Similar UV-induced crosslinking was reported in the literature. [233] The nanoparticle size increase ("swelling") is caused by adjusting the pH to a higher value, leading to ionization and repulsion of the carboxyl groups in the poly(acrylic acid) block. In conclusion, PEO-*b*-PNBA micelles in pure water manifest a more complex behavior under UV irradiation. However, for the intended applications in stimuli-responsive DDSs the system's behavior in buffered media (PBS) is relevant.

3.3 Responsive Fluorinated Polymers Based on Poly[*N*-(2,2-difluoroethyl)acrylamide]

Thermo-/pH- and thermo-/redox-responsive behaviors represent another approach to self-assembled polymer systems. Carefully designed polymers, initially molecularly dissolved at room temperature, may self-assemble into various nanoparticle architectures or alternatively aggregate into bulk precipitate/polymer depots. However, this assembly occurs only at the conditions fulfilling both the right interval of pH and temperature (thermo-pH) or redox potential and temperature (thermo-redox). In this section, we describe a novel series of fluorinated polymers, based on the previously published poly[*N*-(2,2-difluoroethyl)acrylamide] (PDFEA) ^{19}F MRI tracers,[234, 235] designed for injectable implants with varying dissolution rates under physiological conditions. By altering polymer compositions and including pH-responsive imidazole moieties and hydrophilic *N*-(2-hydroxyethyl)acrylamide monomeric units, we tailored different dissolution rates to meet various application demands. We also present novel PDFEA-based polymers with incorporated ferrocene moieties oxidizable to the positively charged and more hydrophilic ferrocenium species. These polymers were intended for dual thermo- and ROS-responsive diblock copolymeric DDS that can be monitored by ^{19}F MRI.

3.3.1 Synthesis and Properties of Thermo-/pH- and Thermo-/Redox-Responsive Polymers

The fluorinated multiresponsive copolymers poly{*N*-(2,2-difluoroethyl)acrylamide-*co*-*N*-[3-(*1H*-imidazol-1-yl)propyl]acrylamide-*co*-*N*-(*2*-hydroxyethyl)acrylamide} (P(DFEA-ImPA-HEA)) were prepared by statistical copolymerizations of the corresponding monomers using RAFT technique with 4-cyano-4-[(dodecylsulfanylthiocarbonyl)sulfanyl]pentanoic acid as the chain transfer agent (Scheme 9). While the *N*-(2,2-difluoroethyl)acrylamide monomeric units provided the copolymers with LCST and ^{19}F MRI contrast properties, the pendant imidazole groups endowed them with pH-responsive character. Finally, we employed the *N*-(2-hydroxyethyl)acrylamide units to tune the polymer hydrophilicity. We prepared the copolymers in five different monomer unit ratios (Table 2) to achieve variable dissolution rates *in vivo*. All studied copolymers had a molar mass of approximately 40 kDa (near the glomerular filtration cutoff[236]) and a narrow dispersity ($Đ \leq 1.20$). The positive charge of the polymer and molar mass near the glomerular filtration cutoff should allow renal excretion after the injectable implant dissolves. Polymers with LCST properties have been demonstrated to be excreted by the kidneys and bile, even when the LCST of the polymer is significantly below body temperature. This occurs due to equilibration between the phase-separated and dissolved phases.[237]

Scheme 9: Structure and synthesis of multiresponsive fluorinated P(DFEA-ImPA-HEA) copolymers **F1-F5**. Polymer chain-end groups were omitted for clarity (reproduced from Kolouchová, 2020 [ref. 88]).

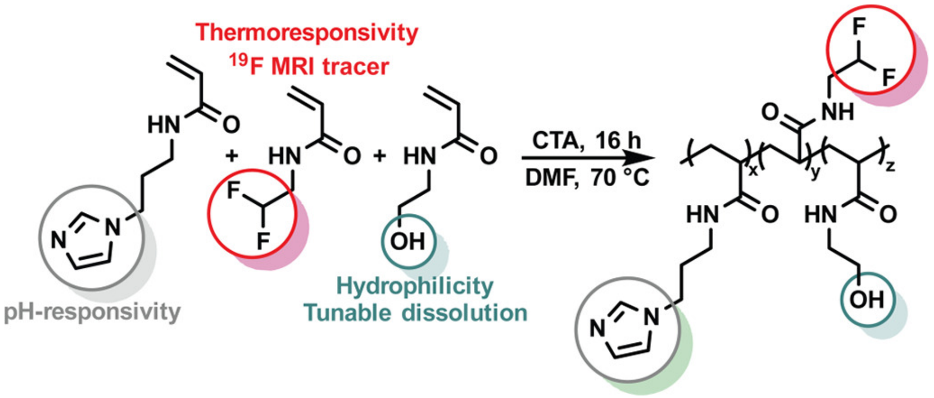

Table 2. The composition and physicochemical properties of the prepared polymers.

Polymer	Polymer Composition[a] [mol. %]			Fluorine [wt %]	M_w [kDa][b]	Đ(SEC)[b]	T_{CP} (°C)[c]	
	DFEA	ImPA	HEA				pH 7.4	pH 5.0
F0 [234]	92	8	0	25.8	41.9	1.10	22	43
F1	88	7	5	24.8	37.8	1.12	27	60
F2	84	8	8	23.6	37.9	1.09	31	71
F3	76	9	15	21.4	32.8	1.19	37	>85[d]
F4	70	9	21	20.2	43.7	1.05	54	(85)[d]
F5	58	9	33	16.3	47.4	1.09	(67)[d]	(85)[d]

Determined by ^{1}H NMR spectroscopy,[a] SEC[b] or turbidimetry.[c] Inaccurate data.[d]

We analyzed the thermo- and pH-responsive behaviors of the polymers using turbidimetry based on the temperature-dependent sample transmittance in two different buffer solutions (PBS buffer with pH = 7.4 and acetate buffer with pH = 5.0). The polymers were designed to exhibit a significant difference in T_{CP} (Table 2) under acidic versus physiological conditions. The polymers were soluble in water at pH 5.0, at which the T_{CP} value of the copolymer was intended to be well above body temperature to prevent polymer aggregation and needle obstruction during injection. [238] In contrast, the T_{CP} at pH 7.4 must be below the body temperature to ensure rapid aggregation and formation of the implant. The copolymers **F1**, **F2**, and **F3** exhibited T_{CP} values within the selected range. However, **F3** precipitated at ≈ 37 °C at pH 7.4, which is too high for the formation of a sufficiently stable implant (body temperature in rats is 36.5 °C[239]). With increasing content of hydrophilic *N*-(2-hydroxyethyl)acrylamide monomer units, the T_{CP} also increased, which is in accordance with the general trend observed for LCST copolymers. [240, 241] The copolymers **F4** and **F5**, with the highest amount of *N*-(2-hydroxyethyl)acrylamide, exhibited T_{CP} far above the body temperature rendering them unsuitable for injectable implants (Figure 12).

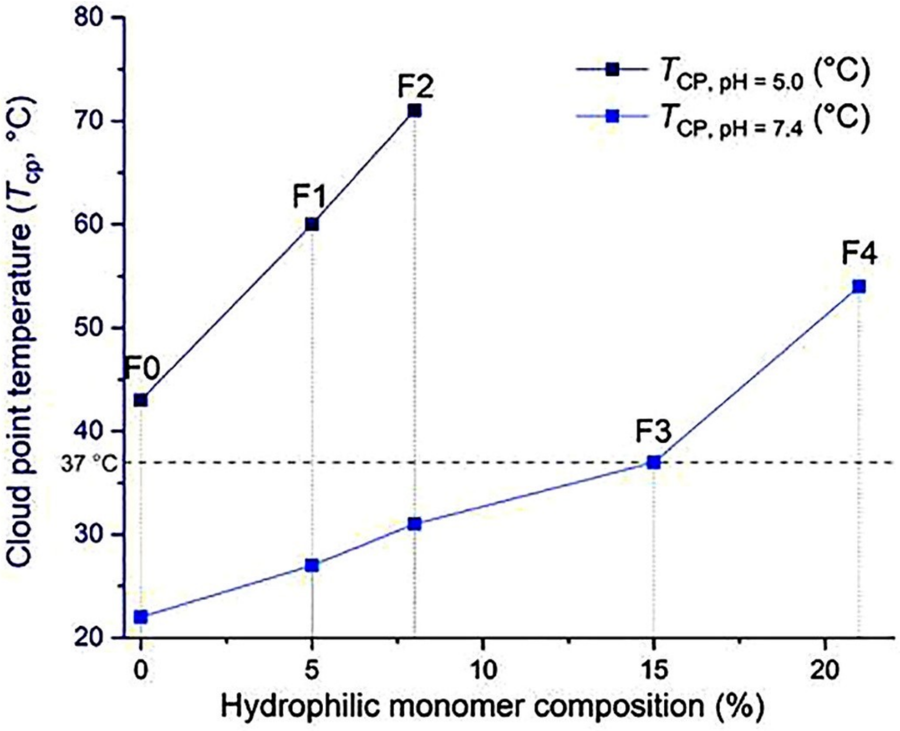

Figure 12. Correlation among composition and physicochemical properties - cloud point temperatures of each polymer at pH 5.0 and 7.4 as a function of the polymer (**F0-F4**) composition (% of hydrophilic monomer); (reproduced from Kolouchová, 2020 [ref. 88]).

Next, we decided to design and study related PDFEA-based block polymers with incorporated ferrocene moieties to obtain materials with thermo-/redox-responsive behavior. The fluorinated copolymers based on poly[*N*-(2-hydroxypropyl)methacrylamide]-*block*-poly{*N*-(2,2-difluoroethyl)acrylamide-*stat*-*N*-[2-(ferrocenylcarboxamido)ethyl]acrylamide} (PHPMA-*block*-P(DFEA-*stat*-FcCEA) (**HF1**, **HF2**, and **HF3**) are amphiphilic diblock copolymers. The hydrophilic to hydrophobic block ratio was 1:2, and the ferrocene content varied from 0.5 to 3.0 wt %. We prepared the polymers **HF1**-**HF3** by polymerizing the corresponding monomers in two subsequent RAFT reactions with the same chain transfer agent as with **F0**-**F5** and using the PHPMA-CTA as a macroinitiator for the second polymerization. The ferrocene moieties were introduced by postpolymerization modifications (amine deprotection followed by amide coupling with ferrocenecarboxylic acid; Scheme 10).

Scheme 10. Synthesis of Multiresponsive Fluorinated PHPMA-*block*-P(DFEA-*stat*-FcCEA) Copolymers **HF1**, **HF2**, and **HF3**; the polymer chain end moieties were omitted for clarity (adapted from Kolouchová, 2021 [ref. 117]).

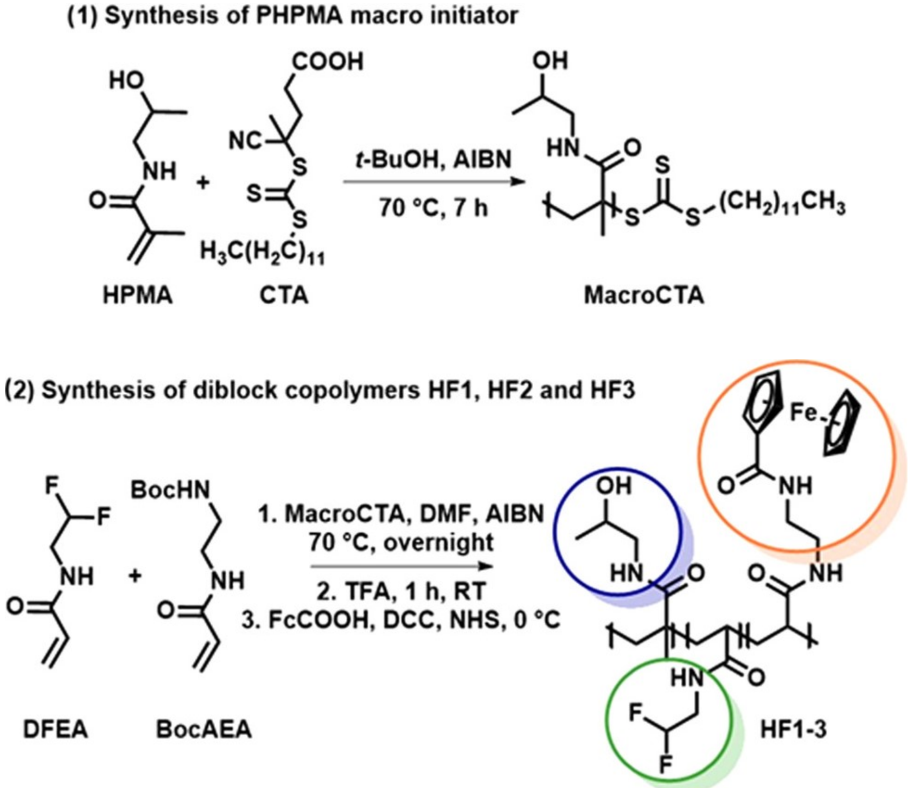

Table 3. Composition and Physicochemical Properties of Polymers

	block ratio[a]	M_w[b] [kDa]	M_n[b] [kDa]	$Đ$[b]	fluorine[a,d] [wt %]	ferrocene[d] [wt %]
PHPMA	–[d]	8.68	8.02	1.09	–	–
HF1	1:1.8	32.3	26.3	1.22	16.7	0.49 ± 0.12
HF2	1:1.9	29.1	26.0	1.12	18.0	0.80 ± 0.12
HF3	1:1.8	34.0	27.9	1.22	16.6	2.63 ± 0.66

Determined by ^{1}H NMR spectroscopy;[a] Determined by SEC;[b] Determined by ICP-MS-MS;[c] Not applicable (−).[d]

The PDFEA component of **HF1**-**HF3** with its high fluorine content ensures the LCST properties and enables particle self-assembly at increased temperature as well as suitability for ^{19}F MRI. The *N*-[2-(ferrocenylcarboxamido)ethyl]acrylamide units (FcCEA) incorporated into the PDFEA block are responsible for the redox-responsive behavior and potential control over the drug release in a DDS. The PHPMA hydrophilic block colloidally stabilizes the nanoparticles formed increased temperature (close to body temperature). The varying ferrocene contents in polymers **HF1**-**HF3** (approximately 0.5, 1.0, and 3.0 wt %, Table 3) were used to assess the effects of these redox-responsive moieties on the general physicochemical behavior of these polymers.

The self-assembly induced by temperature change was measured for neat copolymers (Figure 13, black trends) and for polymer formulation with a hydrophobic drug (GSK 429286, 0.1 mg·mL^{-1}, Figure 13, gray trends).

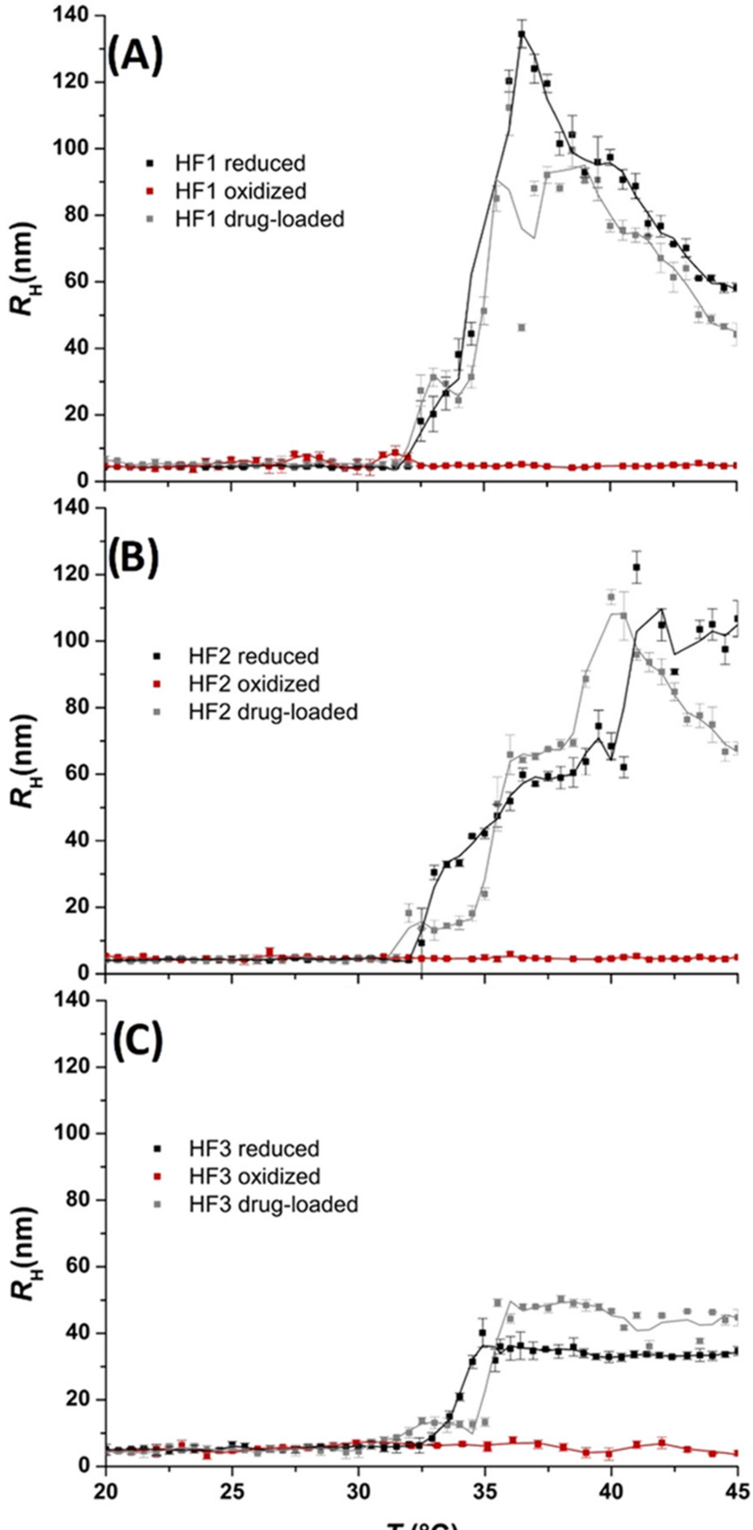

Figure 13. Graphs (A–C) show the particle size (determined by DLS) as a function of temperature for HF1, HF2, and HF3 in their reduced forms in PBS (black trends), in their oxidized forms in acetate buffer (red trends), and in their reduced drug-loaded form in PBS (GSK 429286, 0.1 mg mL^{-1}, gray trends); (adapted from Kolouchová, 2021 [ref. 117]).

The ROS-responsive behavior was studied by oxidizing the polymer ferrocene moieties and measuring the hydrodynamic diameter distributions as a function of temperature (Figure 13). Plethora of ferrocene oxidation methods has been reported such as H_2O_2 in the presence of enzymes and metal ions and acids.[242-245] The ferrocene oxidation by H_2O_2 or oxygen without added catalyst has an induction period, a relatively slow kinetics and is autocatalytic.[109, 242] The ferrocene oxidation can be directly observed by the naked eye as the yellow-orange ferrocene (Fc^0) changes to greenish and finally deep blue ferrocenium (Fc^+). We decided to simulate the conditions for our *in vitro* measurements using acidic pH to simulate the environment tumor endosomes (pH 5.0).[246] To circumvent the slow ferrocene oxidation kinetics we employed Fenton oxidation conditions.[247] Our measurements confirmed that the polymer oxidation prevents particle formation within the measured temperature range for all **HF1-HF3** polymers (Figure 13, red trends). These results indicated that ferrocene moiety oxidation triggered the particle disassembly and shifted the particle formation temperature outside of the physiological range.

3.3.2 Assessment of ^{19}F MRI and Biological Properties

The PDFEA-based tracers have a relatively unique ^{19}F chemical shift (−124 ppm) allowing a parallel imaging with the more “traditional” perfluorocarbon tracers (shifts from −80 ppm to −70 ppm). The T_1 and T_2 relaxation times of **F1**-**F4** were measured at the magnetic field of 4.7 T, temperature of 37.0 °C and two pH values 5.0 and 7.4, respectively. Both T_1 and T_2 were approximately 380 ± 50 ms (T_1 and T_2 were equal within the margin of the experimental error) for the **F1**-**F4** polymers in both their non-aggregated (pH = 5.0) and aggregated forms (pH = 7.4). This makes **F1**-**F4** polymers suitable even for the most common MRI sequences. [248] It has to be noted, that the minor difference in the relaxation times of the aggregated and non-aggregated samples (pH 7.4 and 5.0, respectively) indicates high mobility even in the aggregated state.

Despite numerous theoretical and experimental studies on the prospective use of LCST polymers for implant drug formulations and controlled drug release, very little is known about the dissolution rates ad pharmacokinetics of these polymer implants. We injected polymers **F1**-**F4** subcutaneously and intramuscularly into healthy rats. Subsequently, we used the MR spectroscopy (Appendix 3 – Table S2) and MRI signal intensity data (signal-to-noise ratio, Appendix 3 – Table S4, S6) combined with MRI-assessed implant volume (Appendix 3 – Figure 3, Table S3, S5) to extract specific pharmacokinetic data (Figure 14).

Shortly after administration (simultaneous intramuscular and subcutaneous) a fast decrease in the ^{19}F MR signal intensity over 2 to 3 days was observed. The initial decrease was more pronounced with the more hydrophilic polymers, possibly due to their faster dissolution and subsequent excretion during the first phase. After this initial period, the ^{19}F MR signal intensity decrease closely followed pseudo-first-order kinetics (Figure 14).

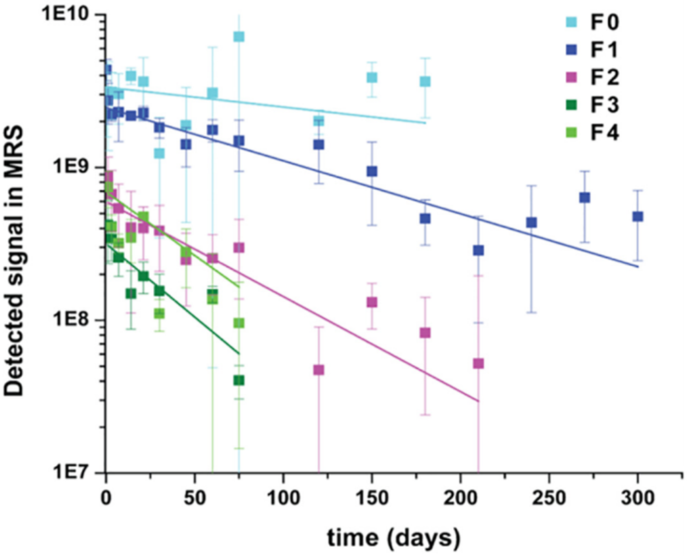

Polymer	A_{MRS}	$t_{1/2} \pm$ SD (days)	R^2
F0	1.0	> 200	-
F1	0.6	86 ± 18	0.92
F2	0.2	48 ± 8	0.75
F3	0.1	36 ± 31	0.14
F4	0.2	31 ± 8	0.62

Figure 14. The non-localized ^{19}F MR spectroscopy from thigh part of rat body performed with 4 cm circular ^{1}H/^{19}F RF surface coil dissolution kinetics of polymers F0-F4 as a function of time. Parameters A_{MRS} and $t_{1/2}$ of the polymers, the fitting-based SD, the fitting R^2; (reproduced from Kolouchová, 2020 [ref. 88]).

To summarize, the T_{CP} of the polymer at the given pH grows linearly with increasing amount of the hydrophilic monomer (in agreement with previous studies[241]) and its dissolution rate increases ($t_{1/2}$ decreases). In order to demonstrate the clinical potential of our polymers, a rat was scanned using a commercial 3 T MRI scanner equipped with a custom rat ^{1}H/^{19}F volume coil, capable of measuring both ^{1}H MRI and ^{19}F MRI. The merged image is presented in Figure 15.

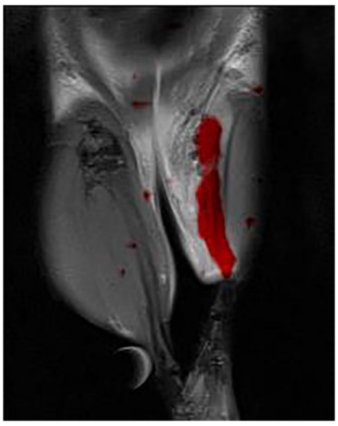

Figure 15. *In vivo* experiment with the clinically used 3 T MRI showing a merged ^{19}F MRI (red) and ^{1}H MRI (grayscale); (reproduced from Kolouchová, 2020 [ref. 88]).

Although aggregation of the PDFEA copolymers **F1**-**F4** does not induce changes in their MR properties, their MR properties may be influenced by the surrounding environment. [88, 249] The oxidation of the ferrocene-containing **HF1**-**HF3** polymers that transforms its diamagnetic ferrocene moieties into paramagnetic ferrocenium may affect the ^{19}F MRI signal. To address this question, we recorded the NMR spectrum of the ferrocene-containing polymer **HF1** before and after oxidation. No change in chemical shift or signal broadening (indicating no significant change in T_2*) was detected. No observable changes in the NMR spectra are most likely attributable to the relatively minor ferrocene content, whose oxidation affects only the surrounding DFEA monomeric units. Most fluorinated moieties remain unaffected, and thus the ^{19}F NMR signal remains virtually unchanged. To further support applicability of these polymers, we also performed ^{1}H/^{19}F MRS and MRI imaging with the polymer **HF1** (Figure 16). The phantom visualization **HF1** was possible with polymer concentrations as low as 12.5 mg·mL^{-1}.

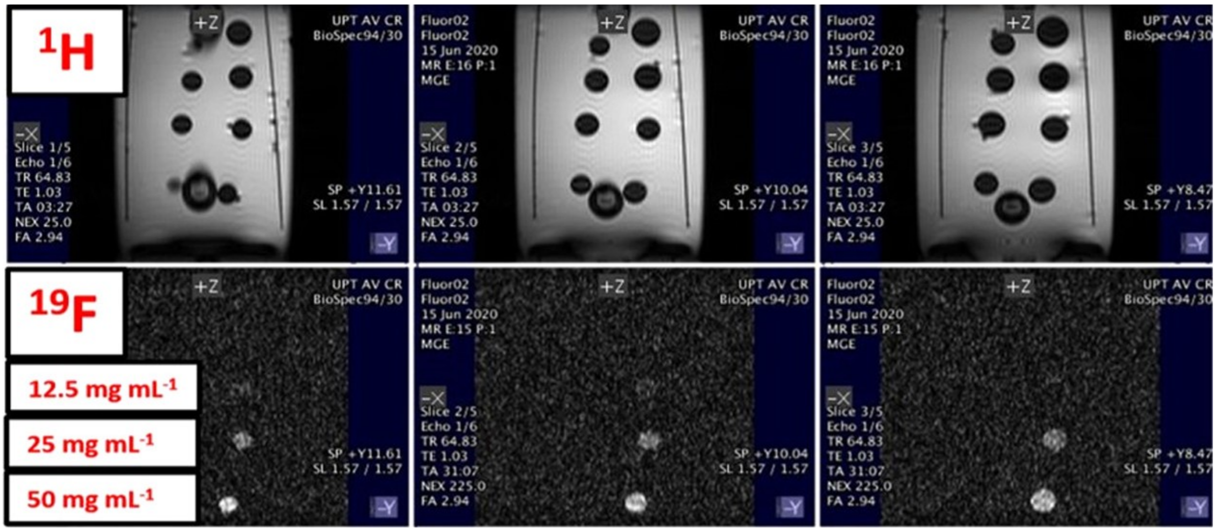

Figure 16. *In vitro* phantom ^{1}H MRI and ^{19}F MRI images with decreasing **HF1** polymer concentrations. Signal-to-noise ratio (SNR) = 6.9; (reproduced from Kolouchová, 2021 [ref. 117]).

3.3.3 Assessment of Drug-Delivery Properties

To investigate the potential of our pH-responsive polymer **F1** for depot drug formulations, we performed an *in vitro* experiment using dexamethasone (polymer **F4** with high T_{CP} above body temperature served as a control). Dexamethasone was selected based on its high biological potency (low concentrations necessary) and, although relatively hydrophobic (log$P$ = 1.8),[250] dexamethasone was sufficiently soluble for a convenient analyzing its aqueous concentration by means of UV-HPLC. In this experiment, we dissolved the polymer (**F1** or **F4**) dissolved in a saturated dexamethasone solution. The resulting solution was transferred into a mini-dialysis kit and placed into a pre-heated (37 °C) PBS solution. The polymer **F1** immediately aggregated and formed a "depot", whereas no change was observed with polymer **F4**. Aliquot samples of the solution at the outer dialysis membrane side were analyzed using UV-HPLC to quantify the concentration of the released dexamethasone.

With both polymers **F1** and **F4**, a fast release phase (commonly referred to as the "burst" release with depot formulations) was observed during the first 10 h. This corresponds to the release of the non-polymer bound portion of dexamethasone. After this fast initial phase, a significantly slower gradual release was observed with the polymer **F1**. The release from **F1** was sustained and accounted for approximately 10% of the contained drug per day (the $t_{1/2}$ of the release was 2.2 days). The drug release rate may depend on the drug hydrophobicity, as reported in similar systems.[251-254] Given that the *in vivo* dissolution of the PDFEA polymer depots is considerably slower than *in vitro* dissolution,[88] the drug release rate *in vivo* may also be significantly slower than in our *in vitro* model.[255, 256] Our results indicate that the **F1** polymer depot with can incorporate a portion of the drug (determined by the log*P* of the drug) and sustain its gradual release (see Figure 17). In contrast, the polymer **F4** with T_{CP} well above the experimental temperature was not able significantly extend the drug release time. Based on our *in vitro* results, we conclude that our systems may be suitable for designing extended-release depot formulations of hydrophobic drugs.

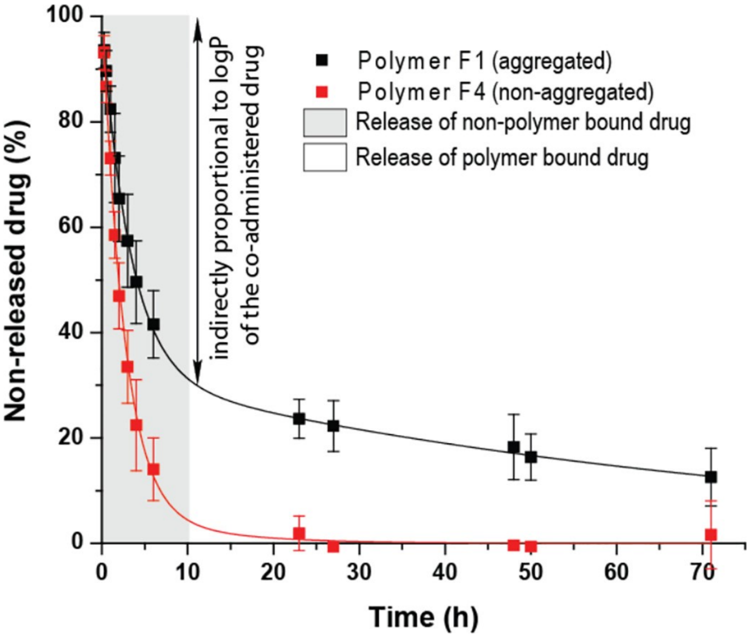

Figure 17. Drug release from a 50 mg depot *in vitro*; the graph shows the concentration of dexamethasone released from the depot F1 and the control F4 as a function of time (the data were fitted with the Formula 7, see Appendix 3); (reproduced from Kolouchová, 2020 [ref. 88]).

3.4 Poly(2-alkyl-2-oxazolines) Functionalized with Fluorinated Ferrocenes

Strong ^{19}F MRI signals require materials with mobile magnetically equivalent fluorine atoms and high fluorine content.[248, 257] In the pursuit of novel redox-responsive materials for DDSs traceable by ^{19}F MRI, we designed polymers containing trifluoromethylated ferrocenes as the sensing units. Unlike our previously studied systems, these polymers were anticipated to change their ^{19}F MRI signal in response to ROS species, due to the proximity of fluorine atoms to the ferrocene moiety. Simultaneously, the oxidation of the ferrocene moieties to charged ferrocenium species was expected to trigger nanoparticle disassembly and potential drug release.

3.4.1 Design and Multigram Synthesis of Fluorinated Ferrocenes

^{19}F nuclei will experience the strongest changes in relaxation times and chemical shift when they are close to the ferrocene moiety that is being oxidized. However, introducing strong electron-withdrawing groups, such as the trifluoromethyl group, to the ferrocene moiety can significantly increase its redox potential. The resulting redox potential of the polymer-bound ferrocene derivative could thus impact the ease and rate of oxidation/disassembly of nanoparticles formed from these amphiphilic polymers. Furthermore, fluorinated groups tend to increase material lipophilicity markedly, and highly fluorinated materials may even exhibit both hydro- and lipophobicity (*i.e.*, fluorophilic behavior). [258] Therefore, we prepared polymers based on different fluorinated ferrocene chemotypes **9** and **12,** with two or one -CF_3 group, respectively (Scheme 11). [109]

Scheme 11. Synthesis of fluorinated ferrocenes with a pendant amine (MW – microwave); (reproduced from Švec, 2022 [ref. 109]).

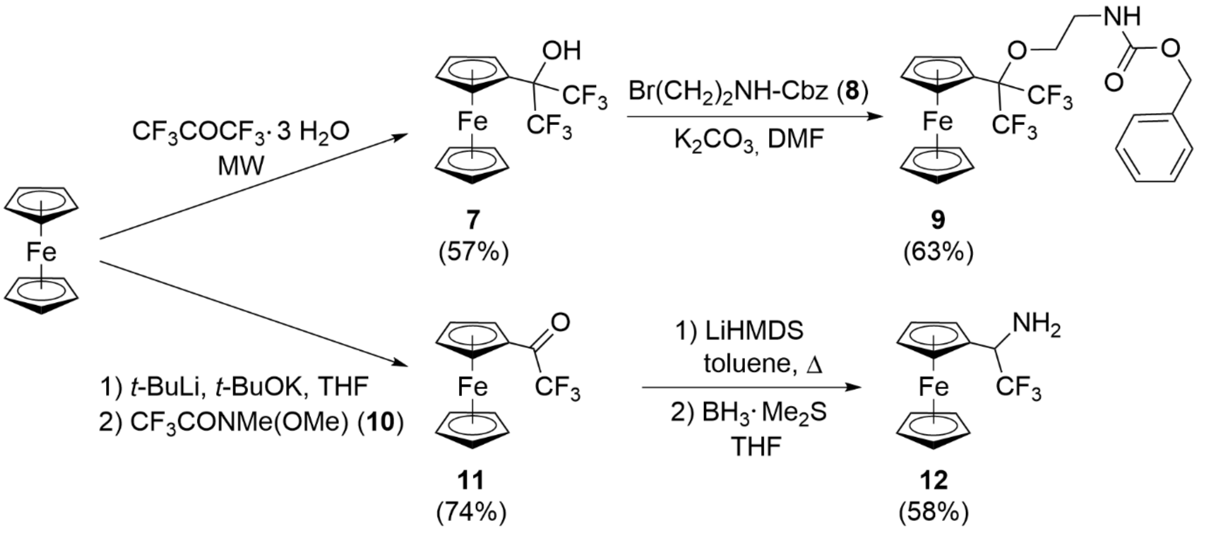

Compound **7** was synthesized by a previously reported microwave-assisted Friedel-Crafts-like reaction. [259] After optimizing the reaction conditions, we scaled up the fluorinated precursor synthesis to multigram amounts. The amine group necessary for amide coupling with the polymer was introduced by Williamson ether synthesis using the alkylating agent **8** with a Cbz-protected amine. The hydroxyl group in compound **7** is considerably acidic due to the two geminal electron-withdrawing -CF_3 groups (the p*K*a of hexafluoroisopropanol is 9.3, [260] and the phenyl analog of **7** has a p*K*a = 8.8[261, 262]). This led to the relatively high yield of the S_N2 reaction leading to the desired product **9** (63%). The Cbz amine protecting group in compound **9** was chosen for its fast and clean cleavage by hydrogenation and the subsequent straightforward free amine isolation by simple filtration.

The synthesis of the second fluorinated ferrocene with a pendant amino group (**12**) started with 2,2,2-trifluoroacetylferrocene (**11**), which can be prepared by acylation of ferrocene with trifluoroacetic anhydride in the presence of $AlCl_3$ as the catalyst (Friedel-Crafts-like reaction). [263] Unfortunately, this approach had very low yields (≈15%). Furthermore, the product purification on a larger scale was rather demanding. Therefore, we prepared **11** on a larger scale by selective ferrocene monolithiation[264] followed by a reaction with the Weinreb amide of trifluoroacetic acid (**10**). This reaction yielded the product on a multigram scale and allows further upscaling.

In the next step towards the final amine **12**, the ketone moiety had to undergo reductive amination. Reductive amination is commonly performed through *in situ* imine formation and subsequent reduction with sodium cyanoborohydride or related agents. However, under these conditions only the product of ketone reduction ((2,2,2-trifluoro-1-hydroxyethyl)ferrocene) was isolated. Perfluoromethylated ketones are known to perform poorly in reductive amination with sodium cyanoborohydride. [265] However, a previously reported procedure for 1-aryl-2,2,2-trifluoroethylamine synthesis from the corresponding ketones[265] finally allowed us to prepare more than 1 g of pure **12** during a single run. Compound **12** was isolated by a relatively simple flash chromatography on silica without any basic additive in the mobile phase, which indicates the low basicity the amino group, *vide infra*. We also converted amine **12** converted into its corresponding acetamide **13** (for structure see Figure 18C) in order to study its electrochemical behavior (low-molecular weight counterpart for polymers modified with compound **12**).

3.4.2 Block Poly(2-alkyl-2-oxazolines) with Fluorinated Ferrocene Moieties

A series of three diblock copoly(2-oxazoline)s (A_{Me}, B_{Me} and C_{Me}; Scheme 12) was targeted to have a first block consisting of a statistical MeOx (2-methyl-2-oxazoline)/ MestOx (2-(3-methoxy-3-oxopropyl)-2-oxazoline) [266] copolymer intended for coupling with the fluorinated ferrocene moieties (the hydrophobic block) and a second hydrophilic PMeOx block.

The block copolymers were prepared by the cationic ring-opening polymerization (CROP) of the respective monomers using acetonitrile as a solvent and MeOTs (methyl 4-methylbenzenesulfonate) initiator at 140 °C. To avoid excessive hydrophobicity of the ferrocene-containing block, statistical copolymerization of MestOx with hydrophilic MeOx was used to prepare the first block. Furthermore, hydrophobic statistical copolymers may offer certain advantages over block copolymers (see also section *3.5*), such as higher mobility and hydration of the core, which potentially leads to longer T_2 [267] and higher drug loading capacity. [268]

After complete consumption of both monomers, the second portion of MeOx was added, and the polymerization was continued to yield the second block of hydrophilic MeOx homopolymer ensuring water solubility and colloidal stabilization. The content of MestOx repeating units in the three copolymers was different, whereas the target block molar ratio and the target total theoretical degree of polymerization (DP = 100) was kept the same in all polymers ([MeOx-MestOx]:[MeOx] = 40:60). The methyl ester side chains were then hydrolyzed into carboxylic acids (polymers **A**-**C**; for polymer dispersities and molecular weights see Table 4).

Scheme 12. Synthesis of starting polyoxazolines with a pendant carboxyl group; (reproduced from Švec, 2022 [ref. 109]).

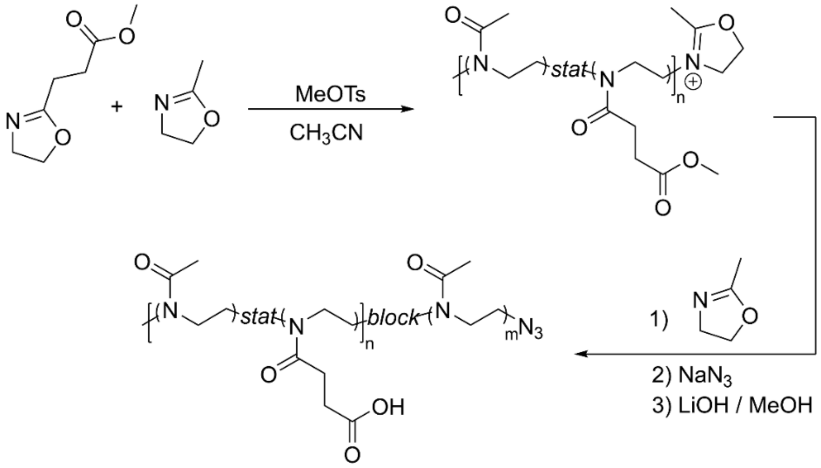

The free carboxyl groups in the three polymers **A**-**C** were subsequently coupled with the fluorinated ferrocenes using (benzotriazol-1-yloxy)tripyrrolidinophosphonium hexafluorophosphate (PyBOP). The amine **14** (Scheme 13) with two -CF_3 groups was prepared by deprotecting **9** by hydrogen with a Pd/C catalyst in MeOH directly prior to coupling with polymers. Amide coupling proceeded smoothly with compound **14** and PyBOP leading to virtually full conversion of the carboxyl groups (polymers **FcF6-A**, **FcF6-B**, and **FcF6-C** with 5, 10, and 15 mol% fluorinated ferrocene moiety content; determined by ^{1}H NMR). These values translate to 5-11 wt% fluorine content (Table 4). Polymers **FcF6-A** and **FcF6-B** were soluble/dispersable in water at room temperature, and polymer **FcF6-C** dissolved/dispersed in water after brief heating to approximately 50 °C without any apparent precipitation when cooling to room temperature (c = 20-30 mg · mL^{-1}). [109]

Scheme 13. Synthesis of the final polymers: amide coupling with **8** (R = -CF$_3$, Y = -CH$_2$CH$_2$O-) or **6** (R = -H, Y= void; racemate); (reproduced from Švec, 2022 [ref. 109]).

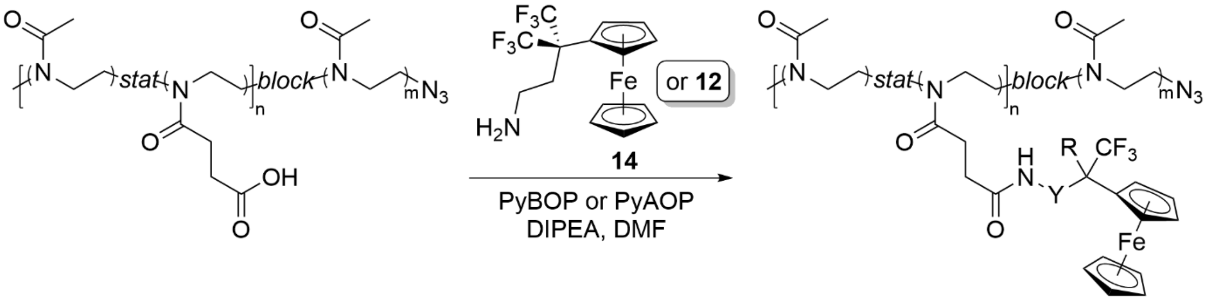

The fluorine content in compound **12** due to the presence of only one -CF$_3$ group. For this reason, only polymer **C** with the highest amount of free carboxyl groups was chosen for modification with this fluorinated ferrocene moiety. By applying the same conditions as with **14**, the carboxyl group conversion in the reaction of **C** with **12** was always incomplete. Furthermore, a relatively high amount of (2-hydroxyethyl)amide moieties (coupling reactions were quenched with 2-hydroxyethylamine) was observed. Polymer **FcF3-C1** (Table 4) contained 6.8 mol% of ferrocene moieties and 5.8 mol% of *N*-(2-hydroxyethyl)amide moieties. This phenomenon is most likely caused by low nucleophilicity (and basicity, as mentioned above in section *3.4.1*) of the amino group in compound **12**. Therefore, we decided to employ a more reactive coupling agent (7-azabenzotriazol-1-yloxy)tripyrrolidinophosphonium hexafluorophosphate (PyAOP) and added the agent separately in two portions. This modified coupling procedure yielded polymer **FcF3-C2** with a high functionalization degree (13 mol%), but the high functionalization was unfortunately accompanied by higher polymer dispersity than in **FcF6 A-C** and **FcF3-C1** (Table 4). As with the FcF6 polymers, the most hydrophilic polymer of the FcF3 chemotype (**FcF3-C1**) was soluble/dispersable at room temperature, whereas the polymer with the highest ferrocene content (**FcF3-C2**) required heating to 60 °C for dissolution/dispersion (no apparent precipitation occurred after cooling to room temperature). Although **FcF3-C2** should be theoretically less hydrophobic than its **FcF6-C** analog, the former is almost insoluble in water without heating the sample but apparent precipitation takes place upon cooling. This kinetically impeded solubility could be explained by a higher structural rigidity in **FcF3-C2** (T_g = 98 °C for **FcF3-C2** vs. 80 °C for **FcF6-C**; see Table S5 and Figure S36 in Appendix 5). [109]

Table 4. Molecular weight and dispersity as determined by SEC-MALS, proportion of ferrocene-containing repeating units (*Fc % r.u.*) as determined by NMR in DMSO-*d6*, and the corresponding calculated weight content of fluorine in the polymers.

Polymer	M_w [a] **[kDa]**	**Đ** [a]	**Ferrocene % r.u.** [b]	**Fluorine [wt %]**
A	11	1.03	-	-
B	9.66	1.03	-	-
C	8.52	1.03	-	-
FcF6-A	12.8	1.03	5	5.3
FcF6-B	14.2	1.04	10	8.9
FcF6-C	16.8	1.01	15	11
FcF3-C1	14.9	1.02	6.8	3.4
FcF3-C2	25.8	1.14	13	5.8

[a] Determined by SEC; the d*n*/d*c* in a mixture (80:20 vol.%) of MeOH and aqueous AcONa buffer (0.3 M, pH = 6.5) at 620 nm and 29 °C: d*n*/d*c* (**FcF6-C**) = 0.183 ± 0.005 mL · g^{-1}; d*n*/d*c* (**FcF3-C1**) = 0.187 ± 0.005 mL · g^{-1}; d*n*/d*c* (**FcF3-C1**) = 0.182 ± 0.009 mL · g^{-1};
[b] determined by ^{1}H NMR in DMSO-*d6*

3.4.3 Electrochemistry, Self-Association, Redox-Responsiveness, and ^{19}F MRI

Cyclic Voltammetry

The redox properties of the amphiphilic polymers and low-molecular-weight fluorinated ferrocene precursors were studied by cyclic voltammetry. Our results revealed that both the alcohol **7** and ether 9 undergo simple redox transitions attributable to reversible oxidation of the ferrocene moiety at 0.25 and 0.22 V *vs*. ferrocene/ferrocenium (Figure 18A). The oxidations of **7** and **9** occur at more positive potentials than the oxidation of parent ferrocene due to the electron-withdrawing groups, which hinder oxidation.

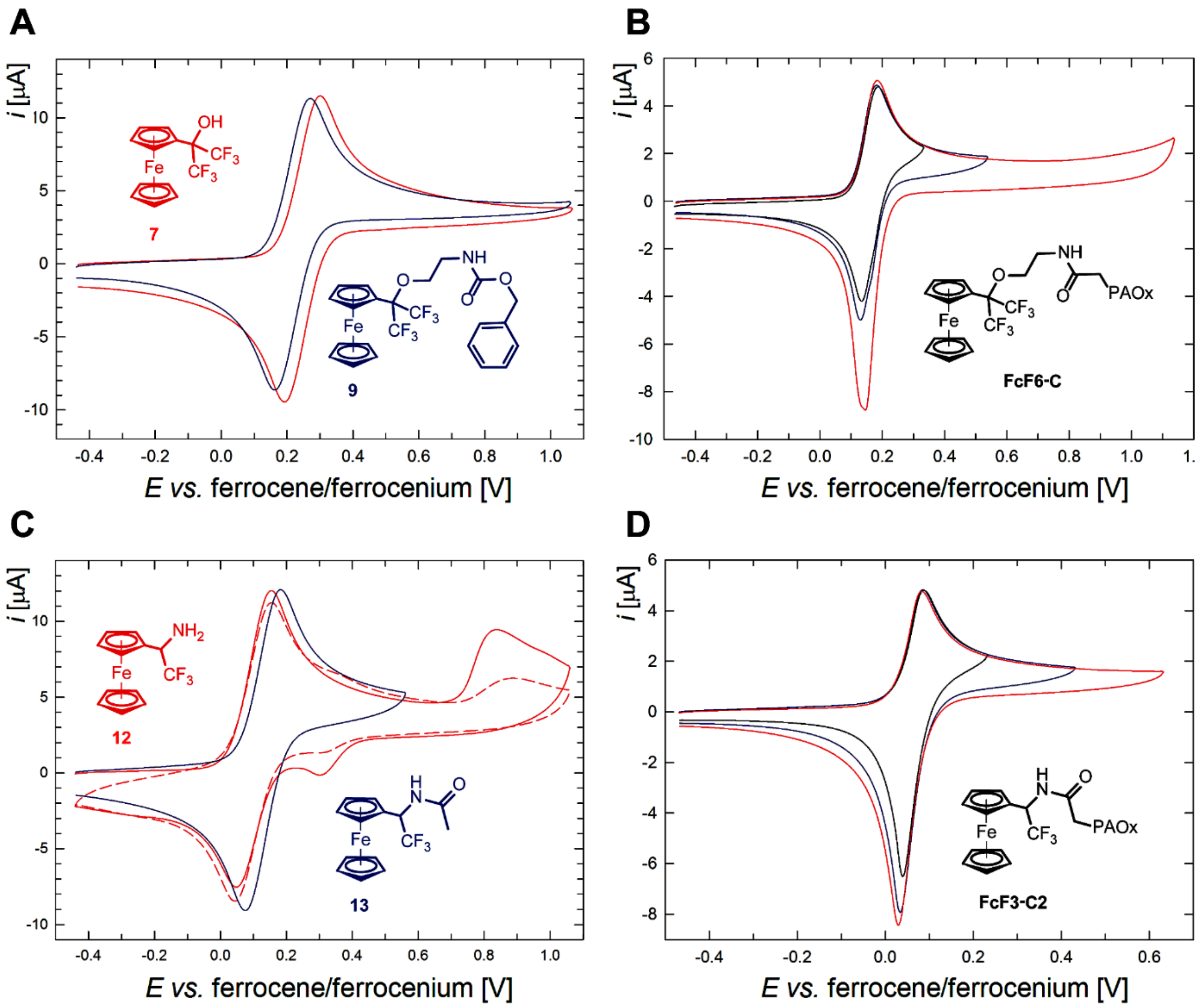

Figure 18. [A, C] Cyclic voltammograms of **7** and **9** (A) and **12** and **13** (C) as recorded in dichloromethane (0.1 M $Bu_4N[PF_6]$) on a glassy carbon disk electrode at 0.1 V · s^{-1} scan rate showing the first scans; the reversible nature of the redox transitions is maintained over the following scans except for **12**, for which the second scan is also shown by a dashed line. **[B, D]** Representative cyclic voltammograms recorded over different potential ranges for **FcF6-C** (B) and **FcF3-C2** (D) in dichloromethane under the same conditions; (reproduced from Švec, 2022 [ref. 109]).

The oxidation of compound **12** (one -CF_3 group), was also reversible ($E^{\circ\prime}$ 0.10 V) but followed by an irreversible process at more positive potentials (Figure 18C). The second wave, possibly caused by an irreversible amine moiety oxidation, [269] was associated with a weak reduction counter wave and changed its position and intensity in repeated scanning. In contrast, the amide **7** oxidation was electrochemically reversible and occurred at a more positive potential ($E^{\circ\prime}$ 0.13 V) than for the parent amine.

The $FcC(CF_3)_2OCH_2CH_2NHC(O)$- moieties in **FcF6-C** polymer were oxidized independently during a single redox event at potentials similar to that of compound **9** (anodic peak potential 0.19 V, see Figure 18B). However, the associated reduction was strongly affected by adsorption of the oxidized polymer on the electrode surface. The redox behavior of polymers **FcF6-C** and **FcF6-B** was virtually identical. Similarly, the redox responses of the polymers **FcF3-C2** and **FcF3-C1** did not differ from each other and were comparable to those of **FcF6-C** and **FcF6-B**, except for the lower oxidation potential of the amido-ferrocene pendants in **FcF3-C2** (Figure 18D) and **FcF3-C1**. This shift to lower potentials stems from the presence of only one -CF_3 group and a less electronegative nitrogen atom at the pivotal carbon atom (anodic peak potentials: 0.08 V). [109]

Dynamic Light Scattering and Cryogenic Transmission Electron Microscopy

Polymer responsivity to ROS (oxidation) in aqueous environments was assessed using DLS and cryogenic transmission electron microscopy (cryo-TEM). Polymers with fluorinated ferrocene moieties can be oxidized using hydrogen peroxide. However, similarly to the oxidation of ferrocene with H_2O_2, this reaction is autocatalytic, with relatively slow kinetics. [242] Furthermore, the ferrocenium species decompose by atmospheric oxygen or by reactions with nucleophiles on a longer timescale. [270-274] To perform a fast and controlled oxidation, we used ammonium peroxydisulfate (APS) as the oxidant together with a $CuCl_2$ catalyst. Under these Fenton-like conditions, the polymers of the FcF3 chemotype were fully oxidized almost instantaneously, whereas polymers of the FcF6 chemotype with two CF_3 groups on the ferrocene moiety became gradually oxidized with an induction period of approximately 1 min. [109]

The polymers **FcF6-A** and **FcF6-B** formed micelles with a hydrodynamic diameter (D_h) from 10 to 20 nm, whose size did not change significantly upon oxidation (possible slight swelling observed during **FcF6-A** oxidation, Figure 19A). In contrast, the D_h of **FcF6-C** polymer particles was close to 100 nm (Fig 19B). This value does not correspond to the size of a “classical micelle” because the maximum theoretical diameter of a classical micelle is limited by the fully stretched polymer chain contour length (L), and, therefore, cannot exceed 2 L (for MeOx DP=100 approx. 70 nm). [275] Upon oxidation, the hydrodynamic diameter of the **FcF6-C** nanoparticles changed to approximately 20 nm, which is similar to that of unoxidized **FcF6-A** and **FcF6-B** (Figure S2, Appendix 5) nanoparticles. [109]

To better understand the DLS results, we examined the morphology of these nanoparticles by cryo-TEM. Cryo-TEM images of unoxidized **FcF6-C** revealed approximately 100-nm-long, thin “rod-like” particles resembling rod/worm-like micelles[268] and flake objects of a similar size (Figure 19C). The flake objects could be either different nanoparticles of **FcF6-C** or an artifact resulting from the cryogenic sample preparation process (such as the occasionally occurring “leopard skin” artifact of unclear origin).[276, 277] In contrast, oxidized polymer **FcF6-C** resembled classical micelles, as shown by the isometric objects, approximately 20 nm in size, observed in the cryo-TEM images (Figure 19D) and in line with our DLS results.[109]

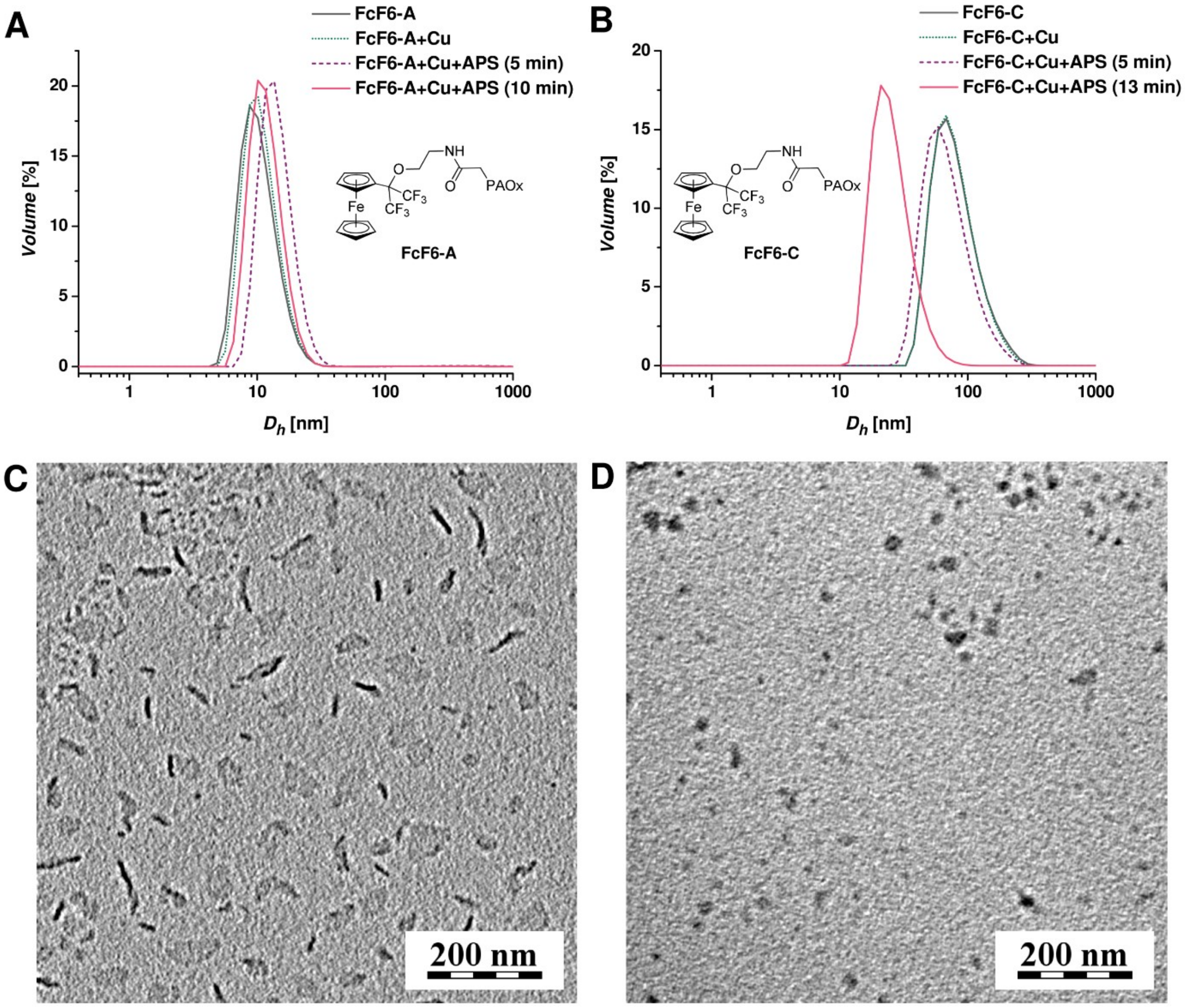

Figure 19. [A, B] Hydrodynamic diameter of **FcF6-A** and **FcF6-C** polymer samples (2 mg · mL^{-1}) dissolved in citrate buffer (0.08 M, pH = 6.2) before oxidation, after Cu^{2+} (catalytic amount) addition, and after APS addition at different timepoints. **[C]** Cryo-TEM image of **FcF6-C** dissolved in citrate buffer (0.08 M, pH = 6.2). **[D]** Cryo-TEM image of **FcF6-C** dissolved in citrate buffer (0.08 M, pH = 6.2) after oxidation with APS; (reproduced from Švec, 2022 [ref. 109]).

The D_h of **FcF3-C1** and **FcF3-C2** nanoparticles was lower than that of FcF6 samples (approximately 10 nm). In contrast to the nanoparticles (NPs) derived from FcF6 polymers, the NPs formed from **FcF3-C1** and **FcF3-C2** at least partly disintegrated to unimers upon oxidation (Figure 20A and Figure S8 in Appendix 5). However, after 6 min, the D_h returned to higher values indicating a gradual re-association process. The cryo-TEM images of aqueous **FcF3-C1** sample (Figure 20B) showed micelle-like particles, which disappeared after oxidation (image not shown). [109]

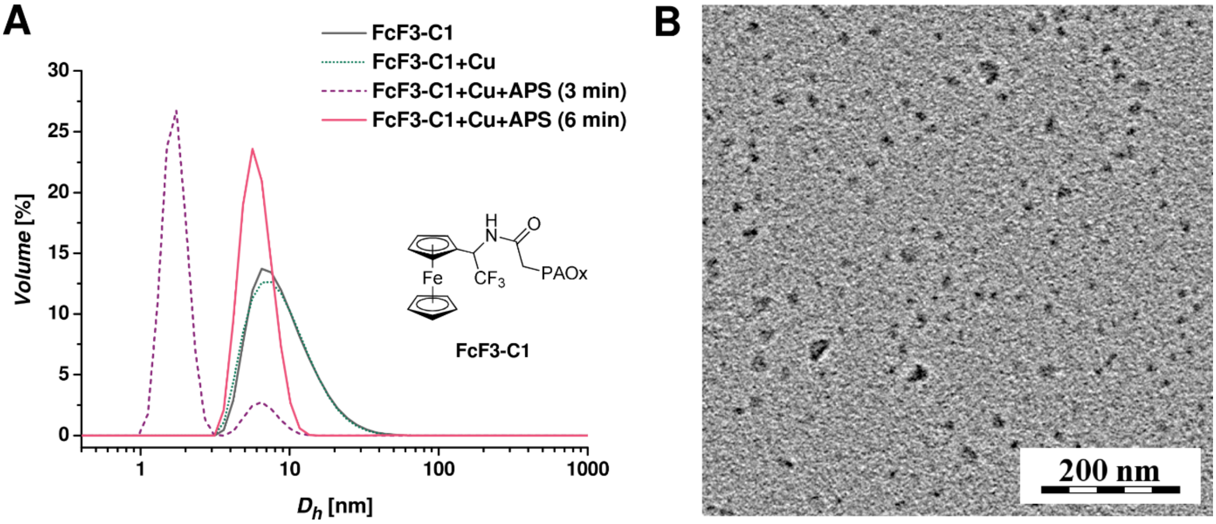

Figure 20. [A] Hydrodynamic diameter of **FcF3-C1** polymer samples (2 mg · mL^{-1}) dissolved in citrate buffer (0.08 M, pH = 6.2) before oxidation, after Cu^{2+} (catalytic amount) addition, and after APS addition at different timepoints. **[B]** cryo-TEM image of **FcF3-C1** dissolved in citrate buffer (0.08 M, pH = 6.2); (reproduced from Švec, 2022 [ref. 109]).

The substantially different behavior of FcF6 and FcF3 polymer chemotypes during oxidation suggests that the (hexafluoroisopropyl)ferrocenyl moiety remains significantly hydrophobic after its oxidation to ferrocenium and/or that the oxidation of the ferrocene moieties in FcF6 polymers is incomplete even when using a strong oxidating agent such as peroxydisulfate. These two proposed mechanisms may act together, as the ferrocene redox potential increases significantly in a non-polar environment. [245] Furthermore, high hydrophobicity decreases the amount of reactive oxygen species available in the nanoparticle core. During the oxidation, the aqueous polymer samples changed from orange-brown (ferrocene) to blue (ferrocenium); more specifically, the FcF3 samples turned deep blue instantaneously after adding APS, whereas FcF6 always reached only a faint blue-green hue even when using a high excess of APS (the incomplete oxidation was also supported by the results of the NMR/MRI experiments, see section *NMR and MRI Properties*). [109]

Cytotoxicity

Cytotoxicity of the FcF3 and FcF6 polymers was assessed using the standard 3-(4,5-dimethylthiazol-2-yl)-2,5-diphenyltetrazolium bromide (MTT) assay. We selected a human prostate cancer PC3 cell line known for its considerably high ROS levels[278] and normal human dermal fibroblast (NHDF) line served as the "ROS-negative" control. In general, the polymers had no negative effect on cell viability of the NHDF line, but the two highest polymer concentrations (1.0 and 0.75 $mg \cdot mL^{-1}$) had a minor, albeit significant, negative impact on the viability of PC3 cells after 24 h incubation for 24 h (Figure S30-S31 in Appendix 5). These results indicated that both FcF3 and FcF6 polymers were slightly cytotoxic to cancer cells that produce high amounts of ROS. This could be explained by the fact that both the oxidation of the ferrocene moieties to ferrocenium and the subsequent, gradual release of Fe(II) by hydrolysis may cause cytotoxicity by generating additional ROS species through Fenton-type pathways. [279-281]

NMR and MRI Properties

Fluorinated ferrocenes **14** and **12** are diamagnetic, while their corresponding oxidized ferrocenium counterparts are paramagnetic. Similarly to (*tert*-butyl)ferrocene and isopropylferrocene, the trifluoromethyl groups in **14** and **12** should exhibit low rotational barriers, thus allowing high group mobility at room temperature. [282] Accordingly, the DMSO-*d6* solutions of FcF6 and FcF3 polymers exhibited sharp signals in ^{19}F NMR (FWHM = 0.02 kHz) at -72.3 and -75.8 ppm, respectively (Figure 21B). The ^{19}F NMR peak of the polymer was always accompanied by two ^{19}F NMR signals with low integral intensities but distinctively sharp peaks. These minor signals likely derived from slow oxidation and decomposition of the ferrocene moieties by atmospheric oxygen and therefore represent unavoidable impurities. Higher impurity signal was observed in the more hydrophilic polymers (Figure 21A), which further supported our hypothesis of "hydrophobically hindered" ferrocene moiety oxidation (see also section *Dynamic Light Scattering and Cryogenic Transmission Electron Microscopy*).

When dissolved in water, FcF6 and FcF3 polymers formed nanoparticles. With a few exceptions, [88, 249] polymer aggregation significantly decreases T_2 (and/or T_2^*) and increases T_1 due to the lower mobility of the polymers. This is generally an undesirable effect for MRI imaging because the decrease in the T_2-to-T_1 ratio lowers the signal-to-noise ratio and leads to longer acquisition times. As expected, the decrease in T_2 due to FcF6 and FcF3 polymer aggregation strengthened with the increase in polymer hydrophobicity. Consequently, **FcF6-C** and **FcF3-C2** exhibited shorter spin-spin relaxation times (T_2 0.4 and 1.6 ms, respectively) than their more hydrophilic counterparts **FcF6-A** and **FcF3-C1** (T_2 8.2 and 6.9 ms, respectively).[109]

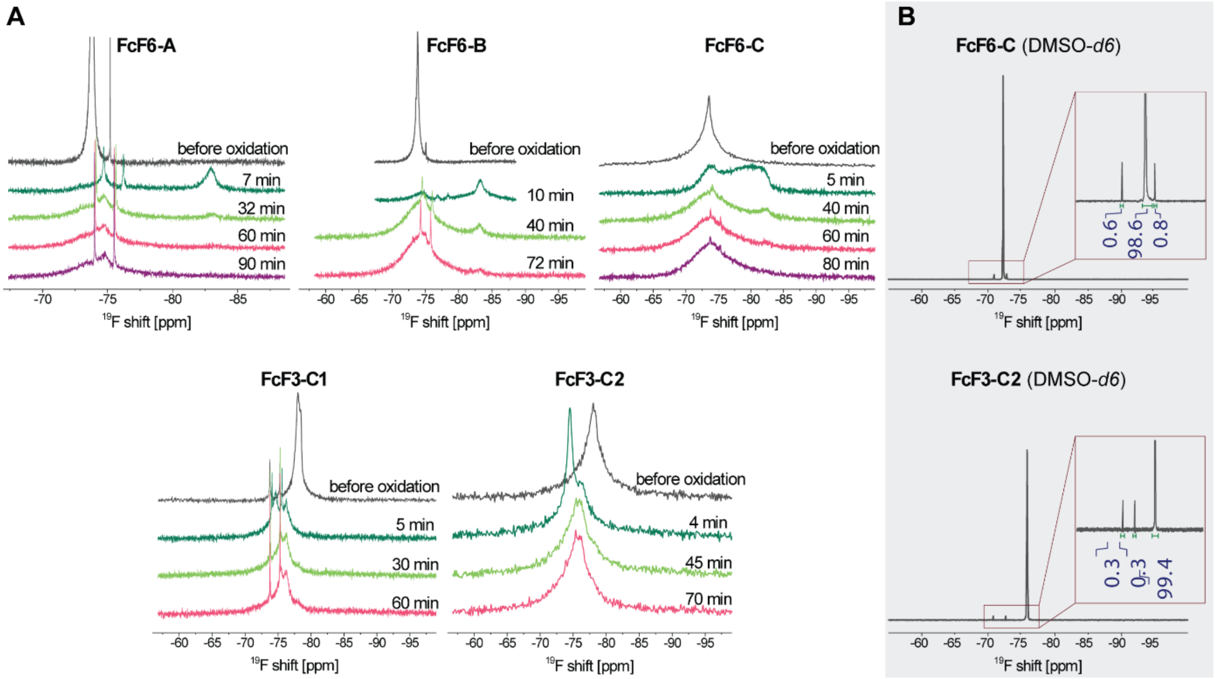

Figure 21. [A] ^{19}F NMR spectra of **FcF6-A**, **-B**, **-C**, **FcF3-C1**, and **FcF3-C2** in citrate buffer (0.08 M, pH=6.2) at B_0 = 11.75 T. The timepoints indicate the time elapsed after adding APS to the sample. The ^{19}F chemical shifts are referenced to external $CFCl_3$. **[B]** ^{19}F NMR spectra of **FcF6-C** and **FcF3-C2** in DMSO-*d6*; (reproduced from Švec, 2022 [ref. 109]).

The polymer oxidation effect on ^{19}F NMR parameters differed between FcF3 and FcF6 chemotypes. However, these chemotypes follow a similar reaction pathway via a short-living (~10 min) intermediate stage with the sharpest changes in NMR lineshape and T_1 relaxation. For the FcF6 chemotype, this stage of oxidation manifests as broadening and shifting of the ^{19}F peak around -73 ppm to a lower frequency (upfield) and as a second peak that emerges around -82 ppm (Figure 21A). For the FcF3 chemotype, the peak at -77 ppm shifts to a higher frequency (downfield), and the second peak emerges at -73 ppm (Figure 21A). These changes are accompanied by a decrease of more than one order of magnitude in the T_1 relaxation time.[109]

The second ^{19}F peak emerging during oxidation is attributed to the newly formed paramagnetic ferrocenium. Paramagnetic metal centers are known to shift the NMR frequency of the nucleus, and the value and sign of this shift is determined by the electron spin – nuclear spin coupling.[231, 283] The second ^{19}F peak appeared at opposite sides to the original peaks in FcF6 versus FcF3 polymers (upfield vs. downfield, respectively). At the early stage of oxidation (Figure 21A), these two ^{19}F signals may be interpreted as a transient coexistence of both ferrocenium and ferrocene moieties. The concomitant faster T_1 of the ^{19}F signal is attributed to the paramagnetic relaxation enhancement (PRE) caused by the Fe^{III} of ferrocenium (Fe^{II} in ferrocene is diamagnetic). The moieties with unoxidized ferrocene also exhibited enhanced ^{19}F T_1 relaxation resulting from the surrounding paramagnetic species and higher mobility due to polymer hydrophilization/nanoparticle disassembly, which caused the T_1 distribution to spread to 100 ms and lower values. In contrast, the T_2 relaxation did not exhibit dramatic changes at this early stage of oxidation. This observation could be explained by two opposing oxidation effects on T_2 – PRE of the ferrocenium moieties (lowering T_2) and by polymer hydrophilization/ nanoparticle disassembly (increasing T_2 and/or T_2^*). Considering the high T_1/T_2 ratio and the micelle size, unlike in smaller dendrimer systems, [284] in our FcF3 and FcF6 systems, the ^{19}F relaxation conditions approach the solid-state limit where T_1 and T_2 have an opposite dependence on the molecular mobility. In other words, polymer nanoparticle disintegration and the concomitant increase in molecular mobility would lead to longer T_2 and shorter T_1 values. The formation of paramagnetic ferrocenium upon oxidation further shortens the T_1 values while counteracting the increase in T_2. [109]

As the reaction proceeded, the newly formed peak gradually disappeared in both FcF3 and FcF6, whereas the parent peak was shifted and broadened compared to the reduced polymer (except for the initially broad spectrum of **FcF3-C2** where the oxidation effect on the FWHM may be disregarded because the peak is already broad) (Figure 21A). Two different phenomena may explain the displacement of this peak from the original ^{19}F chemical shift. On the one hand, both polymer micelles and "free" unimers are present but a fast chemical exchange now gives rise to an average signal. This explanation is also supported by DLS measurements, especially for FcF3 polymers. In **FcF3-C1** and **FcF3-C2**, after their initial "oxidative" disintegration, the nanoparticles gradually re-associate, albeit considerably less so than in the starting polymers. On the other hand, ferrocenium compounds gradually decompose similarly to ferrocenium. Ferrocenium reacts with common nucleophiles (*e.g.*, water and chloride ions) and oxygen. These reactions partly regenerate ferrocene and form Fe^{II} and Fe^{III} ions together with other byproducts such as, cyclopentadiene, cyclopenta-2,4-dien-1-one, and cyclopent-4-ene-1,3-dione, which can further react through Diels-Alder reactions leading to complex mixtures of products. [270, 271, 274] A small amount of regenerated ferrocene units on the polymer chain inevitably leads to fast ferrocenium-ferrocene electron self-exchange, as shown by NMR line broadening.[75, 76] The ^{19}F NMR signals did not change any further 60 min after oxidation and the blue color caused by ferrocenium had dissapeared completely. T_1 relaxation times increased at the late stage of the reaction towards the initial values but exhibited a wider distribution. In some samples of oxidized polymers, T_1 determination was negatively affected by minor impurities, which, however, display long T_1 and very sharp peaks compared to the significantly broadened signal of the redox tracers. [109]

Contrast in MR images is most often achieved by spatial variation of nuclear spin relaxation properties. In general, 3 quantities can be used: T_1 (spin-lattice relaxation time), T_2 (spin-echo decay time) and T_2^* (free induction decay time, $T_2^* \leq T_2$). The short ^{19}F T_2 relaxation times of the FcF3/ FcF6 polymers in aqueous medium render the most common echo-based MRI pulse sequences impractical and require FID-based techniques (free induction decay). Hence, we employed the ultrashort echo time (UTE) MRI sequence in FID mode. [285, 286] The difference in chemical shift of the reduced and oxidized state is an excellent tool for probing the redox state of our tracers by ^{19}F MRS (magnetic resonance spectroscopy) and ^{19}F MRI. Yet, this property also presents a challenge because chemical shift is used to encode spatial information in MRI. The first approach to resolve this issue was late-stage imaging of the oxidized sample because only a single ^{19}F NMR peak was present 60 min after sample oxidation. The second approach included selective excitation to exclusively visualize ^{19}F signal of the ferrocenium species. [109]

Figure 22 shows axial views of a 5-mm NMR tube filled with **FcF6-A** in aqueous medium before and after oxidation (late stage, >60 min). The top two images were acquired with the UTE parameters for MRI contrast based on T_1 relaxation enhancement upon oxidation. The bottom images show MR images of the same sample, exploiting the difference in signal FWHM (note the respective ^{19}F NMR spectra shown above the images). In FcF6 polymers, the ^{19}F line broadening resulting from oxidation yielded a significantly better contrast than the T_1 relaxation enhancement (6:1 vs. 1:2). [109]

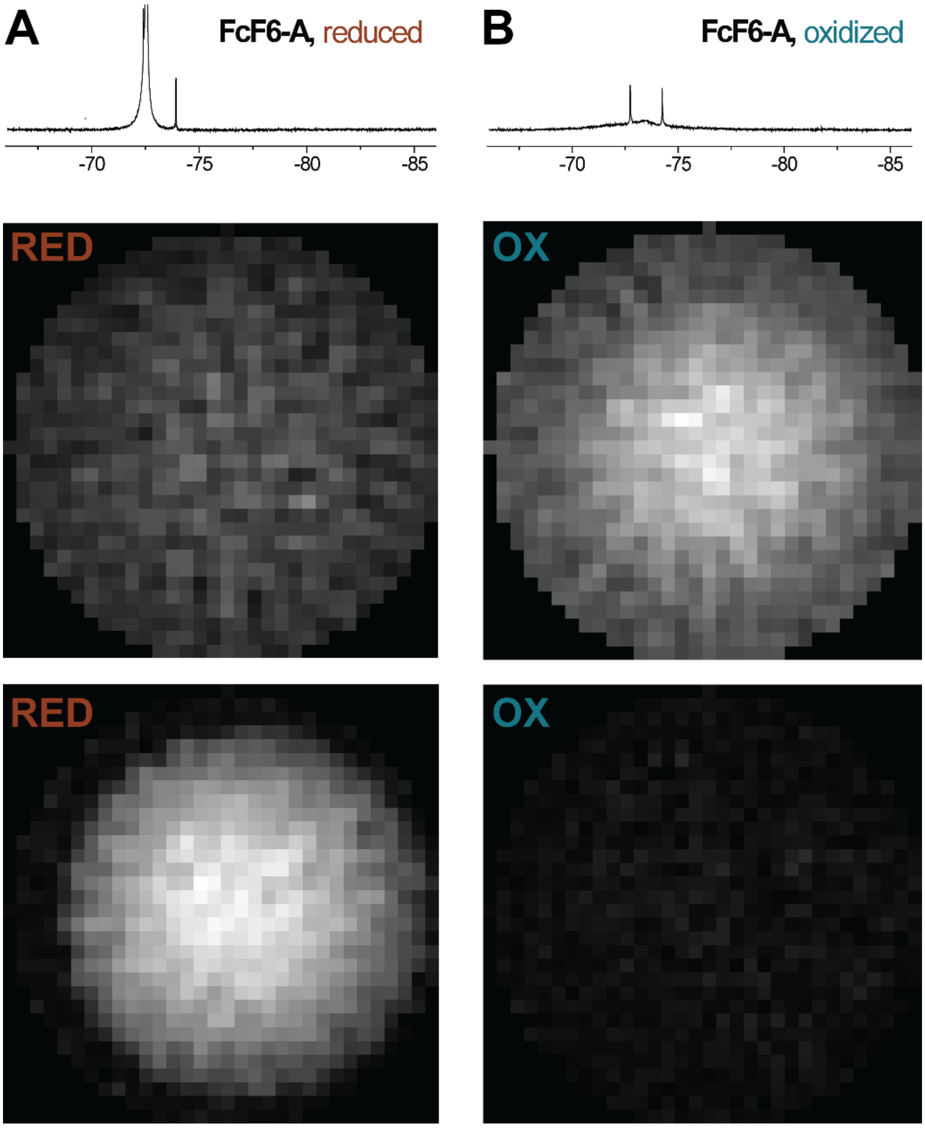

Figure 22. FcF6-A: ^{19}F NMR spectra and ^{19}F UTE images of a polymer sample (18 mg · mL^{-1}) in citrate buffer (0.08 M, pH=6.2) before (A) and after oxidation (B) with APS (> 60 min). The UTE provides a circular field of view (d = 5 mm, the inscribed circles in the square images), the tube position is slightly shifted with respect to the center (tube inner diameter d = 4.2 mm). A blurring of sample edges in (B) is due to the greater FWHM of the ^{19}F NMR signal. *Top:* UTE parameters set in favor of the oxidized sample with a shorter T_1: 22 µs acquisition delay; 10.5 ms repetition time; 90° flip angle. The brighter image is displayed in the full range of a 16-bit grayscale, whereas the darker image is rescaled according to its true intensity ratio. *Bottom:* UTE parameters set in favor of the reduced sample with a slower ^{19}F FID (a narrower spectral peak): 680 µs acquisition delay; 11.2 ms repetition time; 12° flip angle; (reproduced from Švec, 2022 [ref. 109]).

FcF3-C1 and **FcF3-C2** polymers offered good contrast when exploiting the T_1 relaxation enhancement (>4:1), but unlike **FcF6-A** and **FcF6-B**, showed no contrast related to differences in FWHM because the ^{19}F signal of FcF3 polymers is already broad in the reduced state. The short T_2 relaxation of the diamagnetic reduced polymers results from the low mobility of the nanoparticle core and may be improved by altering the polymer composition or changing the structure of the fluorinated ferrocene moieties. For example, switching the trifluoromethyl substituents for difluoromethyl groups may significantly reduce the hydrophobicity[287, 288] and, therefore, increase mobility and make the tracers suitable for echo-based MRI pulse sequences when using of a T_2 contrast scheme. [109]

Of all our polymers, **FcF6-A** gave the highest contrast ^{19}F images. The Figure 23A illustrates the contrast between the reduced and oxidized state of this polymer within a single image - axial view of coaxial NMR tubes (the inner tube is filled with the reduced polymer and the outer tube with the oxidized polymer). The Figure 23B shows ^{1}H MRI contrast caused by paramagnetic relaxation enhancement of ^{1}H water signal in a common gradient echo experiment.

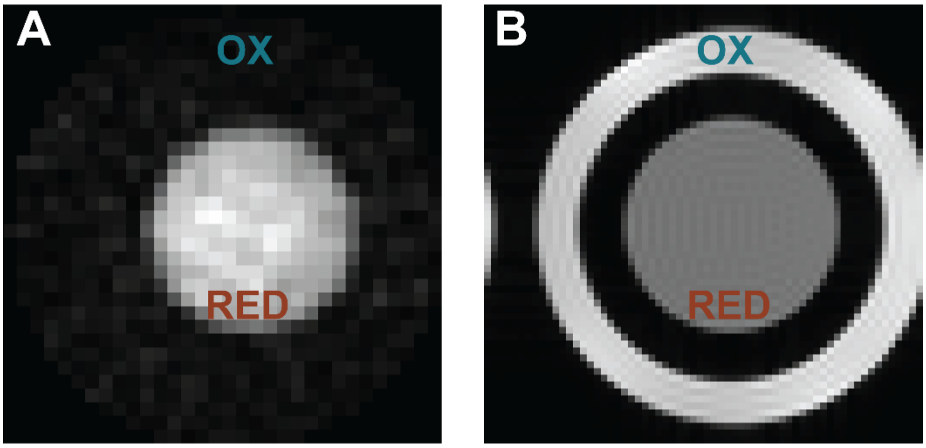

Figure 23. [A]: ^{19}F UTE image of a composite sample of **FcF6-A** (30 mg · mL^{-1}) in citrate buffer (0.08 M, pH=6.2) comprising two coaxial NMR tubes; the inner tube is filled with the reduced polymer and the outer with the oxidized polymer. The UTE parameters are identical to those shown in Figure 22 favoring the reduced sample. **[B]**: ^{1}H 64×64 FLASH image of the same sample, demonstrating paramagnetic relaxation enhancement of the ^{1}H water signal in the oxidized sample and outlining the geometry of the setup; (reproduced from Švec, 2022 [ref. 109]).

Furthermore, selective excitation may enable us to selectively detect ferrocenium species in **FcF6-A** or **FcF6-B** formed at an early stage of the oxidation process by exploiting the large (~10 ppm) difference in ^{19}F chemical shift between ferrocene and ferrocenium. In fact, we briefly tested this option in 2D UTE without performing any slice selection (Figure 24). When using selective excitation, the ^{19}F MRI signal derives solely from the “paramagnetic” ferrocenium species at -82 ppm. These selective pulses can be applied without any resolution restriction in the 3D UTE pulse sequence as long as the whole imaging experiment can be performed within the lifetime of the paramagnetic molecular tracer. [109]

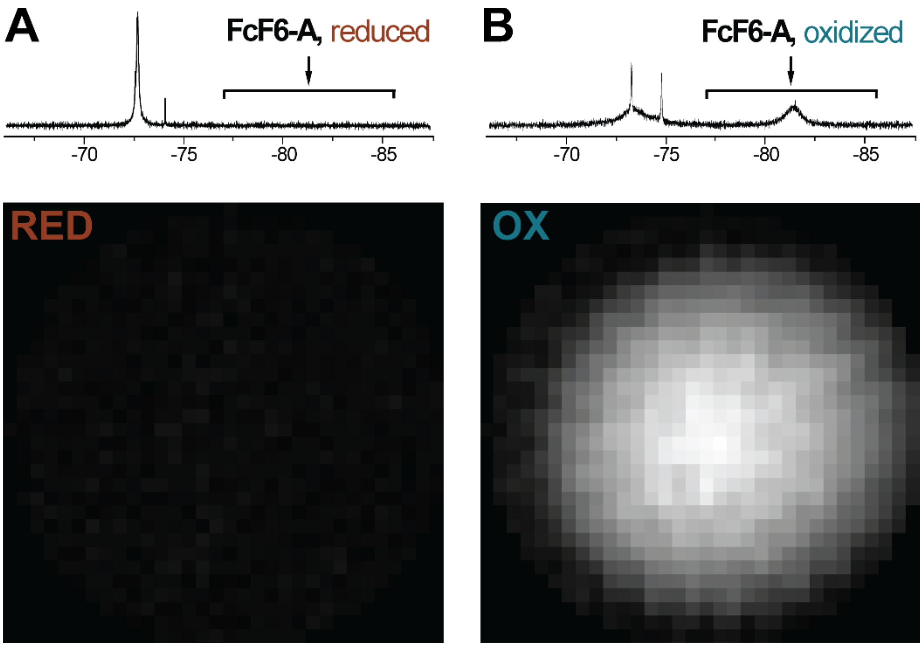

Figure 24. [A] ^{19}F UTE images of **FcF6-A** (16 mg · mL^{-1}) in citrate buffer (0.08 M, pH=6.2) before oxidation recorded with a frequency-selective pulse of a Gaussian shape. The carrier frequency of the pulse is indicated by the arrow and the excitation bandwidth by the brace in the spectra above the image. **[B]** ^{19}F UTE image of the sample shortly after oxidation with APS (~10 min), recorded with the same pulse sequence parameters as in Figure 24A. The MRI signal derives solely from the “paramagnetic” ^{19}F signal at -82 ppm, which enables us to detect the onset of **FcF6-A** oxidation directly from the emergence of the new peak; (reproduced from Švec, 2022 [ref. 109]).

The initial *in vitro* UTE experiments establish the link between MRI and redox-triggered FcF3/ FcF6 changes necessary for their potential biomedical applications as hybrid drug-delivery/ tracer materials. Based on these findings, suitable MRI methods may be thus further developed to fully exploit the properties of these new redox-responsive tracers.

3.5 Synthesis of Novel 2-Aryl-2-oxazolines: Gradient and Block Copolymers

This section directly compares the physicochemical properties of analogous gradient and block POx copolymers advantageously synthesized by living cationic copolymerization of 2-methyl-2-oxazoline (MeOx) with novel 2-aryl-2-oxazolines, evaluating their potential applications as drug delivery systems. We hypothesized that larger micelles with outer layer denser than the core ("bitterball" micelles),[267] formed by gradient copolymers, would exhibit higher drug loading (*DL*) than "traditional micelles" of analogous block copolymers. To test this hypothesis, we prepared three series of gradient and analogous block POx copolymers using MeOx as the hydrophilic monomer, and 2-phenyl-2-oxazoline (PhOx), 2-(4-butylphenyl)-2-oxazoline (BuPhOx), or 2-(4-butoxyphenyl)-2-oxazoline (BuOPhOx) as hydrophobic monomers. We also conducted copolymerization kinetic studies between MeOx and the respective co-monomers. This approach allowed us to assess the effect of substituents on the benzene ring on the polymer properties.

3.5.1 Scalable Multigram Procedure Towards Novel 2-Aryl-2-oxazoline Monomers

The two novel monomers BuPhOx and BuOPhOx were designed to increase side chain mobility compared to the relatively rigid poly(2-phenyl-2-oxazoline) (PPhOx). We have synthesized these monomers by 3 approaches. In the first unoptimized route (Scheme 14), 4-butyl/butoxybenzonitrile (**15**, **16**) were formed by a Sandmeyer reaction,[289] albeit in low yields (25% for 4-butylbenzonitrile and 4% for 4-butoxybenzonitrile), starting from commercially available 4-butyl/butoxyaniline. The Sandmeyer reaction is exothermic, but the cyanation of the unstable intermediate diazonium salt must be performed near 0 °C to eliminate thermal decomposition.[290] In our case of a 50 g-scale reaction mixture (≈ 900 mL), insufficient reaction heat removal capacity possibly caused a formation of side products and low reaction yields (Scheme 14).

Scheme 14. The unoptimized syntheses of BuPhOx (A) and BuOPhOx (B); (reproduced from Loukotová, 2021 [ref. 291]).

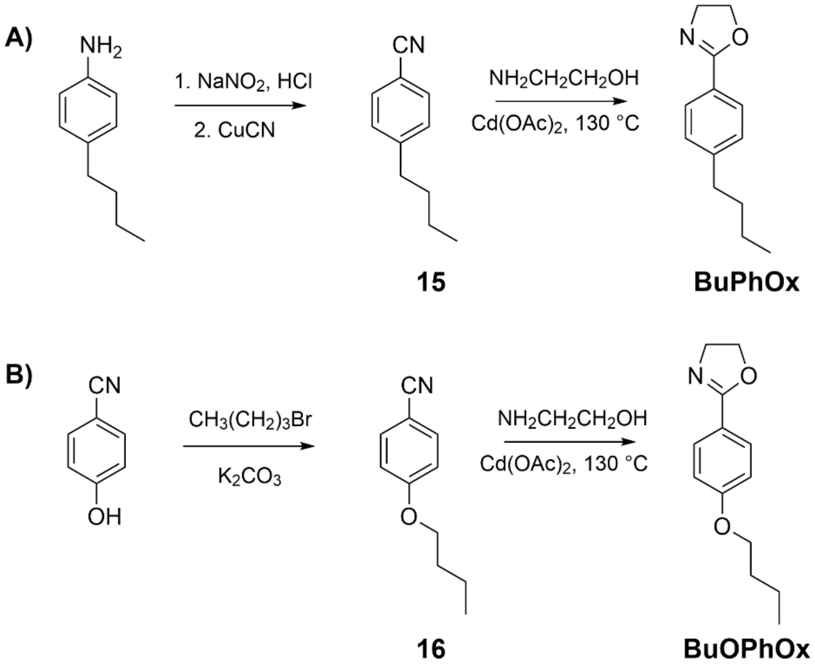

Alternatively to the Sandmeyer reaction route, 4-butoxybenzonitrile was synthesized by alkylating commercially available 4-cyanophenol with quantitative yield (99%, Scheme 14). The obtained nitriles **15** and **16** were reacted with ethanolamine using a Lewis-acid catalyst (cadmium acetate) according to Witte and Seeliger, [292] producing BuPhOx and BuOPhOx in mediocre yields (47% and 42%, respectively). To improve the unsatisfactory overall monomer yields (11% for BuPhOx and 42% for BuOPhOx) and to eliminate the toxic cadmium(II) acetate, the monomer synthesis was redesigned (Scheme 15). Acid chlorides were transformed into the corresponding 2-chloroethylamide derivatives **17** and **18** using 2-chloroethylamine. Subsequently, the intramolecular ring-closure promoted by a strong base (NaH) yielded the desired 2-oxazolines. [266] This method led to significantly improved overall yields (57% for BuPhOx and 63% for BuOPhOx). The structures of the intermediate amides were confirmed by ^{1}H-NMR (Figure 25, the presence of multiplet signals at 3.70-3.85 ppm for **17** and at 4.00-4.55 ppm for **18**, corresponding to the ethylene protons of the 2-chloroethyl moiety. The ^{1}H-NMR spectra of the final oxazoline monomers showed the characteristic triplet signals at 4.0 and 4.4 ppm, which correspond to the protons of the two methylene groups next to the nitrogen and oxygen atoms in the oxazoline ring, respectively.

Scheme 15. The synthesis of BuPhOx and BuOPhOx (reproduced from Loukotová, 2021 [ref. 291]).

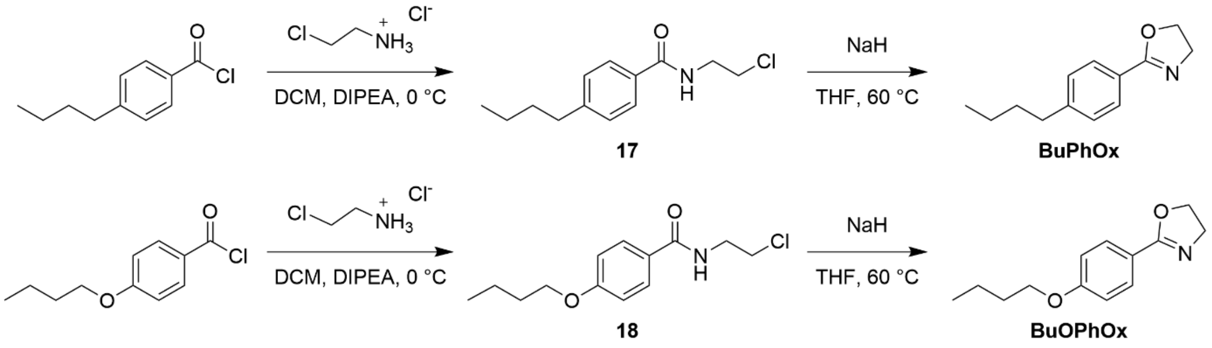

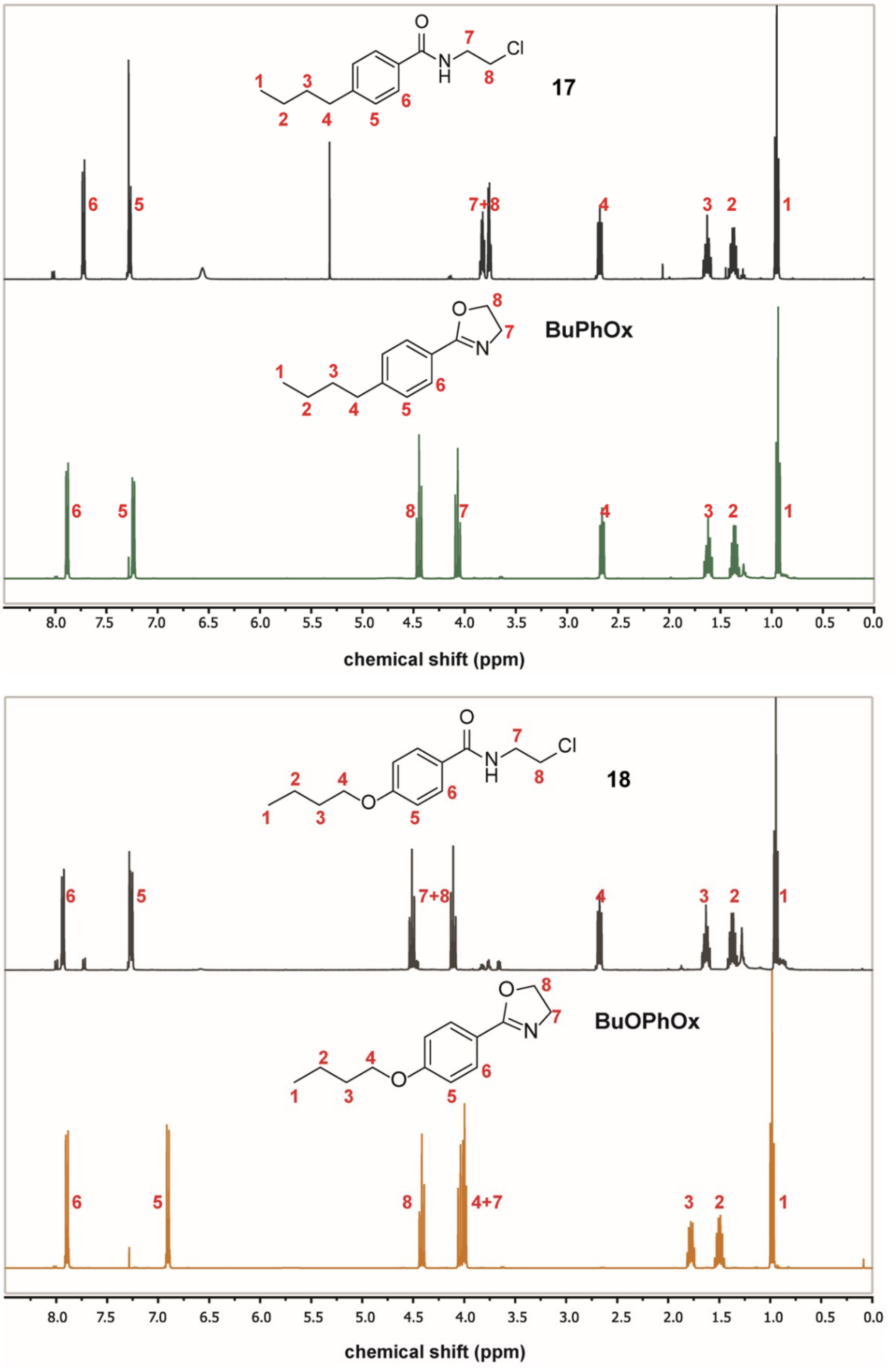

Figure 25. ^{1}H-NMR spectra of the intermediate products **17** and **18**, and BuPhOx and BuOPhOx. The spectra were recorded in $CDCl_3$ (reproduced from Loukotová, 2021 [ref. 291]).

3.5.2 Polymer Synthesis and Polymerization Kinetics

All POx copolymers were synthesized by living cationic ring-opening polymerization (CROP, LCROP). The block copolymers are formed when a single 2-oxazoline monomer is polymerized first, and the second monomer is added only after the first monomer has been consumed (Scheme 16A). In contrast, when two monomer species are present at the initiation (Scheme 16B), they both participate in the polymerization reaction yielding statistical copolymers. When the reactivities of the two monomers differ significantly, the resulting polymers will have a varying composition along the polymer chain. Such polymers are therefore referred to as gradient copolymers.

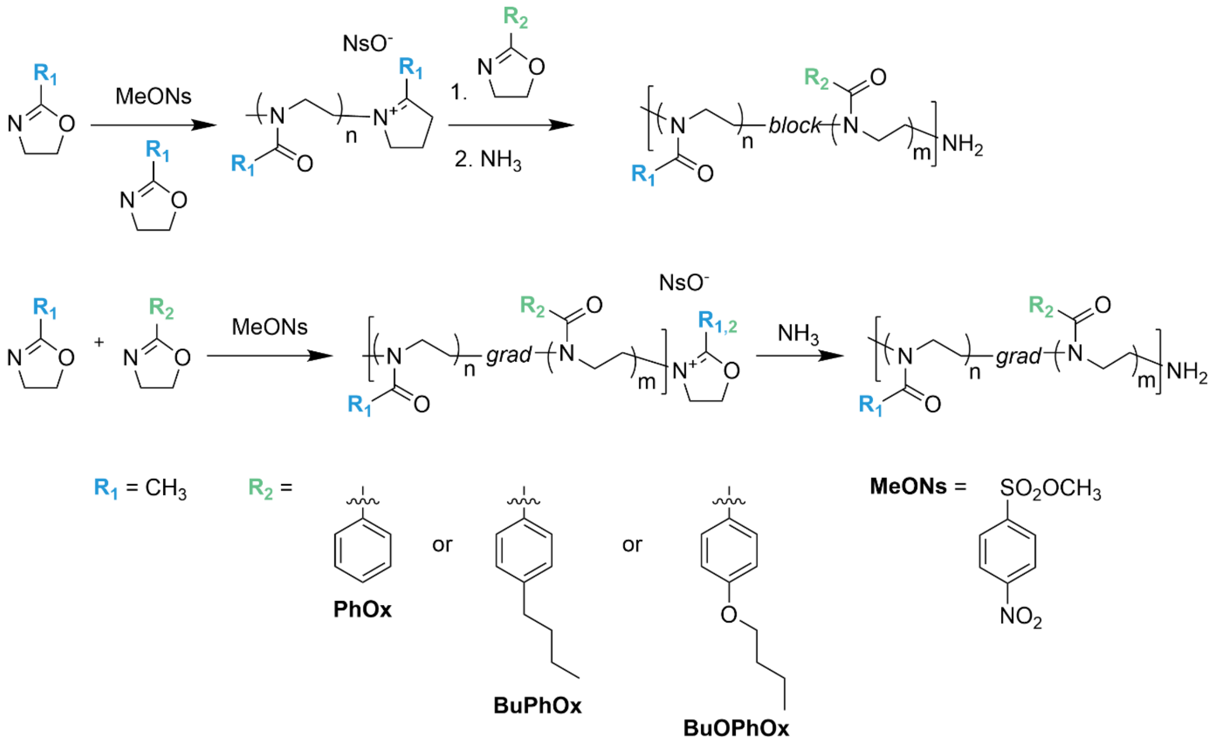

Scheme 16. General scheme of cationic ring-opening polymerization (CROP) of 2-aryl-2-oxazolines to produce block (A) and gradient (B) POx; (adapted from Loukotová, 2021 [ref. 291]).

To investigate the novel monomers, the kinetics of their homopolymerization (see Appendix 6 – Supporting Information) and copolymerization with MeOx were studied. The copolymerization kinetic experiments were performed using different monomer ratios ($[\mathrm{MeOx}]_0/[\mathrm{BuPhOx/BuOPhOx}]_0$ = 90/10, 80/20, 70/30, 50/50, 30/70 and 15/85). All copolymerization reactions displayed pseudo-first-order kinetics, while showing a linear increase in the measured M_n against the theoretical M_n, thus confirming the living character of these polymerizations. For both BuPhOx and BuPhOx copolymerization reactions, the faster consumption of MeOx and the slow incorporation of the 2-aryl-2-oxazoline were monitored. The monomer reactivity ratios in LCROP are usually determined based on the incorporated monomer fractions (F_1) at low conversion (~ 30%). The monomer fractions are plotted against the theoretical monomer fractions (f_1) and the r_1 and r_2 values are then calculated using nonlinear least squares fitting. [293] When the reactivity ratios are significantly different, the composition determination may be challenging due the negligible incorporation of the less reactive monomer. This is the literature-described case for the copolymerization of MeOx and PhOx ($r_{\mathrm{MeOx}} \gg 1$ and $r_{\mathrm{PhOx}} \ll 1$). [294] Thus, we implemented the approach described by *Schubert et al.* [295] using kinetic plots ($\ln([M]_0/[M]_t)$ versus time; see Appendix 6 – Figures S4-S15) for copolymerizations at different initial monomer ratios. The reaction time was set to achieve 30% MeOx conversions ($\ln(M_0/M_t) = 0.357$), and the actual second monomer conversion was determined at these time points. The monomer reactivity ratios were calculated by nonlinear least squares fitting of F_1 (incorporated fraction) versus f_1 (fraction in solution), see Figure 26A,B. A slightly lower r_{MeOx} was observed in the copolymerization with BuPhOx ($r_{\mathrm{MeOx}} = 7.56$, $r_{\mathrm{BuPhOx}} = 0.13$) in comparison with BuOPhOx ($r_{\mathrm{MeOx}} = 8.91$, $r_{\mathrm{BuPhOx}} = 0.12$), indicating a steeper chain composition gradient for copolymers of MeOx and BuOPhOx. To visualize the distribution of the monomeric units along the polymer chains, we simulated the microstructure composition for monomer feed ratios MeOx/BuPhOx or BuOPhOx = 70/30 using the Skeist model[296, 297] (Figure 26C). This simulation revealed that the initial part of the copolymer is rich in MeOx, while the final 10 to 20% of the chain consists of a BuPhOx or BuOPhOx homopolymer.

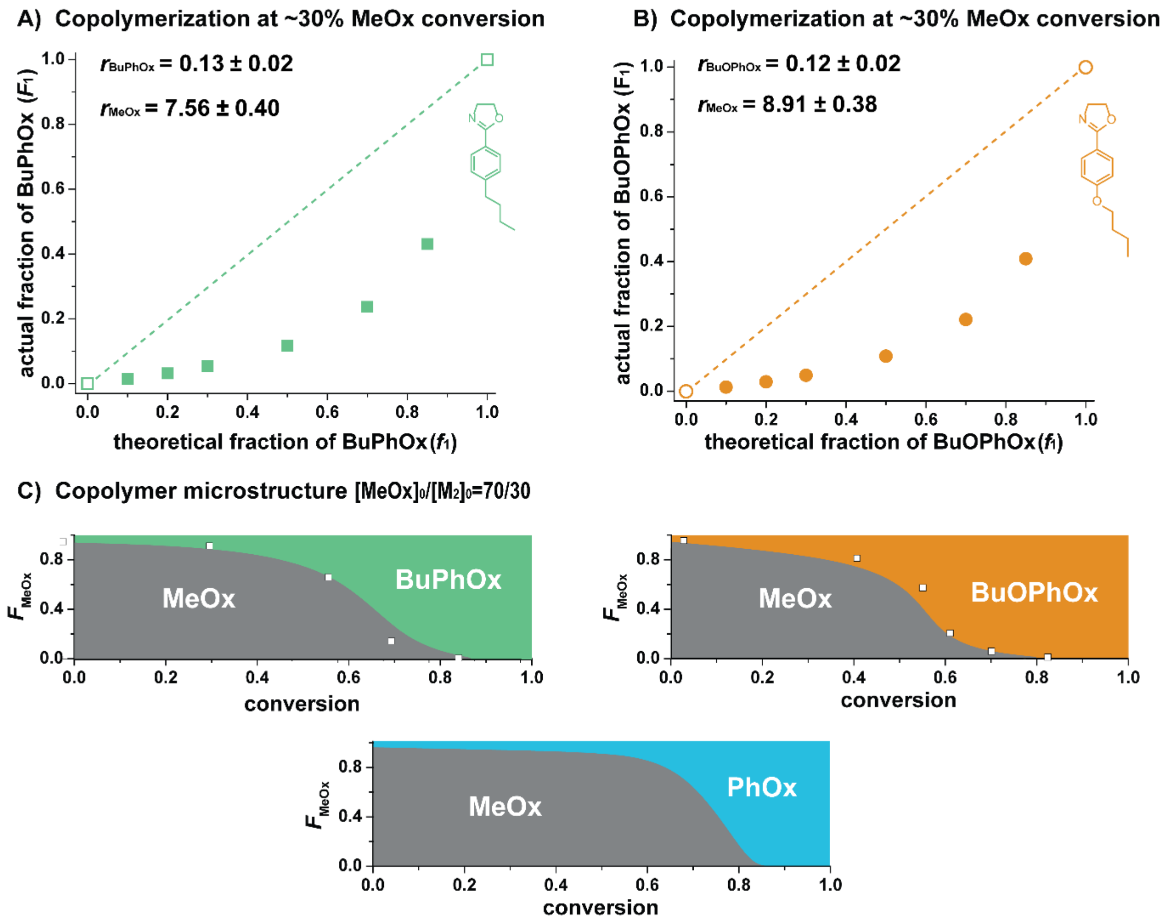

Figure 26. A) and B) Relationship between the fraction of BuPhOx/BuOPhOx in the monomer feed (f_1) and the fraction of BuPhOx/BuOPhOx incorporated into the copolymer (F_1) at 30 mol% MeOx conversion. C) Microstructure of the copolymers resulting from a feed containing monomers at a 70/30 ratio (based on the Skeist model) The white squares correspond to the real data. For the microstructure of PhOx copolymer, the literature data was used (r_{MeOx} = 10.02, r_{BuPhOx} = 0.02);[298] (reproduced from Loukotová, 2021 [ref. 291]).

Furthermore, three series of copolymers were prepared to directly compare properties of analogous gradient and block copolymers. In all copolymers, MeOx was used as the hydrophilic monomer, the hydrophobic monomer was different in each series: a) PhOx, b) BuPhOx, and c) BuOPhOx. In each series, polymers with varying hydrophobic/ hydrophilic monomer ratios were synthesized to assess the effects of each hydrophobic monomer on the polymer properties (10/90, 20/80, and 30/70 ratios). All obtained polymers had monomer compositions and molecular weights (M_w = 8,260 – 12,980 Da) close to the intended values and acceptable dispersity. With only a few exceptions, the dispersity of the final gradient polymers ($Đ$ = 1.03 – 1.21) was lower than that of the block copolymers ($Đ$ = 1.09 – 1.28). This could be explained by the introduction of impurities during the addition of the second monomer in block copolymerization reactions.

3.5.3 Comparison of Gradient and Block Copolymers – Nanoparticles and Drug Loading

Because the samples of gradient and analogous block copolymers exhibited similar molecular weights and ratios of hydrophilic and hydrophobic monomeric units (MUs) incorporated into the chain, we were able to investigate how their properties depend on the structure of the hydrophobic monomer and on the ratios of specific MUs in each macromolecule. [291] The general advantage of gradient copolymers is their straightforward one-pot single-step synthesis, whereas the preparation of block copolymers is a two-step process. Another literature-described advantage of gradient copolymers is their better solubility, [299] which we also observed in our study (Table S1 in Appendix 6).

PMeOx-*grad*-PhOx polymers form a specific type of nanoparticles with an outer layer denser than the core (the so-called "bitterball-core" micelles). [267] Thus, we investigated the incorporation of a drug inside the looser core of such NPs in comparison with the incorporation of the same drug into the "traditional" micelles of analogous block polymers. We chose the antibiotic drug rifampicin ($\log D = 1.3$) [300] the model compound. The rifampicin-loaded polymeric nanoparticles were prepared by nanoprecipitation ($m_{\text{polymer}}/m_{\text{rifampicin}} = 1/1$).

The hydrodynamic diameter of the rifampicin-loaded NPs was determined by DLS. In general, the gradient polymer NPs (D_h = 27 to 225 nm) were much smaller than their block counterparts (D_h = 66 to 302 nm), and all NPs displayed a relatively narrow hydrodynamic diameter distribution (Figure 27 and Table 3 in Appendix 6). We also observed that the formed NPs tend to be larger with increasing content of hydrophobic MUs in the polymer. The BuPhOx copolymers were significantly larger (D_h = 24 to 283 nm) than the analogous PhOx copolymers (D_h = 32 to 163 nm), which points to the higher hydrophobicity of BuPhOx caused by the butyl substituent on the phenyl ring. This effect was most pronounced in gradient copolymers with the highest amount of the hydrophobic monomer – D_h (PMeOx$_{70}$-*grad*-PhOx$_{30}$) = 72 nm and D_h (PMeOx$_{70}$-*grad*-BuPhOx$_{30}$) = 225 nm. [291] Interestingly, in polymers with the low ratio of hydrophilic/hydrophobic MUs = 90/10, the hydrophobic monomer type had negligible effect on the nanoparticle size with the gradient polymers (D_h = 20 to 32 nm) but strongly affected the size in the case of the block analogs (D_h = 66 to 187 nm, Figure 27A). All nanoparticle formulations displayed high colloidal stability upon 14-day storage (no change of the observed hydrodynamic diameter D_h after 14 days at room temperature), see Figure 27B. It should be noted that the polymeric NPs without rifampicin had a consistent D_h around 5 nm in when prepared from water-soluble copolymers. However, the NPs prepared from water-insoluble polymers varied more in size and their size reproducibility was lower.

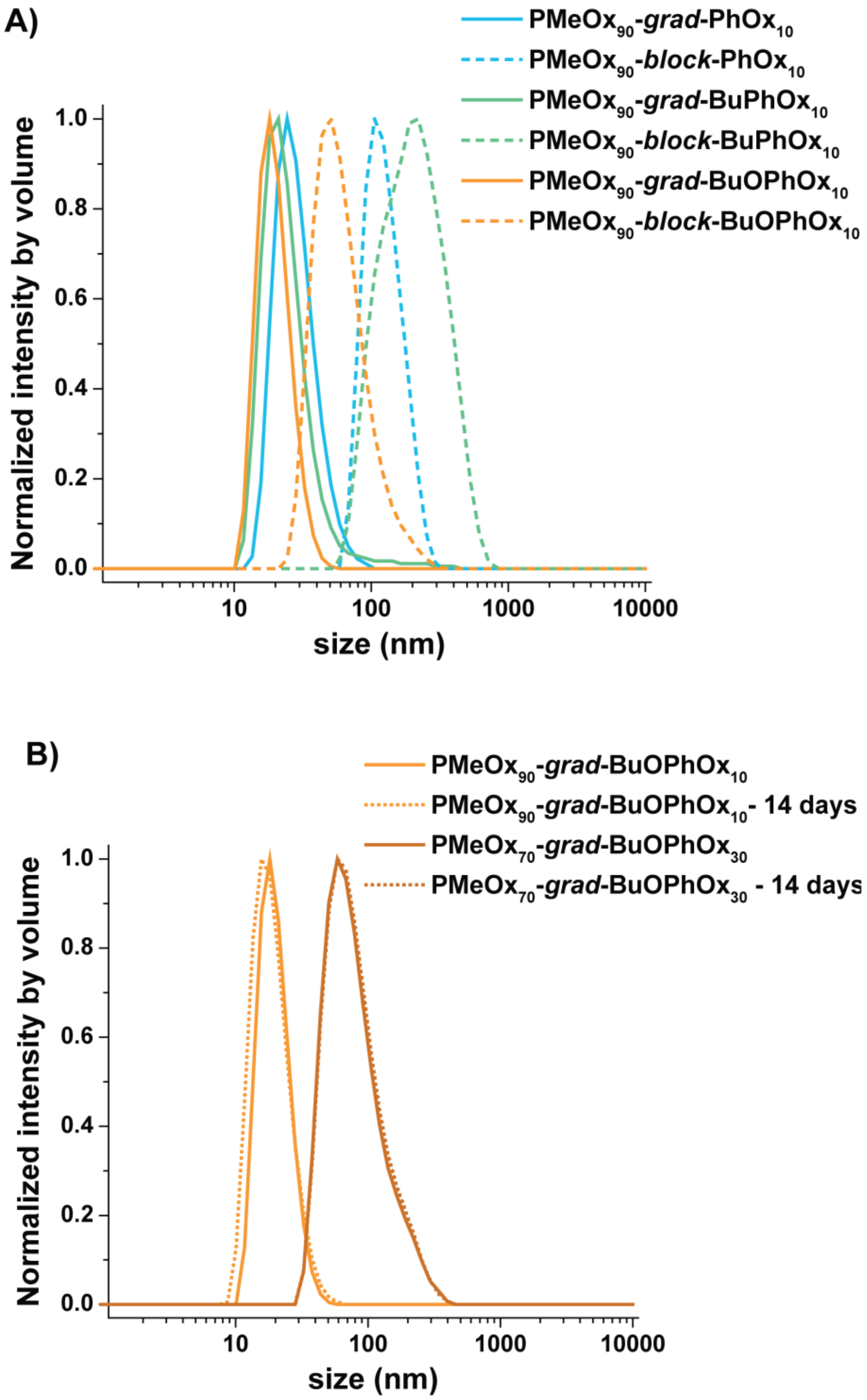

Figure 27. A) NPs size distributions by volume obtained by DLS - comparison of block and gradient polymer NPs loaded by rifampicin. A) NPs size distributions by volume obtained by DLS - comparison of block and gradient polymer NPs loaded by rifampicin and their stability upon 14 day storage; (reproduced from Loukotová, 2021 [ref. 291]).

The NP morphology of was observed by transmission electron microscopy (TEM). The samples were negatively stained in the presence of trehalose to stabilize the structure of NPs and mitigate material shrinkage caused by sample drying. [301] The PhOx copolymers formed spherical micelles with diameters similar to those obtained by DLS (Figure 28). However, the diameters detected by TEM were smaller than the diameters obtained by DLS which is caused by polymer shrinkage in its dry state (trehalose does not completely prevent the deformation of the NPs upon dehydration). Furthermore, DLS systematically overestimates NPs diameter because of the hydration layer. Despite having the same monomer ratios (MeOx/PhOx or BuPhOx or BuOPhOx = 80/20) and the same polymer architecture, the BuPhOx and BuOPhOx copolymers formed rod-like micelles with the lengths in line with the diameters detected by DLS (Figure 28; Figure S22-S23 and Table S5 in Appendix 6). In the BuPhOx and BuOPhOx copolymers, the number of spherical particles was ranging from minor to undetectable (except for the sub-10 nm fraction which was present in all samples). The monomeric unit of BuPhOx and BuOPhOx has 50% higher volume than the PhOx monomeric unit, and thus, the hydrophobic parts of $PMeOx_{80}$-$BuPhOx_{20}$ and $PMeOx_{80}$-$BuOPhOx_{20}$ have significantly higher volume compared to $PMeOx_{80}$-$PhOx_{20}$. This results in the formation of rod-like micelles because the shape of NPs containing a single amphiphile is controlled by the packing factor p proportional to the volume of the hydrophobic part ($0 < p \leq 1/3$ → spherical micelles, $0.406 < p \leq 1/2$ → rod-like micelless[302, 303]). [291]

Figure 28. TEM images of rifampicin-loaded NPs. Scale bar represents 200 nm ; (reproduced from Loukotová, 2021 [ref. 291]).

Using the same drug (rifampicin) we have also studied the copolymer drug loading capacity (*DL*,%) and drug entrapment efficiency (*EE*,%). The micelle content of rifampicin was determined by UV-Vis spectroscopy, and we analyzed the effect of the substituents on the aromatic ring of hydrophobic monomeric units as well as the influence of the hydrophilic/hydrophobic MU ratio on *EE* and *DL* (Figure 29).

EE was higher with the increasing content of hydrophobic MUs in P(MeOx-*grad*-PhOx) but remained almost constant in P(MeOx-*block*-PhOx). Consequently, P(MeOx$_{70}$-*grad*-PhOx$_{30}$) showed significantly higher *EE* (47.8%) than P(MeOx$_{70}$-*block*-PhOx$_{30}$) (33.0%). This is most likely because the gradient copolymer NPs have a less dense core ("bitterball-core") than their block counterparts, as already mentioned above. The results were similar for copolymers of

MeOx and BuPhOx, with P(MeOx$_{70}$-*grad*-BuPhOx$_{30}$) also showing a significantly higher *EE* (43.3%) than P(MeOx$_{70}$-*block*-BuPhOx$_{30}$) (35.4%). In contrast, gradient and block copolymers of MeOx and BuOPhOx had comparable *EE*s, albeit with slightly higher absolute values (43.2 to 51.9%) than PMeOx-PhOx and PMeOx-BuPhOx, possibly due to rifampicin interactions with BuOPhOx monomeric units. [291]

In general, *DL* reproduces the trends of *EE*. *DL* grew with the content of hydrophobic MUs in the gradient copolymers. The effect was stronger in P(MeOx$_{70}$-*grad*-PhOx$_{30}$) (32.3%) and P(MeOx$_{70}$-*grad*-BuPhOx$_{30}$) (30.2%) than in their block counterparts (24.8% and 26.1%, respectively). Similarly, the BuOPhOx copolymers had the highest absolute values of *DL* (30.2 to 34.2%), most likely due to rifampicin interactions with BuOPhOx monomeric units. [291]

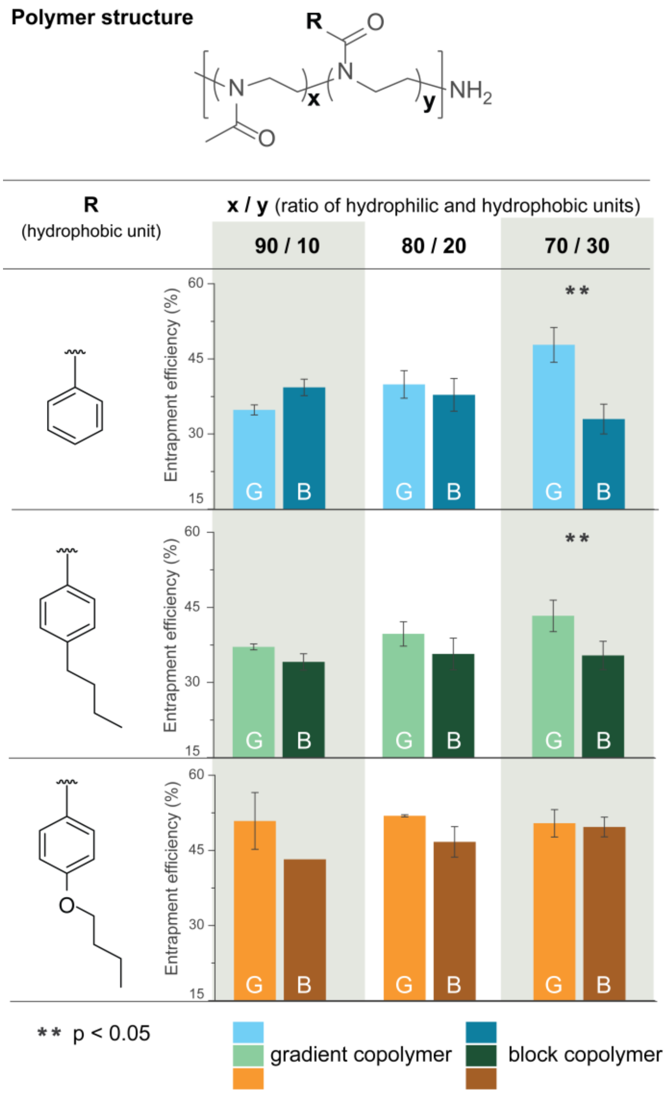

Figure 29. Comparison of entrapment efficiency between gradient and analogous block copolymers – effect of substituents and of ratios of monomeric units incorporated into the

polymer chain. All data are presented as mean ± standard deviation ($n = 3$); (reproduced from Loukotová, 2021 [ref. 291]).

4 Conclusion

This doctoral thesis presents advancements in the field of responsive polymer materials, focusing on their design, synthesis, and characterization to enhance polymer-based DDSs and develop theranostic materials. By utilizing a bottom-up approach, we aimed to create novel, well-defined responsive polymers, thereby improving and contributing to better efficiency and functionality of DDSs in the future.

One of the achievements of this thesis was the development of synthetic and derivatization strategies for new pyrazinacene-based materials. Pyrazinacenes, a type of heteroacenes formed from linearly-fused 1,4-pyrazine units, are redox-active, strongly colored, and fluorescent compounds with characteristics that make them promising candidates for designing new upconverting materials. Upconverting materials convert lower-energy photons to higher-energy photons, enabling the use of low-energy photons within the biological transparency window for processes that would otherwise require high-energy photons. We successfully described a novel and scalable one-pot synthesis of phenanthroline-fused pyrazinacenes from relatively inexpensive starting materials. The phenanthroline moiety was employed to form pyrazinacene complexes with Ru^{2+} ions, and a straightforward *N*-alkylation strategy was developed for the potential future conjugation of pyrazinacene upconversion materials with polymers.

This thesis also explored light-responsive micelle-like DDSs, based on a model amphiphilic block copolymer of (2-nitrobenzyl)acrylate. We reported the first controlled polymerization of (2-nitrobenzyl)acrylate using SET-LRP, leading to polymers with narrow dispersity. These block copolymers formed micelle-like particles in aqueous environment and readily disassembled upon UV irradiation. The UV-triggered disassembly makes these systems a valuable model for light-responsive, excretable micellar DDSs. Furthermore, by combining these polymers with upconverting materials in the future, not only UV but also low-energy photons within the biological transparency window could be used to trigger their disassembly.

We also presented fluorinated poly[(*N*-(alkyl)acrylamide)] and poly(2-oxazoline) polymer systems that are responsive to multiple physical and/or chemical stimuli. These fluorinated polymers were designed as potential theranostic materials applicable for stimuli-responsive DDSs traceable *in vivo* by ^{19}F MRI. The thermo-/pH- and thermo-/redox-responsive systems based on PDFEA have demonstrated both highly favorable ^{19}F MRI imaging properties and biocompatibility.

However, with thermo-/redox-responsive PDFEA polymers incorporating ferrocene, there was no observable change in the ^{19}F MRI signal upon oxidation. To address the possibility of ^{19}F MRI redox sensing, we synthesized two novel ferrocene derivatives with fluorine atoms in direct proximity to the ferrocene core and used them to modify POx copolymers. The resulting POx copolymers, decorated with fluorinated ferrocene moieties, formed nanoparticles that disassembled upon oxidation. They also exhibited significant changes in both the relaxation times and chemical shifts of the ^{19}F nuclei, which could be distinguished by ^{19}F MRI.

Finally, we described the synthesis of novel 2-aryl-2-oxazoline monomers and a first direct comparison of analogous amphiphilic gradient and block POx copolymers containing these monomers. Nanoparticles based on MeOx/2-aryl-2-oxazoline gradient copolymers exhibited improved drug loading capacity and higher hydration/mobility of the micelle core.

In conclusion, this doctoral thesis significantly contributes to the fields of light-, pH-, thermo-, and redox-responsive materials; polymer-based DDSs; and polymer-based ^{19}F MRI tracers.

5 References

1. Lendlein, A. Polymers in Biomedicine. *Macromolecular Bioscience* **2010**, *10*, 993.
2. Pearce, A. K.; O'Reilly, R. K. Polymers for Biomedical Applications: The Importance of Hydrophobicity in Directing Biological Interactions and Application Efficacy. *Biomacromolecules* **2021**, *22*, 4459.
3. Sung, Y. K.; Kim, S. W. Recent advances in polymeric drug delivery systems. *Biomaterials Research* **2020**, *24*, 12.
4. Peer, D.; Karp, J. M.; Hong, S.; Farokhzad, O. C.; Margalit, R.; Langer, R. Nanocarriers as an emerging platform for cancer therapy. *Nature Nanotechnology* **2007**, *2*, 751.
5. Lee, C.-Y.; Hu, S.-M.; Christy, J.; Chou, F.-Y.; Ramli, T. C.; Chen, H.-Y. Biointerface Coatings With Structural and Biochemical Properties Modifications of Biomaterials. *Advanced Materials Interfaces* **2023**, *10*, 2202286.
6. Smith, I. O.; Liu, X. H.; Smith, L. A.; Ma, P. X. Nanostructured polymer scaffolds for tissue engineering and regenerative medicine. *WIREs Nanomedicine and Nanobiotechnology* **2009**, *1*, 226.
7. Zhang, F.; King, M. W. Biodegradable Polymers as the Pivotal Player in the Design of Tissue Engineering Scaffolds. *Advanced Healthcare Materials* **2020**, *9*, 1901358.
8. Han, G.-Y.; Hwang, S.-K.; Cho, K.-H.; Kim, H.-J.; Cho, C.-S. Progress of tissue adhesives based on proteins and synthetic polymers. *Biomaterials Research* **2023**, *27*, 57.
9. Mir, M.; Ali, M. N.; Barakullah, A.; Gulzar, A.; Arshad, M.; Fatima, S.; Asad, M. Synthetic polymeric biomaterials for wound healing: a review. *Progress in Biomaterials* **2018**, *7*, 1.
10. Kumar, R.; Santa Chalarca, C. F.; Bockman, M. R.; Bruggen, C. V.; Grimme, C. J.; Dalal, R. J.; Hanson, M. G.; Hexum, J. K.; Reineke, T. M. Polymeric Delivery of Therapeutic Nucleic Acids. *Chemical Reviews* **2021**, *121*, 11527.
11. Elzes, M. R.; Mertens, I.; Sedláček, O.; Verbraeken, B.; Doensen, A. C. A.; Mees, M. A.; Glassner, M.; Jana, S.; Paulusse, J. M. J.; Hoogenboom, R. Linear Poly(ethylenimine-propylenimine) Random Copolymers for Gene Delivery: From Polymer Synthesis to Efficient Transfection with High Serum Tolerance. *Biomacromolecules* **2022**, *23*, 2459.
12. Mai, Y.; Eisenberg, A. Self-assembly of block copolymers. *Chemical Society Reviews* **2012**, *41*, 5969.
13. Lehn, J.-M. Perspectives in Chemistry—Steps towards Complex Matter. *Angewandte Chemie International Edition* **2013**, *52*, 2836.
14. Cartwright, J. H. E.; Mackay, A. L. Beyond crystals: the dialectic of materials and information. *Philosophical Transactions of the Royal Society A: Mathematical, Physical and Engineering Sciences* **2012**, *370*, 2807.
15. Cademartiri, L.; Bishop, K. J. M. Programmable self-assembly. *Nature Materials* **2015**, *14*, 2.
16. Whitesides, G. M.; Grzybowski, B. Self-Assembly at All Scales. *Science* **2002**, *295*, 2418.
17. Hrubý, M. Samoasociované polymerní systémy citlivé na vnější podněty. Habilitační práce, Univerzita Karlova v Praze, Praha, 2019.
18. Huang, Y.-X.; Wu, Z.-J.; Huang, B.-T.; Luo, M. Pathway and Mechanism of pH Dependent Human Hemoglobin Tetramer-Dimer-Monomer Dissociations. *PLOS ONE* **2013**, *8*, e81708.

19. Fong, C.; Le, T.; Drummond, C. J. Lyotropic liquid crystal engineering–ordered nanostructured small molecule amphiphile self-assembly materials by design. *Chemical Society Reviews* **2012**, *41*, 1297.
20. Long, J. A.; Rankin, B. M.; Ben-Amotz, D. Micelle Structure and Hydrophobic Hydration. *Journal of the American Chemical Society* **2015**, *137*, 10809.
21. Israelachvili, J. N. 20 - Soft and Biological Structures. In *Intermolecular and Surface Forces (Third Edition)*, Israelachvili, J. N. Ed.; Academic Press, 2011; pp 535.
22. Zhang, J.; Farias-Mancilla, B.; Destarac, M.; Schubert, U. S.; Keddie, D. J.; Guerrero-Sanchez, C.; Harrisson, S. Asymmetric Copolymers: Synthesis, Properties, and Applications of Gradient and Other Partially Segregated Copolymers. *Macromol. Rapid Commun.* **2018**, *39*, 1800357.
23. Kim, S.; Shi, Y.; Kim, J. Y.; Park, K.; Cheng, J.-X. Overcoming the barriers in micellar drug delivery: loading efficiency, in vivo stability, and micelle–cell interaction. *Expert Opinion on Drug Delivery* **2010**, *7*, 49.
24. Lu, Y.; Yue, Z.; Xie, J.; Wang, W.; Zhu, H.; Zhang, E.; Cao, Z. Micelles with ultralow critical micelle concentration as carriers for drug delivery. *Nature Biomedical Engineering* **2018**, *2*, 318.
25. Kapse, A.; Anup, N.; Patel, V.; Saraogi, G. K.; Mishra, D. K.; Tekade, R. K. Chapter 6 - Polymeric micelles: a ray of hope among new drug delivery systems. In *Drug Delivery Systems*, Tekade, R. K. Ed.; Academic Press, 2020; pp 235.
26. Adams, M. L.; Lavasanifar, A.; Kwon, G. S. Amphiphilic block copolymers for drug delivery. *Journal of Pharmaceutical Sciences* **2003**, *92*, 1343.
27. Nicolai, T.; Colombani, O.; Chassenieux, C. Dynamic polymeric micelles versus frozen nanoparticles formed by block copolymers. *Soft Matter* **2010**, *6*, 3111.
28. Ehrlich, P. Experimental researches on specific therapy: on immunity with special reference to the relationship between distribution and action of antigens: FIRST HARBEN LECTURE. In *The collected papers of Paul Ehrlich*, Elsevier, 1960; pp 106.
29. Williams, K. The introduction of 'chemotherapy' using arsphenamine – the first magic bullet. *Journal of the Royal Society of Medicine* **2009**, *102*, 343.
30. Braatz, D.; Cherri, M.; Tully, M.; Dimde, M.; Ma, G.; Mohammadifar, E.; Reisbeck, F.; Ahmadi, V.; Schirner, M.; Haag, R. Chemical Approaches to Synthetic Drug Delivery Systems for Systemic Applications. *Angewandte Chemie International Edition* **2022**, *61*, e202203942.
31. De, R.; Mahata, M. K.; Kim, K.-T. Structure-Based Varieties of Polymeric Nanocarriers and Influences of Their Physicochemical Properties on Drug Delivery Profiles. *Advanced Science* **2022**, *9*, 2105373.
32. Wouters, O. J.; McKee, M.; Luyten, J. Estimated Research and Development Investment Needed to Bring a New Medicine to Market, 2009-2018. *JAMA* **2020**, *323*, 844.
33. Lipinski, C. A. Rule of five in 2015 and beyond: Target and ligand structural limitations, ligand chemistry structure and drug discovery project decisions. *Advanced Drug Delivery Reviews* **2016**, *101*, 34.
34. Washington, N.; Washington, C.; Wilson, C. *Physiological Pharmaceutics: Barriers to Drug Absorption*; Taylor & Francis, 2000.
35. Levy, G.; Gibaldi, M. Pharmacokinetics. In *Concepts in Biochemical Pharmacology: Part 3*, Gillette, J. R., Mitchell, J. R. Eds.; Springer Berlin Heidelberg, 1975; pp 1.

36. Vargason, A. M.; Anselmo, A. C.; Mitragotri, S. The evolution of commercial drug delivery technologies. *Nature Biomedical Engineering* **2021**, *5*, 951.

37. Fink, C.; Sun, D.; Wagner, K.; Schneider, M.; Bauer, H.; Dolgos, H.; Mäder, K.; Peters, S.-A. Evaluating the Role of Solubility in Oral Absorption of Poorly Water-Soluble Drugs Using Physiologically-Based Pharmacokinetic Modeling. *Clinical Pharmacology & Therapeutics* **2020**, *107*, 650.

38. Mitchell, M. J.; Billingsley, M. M.; Haley, R. M.; Wechsler, M. E.; Peppas, N. A.; Langer, R. Engineering precision nanoparticles for drug delivery. *Nature Reviews Drug Discovery* **2021**, *20*, 101.

39. Mura, S.; Nicolas, J.; Couvreur, P. Stimuli-responsive nanocarriers for drug delivery. *Nature Materials* **2013**, *12*, 991.

40. Pearce, A. K.; O'Reilly, R. K. Insights into Active Targeting of Nanoparticles in Drug Delivery: Advances in Clinical Studies and Design Considerations for Cancer Nanomedicine. *Bioconjugate Chemistry* **2019**, *30*, 2300.

41. Zi, Y.; Yang, K.; He, J.; Wu, Z.; Liu, J.; Zhang, W. Strategies to enhance drug delivery to solid tumors by harnessing the EPR effects and alternative targeting mechanisms. *Advanced Drug Delivery Reviews* **2022**, *188*, 114449.

42. Fang, J.; Nakamura, H.; Maeda, H. The EPR effect: Unique features of tumor blood vessels for drug delivery, factors involved, and limitations and augmentation of the effect. *Advanced Drug Delivery Reviews* **2011**, *63*, 136.

43. Matsumura, Y.; Maeda, H. A New Concept for Macromolecular Therapeutics in Cancer Chemotherapy: Mechanism of Tumoritropic Accumulation of Proteins and the Antitumor Agent Smancs1. *Cancer Research* **1986**, *46*, 6387.

44. Nichols, J. W.; Bae, Y. H. EPR: Evidence and fallacy. *Journal of Controlled Release* **2014**, *190*, 451.

45. Maeda, H. Tumor-Selective Delivery of Macromolecular Drugs via the EPR Effect: Background and Future Prospects. *Bioconjugate Chemistry* **2010**, *21*, 797.

46. Flynn, T.; Wei, C. The pathway to commercialization for nanomedicine. *Nanomedicine: Nanotechnology, Biology and Medicine* **2005**, *1*, 47.

47. Rodríguez, F.; Caruana, P.; De la Fuente, N.; Español, P.; Gámez, M.; Balart, J.; Llurba, E.; Rovira, R.; Ruiz, R.; Martín-Lorente, C.; Corchero, J. L.; Céspedes, M. V. Nano-Based Approved Pharmaceuticals for Cancer Treatment: Present and Future Challenges. *Biomolecules* **2022**, *12*, 784.

48. National Cancer Institute, 2024. https://www.cancer.gov/nano/cancer-nanotechnology/current-treatments (accessed 2024 2nd June 2024).

49. He, H.; Liu, L.; Morin, E. E.; Liu, M.; Schwendeman, A. Survey of Clinical Translation of Cancer Nanomedicines—Lessons Learned from Successes and Failures. *Accounts of Chemical Research* **2019**, *52*, 2445.

50. Challenging paradigms in tumour drug delivery. *Nature Materials* **2020**, *19*, 477.

51. Danhier, F. To exploit the tumor microenvironment: Since the EPR effect fails in the clinic, what is the future of nanomedicine? *Journal of Controlled Release* **2016**, *244*, 108.

52. Hansen, A. E.; Petersen, A. L.; Henriksen, J. R.; Boerresen, B.; Rasmussen, P.; Elema, D. R.; Rosenschöld, P. M. a.; Kristensen, A. T.; Kjær, A.; Andresen, T. L. Positron Emission

Tomography Based Elucidation of the Enhanced Permeability and Retention Effect in Dogs with Cancer Using Copper-64 Liposomes. *ACS Nano* **2015**, *9*, 6985.

53. Sindhwani, S.; Syed, A. M.; Ngai, J.; Kingston, B. R.; Maiorino, L.; Rothschild, J.; MacMillan, P.; Zhang, Y.; Rajesh, N. U.; Hoang, T.; Wu, J. L. Y.; Wilhelm, S.; Zilman, A.; Gadde, S.; Sulaiman, A.; Ouyang, B.; Lin, Z.; Wang, L.; Egeblad, M.; Chan, W. C. W. The entry of nanoparticles into solid tumours. *Nature Materials* **2020**, *19*, 566.

54. de Lázaro, I.; Mooney, D. J. A nanoparticle's pathway into tumours. *Nature Materials* **2020**, *19*, 486.

55. May, J.-N.; Moss, J. I.; Mueller, F.; Golombek, S. K.; Biancacci, I.; Rizzo, L.; Elshafei, A. S.; Gremse, F.; Pola, R.; Pechar, M.; Etrych, T.; Becker, S.; Trautwein, C.; Bülow, R. D.; Boor, P.; Knuechel, R.; von Stillfried, S.; Storm, G.; Puri, S.; Barry, S. T.; Schulz, V.; Kiessling, F.; Ashford, M. B.; Lammers, T. Histopathological biomarkers for predicting the tumour accumulation of nanomedicines. *Nature Biomedical Engineering* **2024**.

56. Stuart, M. A. C.; Huck, W. T. S.; Genzer, J.; Müller, M.; Ober, C.; Stamm, M.; Sukhorukov, G. B.; Szleifer, I.; Tsukruk, V. V.; Urban, M.; Winnik, F.; Zauscher, S.; Luzinov, I.; Minko, S. Emerging applications of stimuli-responsive polymer materials. *Nature Materials* **2010**, *9*, 101.

57. Green, J. J.; Elisseeff, J. H. Mimicking biological functionality with polymers for biomedical applications. *Nature* **2016**, *540*, 386.

58. Ahn, B. K.; Lee, D. W.; Israelachvili, J. N.; Waite, J. H. Surface-initiated self-healing of polymers in aqueous media. *Nature Materials* **2014**, *13*, 867.

59. Zhao, Q.; Lee, D. W.; Ahn, B. K.; Seo, S.; Kaufman, Y.; Israelachvili, Jacob N.; Waite, J. H. Underwater contact adhesion and microarchitecture in polyelectrolyte complexes actuated by solvent exchange. *Nature Materials* **2016**, *15*, 407.

60. Maier, G. P.; Rapp, M. V.; Waite, J. H.; Israelachvili, J. N.; Butler, A. Adaptive synergy between catechol and lysine promotes wet adhesion by surface salt displacement. *Science* **2015**, *349*, 628.

61. Ebara, M.; Yamato, M.; Aoyagi, T.; Kikuchi, A.; Sakai, K.; Okano, T. Temperature-Responsive Cell Culture Surfaces Enable "On−Off" Affinity Control between Cell Integrins and RGDS Ligands. *Biomacromolecules* **2004**, *5*, 505.

62. Ionov, L. Polymeric Actuators. *Langmuir* **2015**, *31*, 5015.

63. Martins, P.; Correia, D. M.; Correia, V.; Lanceros-Mendez, S. Polymer-based actuators: back to the future. *Physical Chemistry Chemical Physics* **2020**, *22*, 15163.

64. Maslen, C.; Gholamipour-Shirazi, A.; Butler, M. D.; Kropáček, J.; Řehoř, I.; Montenegro-Johnson, T. A New Class of Single-Material, Non-Reciprocal Microactuators. *Macromolecular Rapid Communications* **2023**, *44*, 2200842.

65. Řehoř, I.; Maslen, C.; Moerman, P. G.; van Ravensteijn, B. G. P.; van Alst, R.; Groenewold, J.; Eral, H. B.; Kegel, W. K. Photoresponsive Hydrogel Microcrawlers Exploit Friction Hysteresis to Crawl by Reciprocal Actuation. *Soft Robotics* **2020**, *8*, 10.

66. Zhou, F.; Shu, W.; Welland, M. E.; Huck, W. T. S. Highly Reversible and Multi-Stage Cantilever Actuation Driven by Polyelectrolyte Brushes. *Journal of the American Chemical Society* **2006**, *128*, 5326.

67. Tokareva, I.; Minko, S.; Fendler, J. H.; Hutter, E. Nanosensors Based on Responsive Polymer Brushes and Gold Nanoparticle Enhanced Transmission Surface Plasmon Resonance Spectroscopy. *Journal of the American Chemical Society* **2004**, *126*, 15950.

68. Itano, K.; Choi, J.; Rubner, M. F. Mechanism of the pH-Induced Discontinuous Swelling/Deswelling Transitions of Poly(allylamine hydrochloride)-Containing Polyelectrolyte Multilayer Films. *Macromolecules* **2005**, *38*, 3450.

69. Kamaly, N.; Yameen, B.; Wu, J.; Farokhzad, O. C. Degradable Controlled-Release Polymers and Polymeric Nanoparticles: Mechanisms of Controlling Drug Release. *Chemical Reviews* **2016**, *116*, 2602.

70. Zhuang, J.; Gordon, M. R.; Ventura, J.; Li, L.; Thayumanavan, S. Multi-stimuli responsive macromolecules and their assemblies. *Chemical Society Reviews* **2013**, *42*, 7421.

71. Klaikherd, A.; Nagamani, C.; Thayumanavan, S. Multi-Stimuli Sensitive Amphiphilic Block Copolymer Assemblies. *Journal of the American Chemical Society* **2009**, *131*, 4830.

72. Roy, D.; Brooks, W. L. A.; Sumerlin, B. S. New directions in thermoresponsive polymers. *Chemical Society Reviews* **2013**, *42*, 7214.

73. Roth, P. J.; Davis, T. P.; Lowe, A. B. Comparison between the LCST and UCST Transitions of Double Thermoresponsive Diblock Copolymers: Insights into the Behavior of POEGMA in Alcohols. *Macromolecules* **2012**, *45*, 3221.

74. Rubinstein, M.; Colby, R. H. *Polymer Physics*; Oxford University Press, 2003.

75. Scarpa, J. S.; Mueller, D. D.; Klotz, I. M. Slow hydrogen-deuterium exchange in a non-.alpha.-helical polyamide. *Journal of the American Chemical Society* **1967**, *89*, 6024.

76. Halperin, A.; Kröger, M.; Winnik, F. M. Poly(N-isopropylacrylamide) Phase Diagrams: Fifty Years of Research. *Angewandte Chemie International Edition* **2015**, *54*, 15342.

77. Kolouchová, K.; Lobaz, V.; Beneš, H.; de la Rosa, V. R.; Babuka, D.; Švec, P.; Černoch, P.; Hrubý, M.; Hoogenboom, R.; Štěpánek, P.; Groborz, O. Thermoresponsive properties of polyacrylamides in physiological solutions. *Polymer Chemistry* **2021**, *12*, 5077.

78. Weaver, J. V. M.; Armes, S. P.; Bütün, V. Synthesis and aqueous solution properties of a well-defined thermo-responsive schizophrenic diblock copolymer. *Chemical Communications* **2002**, 2122.

79. Arotçaréna, M.; Heise, B.; Ishaya, S.; Laschewsky, A. Switching the Inside and the Outside of Aggregates of Water-Soluble Block Copolymers with Double Thermoresponsivity. *Journal of the American Chemical Society* **2002**, *124*, 3787.

80. Gao, S.; Tang, G.; Hua, D.; Xiong, R.; Han, J.; Jiang, S.; Zhang, Q.; Huang, C. Stimuli-responsive bio-based polymeric systems and their applications. *Journal of Materials Chemistry B* **2019**, *7*, 709.

81. Sedláček, O.; Filippov, S. K.; Švec, P.; Hrubý, M. SET-LRP Synthesis of Well-Defined Light-Responsible Block Copolymer Micelles. *Macromolecular Chemistry and Physics* **2019**, *220*, 1900238.

82. Jiang, J.; Tong, X.; Zhao, Y. A New Design for Light-Breakable Polymer Micelles. *Journal of the American Chemical Society* **2005**, *127*, 8290.

83. Babin, J.; Pelletier, M.; Lepage, M.; Allard, J.-F.; Morris, D.; Zhao, Y. A New Two-Photon-Sensitive Block Copolymer Nanocarrier. *Angewandte Chemie International Edition* **2009**, *48*, 3329.

84. Son, S.; Shin, E.; Kim, B.-S. Light-Responsive Micelles of Spiropyran Initiated Hyperbranched Polyglycerol for Smart Drug Delivery. *Biomacromolecules* **2014**, *15*, 628.

85. Buback, J.; Kullmann, M.; Langhojer, F.; Nuernberger, P.; Schmidt, R.; Würthner, F.; Brixner, T. Ultrafast Bidirectional Photoswitching of a Spiropyran. *Journal of the American Chemical Society* **2010**, *132*, 16510.

86. Matsubara, K.; Watanabe, M.; Takeoka, Y. A Thermally Adjustable Multicolor Photochromic Hydrogel. *Angewandte Chemie International Edition* **2007**, *46*, 1688.

87. Kocak, G.; Tuncer, C.; Bütün, V. pH-Responsive polymers. *Polymer Chemistry* **2017**, *8*, 144.

88. Kolouchová, K.; Jirák, D.; Groborz, O.; Sedláček, O.; Ziolkowská, N.; Vít, M.; Šticová, E.; Gálisová, A.; Švec, P.; Trousil, J.; Hájek, M.; Hrubý, M. Implant-forming polymeric 19F MRI-tracer with tunable dissolution. *Journal of Controlled Release* **2020**, *327*, 50.

89. Kawamura, A.; Miyata, T. pH-Responsive Polymer. In *Encyclopedia of Polymeric Nanomaterials*, Kobayashi, S., Müllen, K. Eds.; Springer Berlin Heidelberg, 2021; pp 1.

90. Tao, W.; Wang, J.; Parak, W. J.; Farokhzad, O. C.; Shi, J. Nanobuffering of pH-Responsive Polymers: A Known but Sometimes Overlooked Phenomenon and Its Biological Applications. *ACS Nano* **2019**, *13*, 4876.

91. Anees, P.; Zhao, Y.; Greschner, A. A.; Congdon, T. R.; de Haan, H. W.; Cottenye, N.; Gauthier, M. A. Evidence, Manipulation, and Termination of pH 'Nanobuffering' for Quantitative Homogenous Scavenging of Monoclonal Antibodies. *ACS Nano* **2019**, *13*, 1019.

92. Nikam, A.; Sahoo, P. R.; Musale, S.; Pagar, R. R.; Paiva-Santos, A. C.; Giram, P. S. A Systematic Overview of Eudragit® Based Copolymer for Smart Healthcare. *Pharmaceutics* **2023**, *15*, 587.

93. Huo, M.; Yuan, J.; Tao, L.; Wei, Y. Redox-responsive polymers for drug delivery: from molecular design to applications. *Polymer Chemistry* **2014**, *5*, 1519.

94. Lushchak, V. I. Glutathione Homeostasis and Functions: Potential Targets for Medical Interventions. *Journal of Amino Acids* **2012**, *2012*, 736837.

95. Deponte, M. Glutathione catalysis and the reaction mechanisms of glutathione-dependent enzymes. *Biochimica et Biophysica Acta (BBA) - General Subjects* **2013**, *1830*, 3217.

96. Kuppusamy, P.; Li, H.; Ilangovan, G.; Cardounel, A. J.; Zweier, J. L.; Yamada, K.; Krishna, M. C.; Mitchell, J. B. Noninvasive Imaging of Tumor Redox Status and Its Modification by Tissue Glutathione Levels1. *Cancer Research* **2002**, *62*, 307.

97. Monteiro, P. F.; Travanut, A.; Conte, C.; Alexander, C. Reduction-responsive polymers for drug delivery in cancer therapy—Is there anything new to discover? *WIREs Nanomedicine and Nanobiotechnology* **2021**, *13*, e1678.

98. Cho, H.; Bae, J.; Garripelli, V. K.; Anderson, J. M.; Jun, H.-W.; Jo, S. Redox-sensitive polymeric nanoparticles for drug delivery. *Chemical Communications* **2012**, *48*, 6043.

99. Levine, M. N.; Raines, R. T. Trimethyl lock: a trigger for molecular release in chemistry, biology, and pharmacology. *Chemical Science* **2012**, *3*, 2412.

100. Winterbourn, C. C. Reconciling the chemistry and biology of reactive oxygen species. *Nature Chemical Biology* **2008**, *4*, 278.

101. Chio, I. I. C.; Tuveson, D. A. ROS in Cancer: The Burning Question. *Trends in Molecular Medicine* **2017**, *23*, 411.

102. Radi, R. Oxygen radicals, nitric oxide, and peroxynitrite: Redox pathways in molecular medicine. *Proceedings of the National Academy of Sciences* **2018**, *115*, 5839.

103. Brunelle, J. K.; Bell, E. L.; Quesada, N. M.; Vercauteren, K.; Tiranti, V.; Zeviani, M.; Scarpulla, R. C.; Chandel, N. S. Oxygen sensing requires mitochondrial ROS but not oxidative phosphorylation. *Cell Metabolism* **2005**, *1*, 409.

104. Guzy, R. D.; Hoyos, B.; Robin, E.; Chen, H.; Liu, L.; Mansfield, K. D.; Simon, M. C.; Hammerling, U.; Schumacker, P. T. Mitochondrial complex III is required for hypoxia-induced ROS production and cellular oxygen sensing. *Cell Metabolism* **2005**, *1*, 401.

105. Mansfield, K. D.; Guzy, R. D.; Pan, Y.; Young, R. M.; Cash, T. P.; Schumacker, P. T.; Simon, M. C. Mitochondrial dysfunction resulting from loss of cytochrome c impairs cellular oxygen sensing and hypoxic HIF-α activation. *Cell Metabolism* **2005**, *1*, 393.

106. Ryan, H. E.; Lo, J.; Johnson, R. S. HIF-1α is required for solid tumor formation and embryonic vascularization. *The EMBO Journal* **1998**, *17*, 3005.

107. Akong-Moore, K.; Chow, O. A.; von Köckritz-Blickwede, M.; Nizet, V. Influences of Chloride and Hypochlorite on Neutrophil Extracellular Trap Formation. *PLOS ONE* **2012**, *7*, e42984.

108. Manda-Handzlik, A.; Bystrzycka, W.; Cieloch, A.; Glodkowska-Mrowka, E.; Jankowska-Steifer, E.; Heropolitanska-Pliszka, E.; Skrobot, A.; Muchowicz, A.; Ciepiela, O.; Wachowska, M.; Demkow, U. Nitric oxide and peroxynitrite trigger and enhance release of neutrophil extracellular traps. *Cellular and Molecular Life Sciences* **2020**, *77*, 3059.

109. Švec, P.; Petrov, O. V.; Lang, J.; Štěpnička, P.; Groborz, O.; Dunlop, D.; Blahut, J.; Kolouchová, K.; Loukotová, L.; Sedláček, O.; Heizer, T.; Tošner, Z.; Šlouf, M.; Beneš, H.; Hoogenboom, R.; Hrubý, M. Fluorinated Ferrocene Moieties as a Platform for Redox-Responsive Polymer 19F MRI Theranostics. *Macromolecules* **2022**, *55*, 658.

110. Velluto, D.; Demurtas, D.; Hubbell, J. A. PEG-b-PPS Diblock Copolymer Aggregates for Hydrophobic Drug Solubilization and Release: Cyclosporin A as an Example. *Molecular Pharmaceutics* **2008**, *5*, 632.

111. Ma, N.; Li, Y.; Xu, H.; Wang, Z.; Zhang, X. Dual Redox Responsive Assemblies Formed from Diselenide Block Copolymers. *Journal of the American Chemical Society* **2010**, *132*, 442.

112. Stubelius, A.; Lee, S.; Almutairi, A. The Chemistry of Boronic Acids in Nanomaterials for Drug Delivery. *Accounts of Chemical Research* **2019**, *52*, 3108.

113. Jäger, E.; Humajová, J.; Dölen, Y.; Kučka, J.; Jäger, A.; Konefał, R.; Pankrác, J.; Pavlova, E.; Heizer, T.; Šefc, L.; Hrubý, M.; Figdor, C. G.; Verdoes, M. Enhanced Antitumor Efficacy through an "AND gate" Reactive Oxygen-Species-Dependent pH-Responsive Nanomedicine Approach. *Advanced Healthcare Materials* **2021**, *10*, 2100304.

114. Kim, S.; Seong, K.; Kim, O.; Kim, S.; Seo, H.; Lee, M.; Khang, G.; Lee, D. Polyoxalate Nanoparticles as a Biodegradable and Biocompatible Drug Delivery Vehicle. *Biomacromolecules* **2010**, *11*, 555.

115. Höcherl, A.; Jäger, E.; Jäger, A.; Hrubý, M.; Konefał, R.; Janoušková, O.; Spěváček, J.; Jiang, Y.; Schmidt, P. W.; Lodge, T. P.; Štěpánek, P. One-pot synthesis of reactive oxygen species (ROS)-self-immolative polyoxalate prodrug nanoparticles for hormone dependent cancer therapy with minimized side effects. *Polymer Chemistry* **2017**, *8*, 1999.

116. Alkan, A.; Wurm, F. R. Water-Soluble Metallocene-Containing Polymers. *Macromolecular Rapid Communications* **2016**, *37*, 1482.

117. Kolouchová, K.; Groborz, O.; Černochová, Z.; Škárková, A.; Brábek, J.; Rosel, D.; Švec, P.; Starčuk, Z.; Šlouf, M.; Hrubý, M. Thermo-and ROS-Responsive Self-Assembled Polymer Nanoparticle Tracers for 19F MRI Theranostics. *Biomacromolecules* **2021**, *22*, 2325.

118. Borchers, P. S.; Dirauf, M.; Strumpf, M.; Görls, H.; Weber, C.; Hager, M. D.; Schubert, U. S. Ferrocene containing redox-responsive poly(2-oxazoline)s. *Chemical Communications* **2021**, *57*, 1308.

119. Moreno, S.; Hübner, H.; Effenberg, C.; Boye, S.; Ramuglia, A.; Schmitt, D.; Voit, B.; Weidinger, I. M.; Gallei, M.; Appelhans, D. Redox- and pH-Responsive Polymersomes with Ferrocene Moieties Exhibiting Peroxidase-like, Chemoenzymatic Activity and H2O2-Responsive Release Behavior. *Biomacromolecules* **2022**, *23*, 4655.

120. Clar, E. Nomenclature of Polycyclic Hydrocarbons. In *Polycyclic Hydrocarbons: Volume 1*, Springer Berlin Heidelberg, 1964; pp 3.

121. Poater, J.; Duran, M.; Solà, M. Aromaticity Determines the Relative Stability of Kinked vs. Straight Topologies in Polycyclic Aromatic Hydrocarbons. *Frontiers in Chemistry* **2018**, *6*.

122. Tönshoff, C.; Bettinger, H. F. Pushing the Limits of Acene Chemistry: The Recent Surge of Large Acenes. *Chemistry – A European Journal* **2021**, *27*, 3193.

123. Hardouin, C.; Kelso, M. J.; Romero, F. A.; Rayl, T. J.; Leung, D.; Hwang, I.; Cravatt, B. F.; Boger, D. L. Structure−Activity Relationships of α-Ketooxazole Inhibitors of Fatty Acid Amide Hydrolase. *Journal of Medicinal Chemistry* **2007**, *50*, 3359.

124. Masamichi, Y.; Isao, I.; Haruo, K. Photooxidation of the Evaporated Films of Polycyclic Aromatic Hydrocarbons Studied by X-Ray Photoelectron Spectroscopy. *Bulletin of the Chemical Society of Japan* **1988**, *61*, 1057.

125. Maliakal, A.; Raghavachari, K.; Katz, H.; Chandross, E.; Siegrist, T. Photochemical Stability of Pentacene and a Substituted Pentacene in Solution and in Thin Films. *Chemistry of Materials* **2004**, *16*, 4980.

126. Richards, G. J.; Hill, J. P.; Mori, T.; Ariga, K. Putting the 'N' in ACENE: Pyrazinacenes and their structural relatives. *Organic & Biomolecular Chemistry* **2011**, *9*, 5005.

127. Brega, V.; Yan, Y.; Thomas, S. W. Acenes beyond organic electronics: sensing of singlet oxygen and stimuli-responsive materials. *Organic & Biomolecular Chemistry* **2020**, *18*, 9191.

128. Zhou, J.; Liu, Q.; Feng, W.; Sun, Y.; Li, F. Upconversion Luminescent Materials: Advances and Applications. *Chemical Reviews* **2015**, *115*, 395.

129. Parker, C. A.; Hatchard, C. G.; Bowen, E. J. Delayed fluorescence from solutions of anthracene and phenanthrene. *Proceedings of the Royal Society of London. Series A. Mathematical and Physical Sciences* **1962**, *269*, 574.

130. Imperiale, C. J.; Green, P. B.; Miller, E. G.; Damrauer, N. H.; Wilson, M. W. B. Triplet-Fusion Upconversion Using a Rigid Tetracene Homodimer. *The Journal of Physical Chemistry Letters* **2019**, *10*, 7463.

131. Chen, H.-C.; Hung, C.-Y.; Wang, K.-H.; Chen, H.-L.; Fann, W. S.; Chien, F.-C.; Chen, P.; Chow, T. J.; Hsu, C.-P.; Sun, S.-S. White-light emission from an upconverted emission with an organic triplet sensitizer. *Chemical Communications* **2009**, *27*, 4064.

132. Chen, G.; Qiu, H.; Prasad, P. N.; Chen, X. Upconversion Nanoparticles: Design, Nanochemistry, and Applications in Theranostics. *Chemical Reviews* **2014**, *114*, 5161.

133. Weinstain, R.; Slanina, T.; Kand, D.; Klán, P. Visible-to-NIR-Light Activated Release: From Small Molecules to Nanomaterials. *Chemical Reviews* **2020**, *120*, 13135.

134. Yan, B.; Boyer, J.-C.; Branda, N. R.; Zhao, Y. Near-Infrared Light-Triggered Dissociation of Block Copolymer Micelles Using Upconverting Nanoparticles. *Journal of the American Chemical Society* **2011**, *133*, 19714.

135. Bunz, U. H. F. The Larger Linear N-Heteroacenes. *Accounts of Chemical Research* **2015**, *48*, 1676.

136. Richards, G. J.; Hill, J. P.; Subbaiyan, N. K.; D'Souza, F.; Karr, P. A.; Elsegood, M. R. J.; Teat, S. J.; Mori, T.; Ariga, K. Pyrazinacenes: Aza Analogues of Acenes. *The Journal of Organic Chemistry* **2009**, *74*, 8914.

137. Švec, P.; Webre, W. A.; Richards, G. J.; Labuta, J.; Wakayama, Y.; Miklík, D.; Karr, P. A.; Mori, T.; Ariga, K.; D'Souza, F.; Hill, J. P. Phenanthroline-Fused Pyrazinacenes: One-Pot Synthesis, Tautomerization and a RuII(2,2′-bpy)2 Derivative. *European Journal of Inorganic Chemistry* **2018**, *2018*, 2541.

138. Winkler, M.; Houk, K. N. Nitrogen-Rich Oligoacenes: Candidates for n-Channel Organic Semiconductors. *Journal of the American Chemical Society* **2007**, *129*, 1805.

139. Richards, G. J.; Cador, A.; Yamada, S.; Middleton, A.; Webre, W. A.; Labuta, J.; Karr, P. A.; Ariga, K.; D'Souza, F.; Kahlal, S.; Halet, J.-F.; Hill, J. P. Amphiprotism-Coupled Near-Infrared Emission in Extended Pyrazinacenes Containing Seven Linearly Fused Pyrazine Units. *Journal of the American Chemical Society* **2019**, *141*, 19570.

140. Šuteková, M.; Barlog, M.; Baranyaiová, T. Š.; Klement, R.; Richards, G. J.; Hill, J. P.; Labuta, J.; Bujdák, J. Pyrazinacene luminescence enhancement by heat-activated surface adsorption and de-aggregation in a saponite colloidal system. *Applied Clay Science* **2022**, *218*, 106413.

141. Sutton, M. *The birth of the polymer age*. 2020. https://www.chemistryworld.com/features/the-birth-of-the-polymer-age/4011418.article (accessed 2023 8 September 2023).

142. Staudinger, H. Über Polymerisation. *Berichte der deutschen chemischen Gesellschaft (A and B Series)* **1920**, *53*, 1073.

143. Frey, H.; Johann, T. Celebrating 100 years of "polymer science": Hermann Staudinger's 1920 manifesto. *Polymer Chemistry* **2020**, *11*, 8.

144. Staudinger, H.; Fritschi, J. Über Isopren und Kautschuk. 5. Mitteilung. Über die Hydrierung des Kautschuks und über seine Konstitution. *Helvetica Chimica Acta* **1922**, *5*, 785.

145. Webster, O. W. Living Polymerization Methods. *Science* **1991**, *251*, 887.

146. Szwarc, M. 'Living' Polymers. *Nature* **1956**, *178*, 1168.

147. Szwarc, M.; Levy, M.; Milkovich, R. Polymerization Initiated by Electron Transfer to Monomer. A New Method of Formation of Block Polymers. *Journal of the American Chemical Society* **1956**, *78*, 2656.

148. Grubbs, R. B.; Grubbs, R. H. 50th Anniversary Perspective: Living Polymerization—Emphasizing the Molecule in Macromolecules. *Macromolecules* **2017**, *50*, 6979.

149. Matyjaszewski, K.; Xia, J. Atom Transfer Radical Polymerization. *Chemical Reviews* **2001**, *101*, 2921.

150. Stenzel, M. H.; Barner-Kowollik, C. The living dead – common misconceptions about reversible deactivation radical polymerization. *Materials Horizons* **2016**, *3*, 471.

151. Jenkins, A. D.; Jones, R. G.; Moad, G. Terminology for reversible-deactivation radical polymerization previously called "controlled" radical or "living" radical polymerization (IUPAC Recommendations 2010). *Pure and Applied Chemistry* **2009**, *82*, 483.

152. Claverie, J. P.; Schaper, F. Ziegler-Natta catalysis: 50 years after the Nobel Prize. *MRS Bulletin* **2013**, *38*, 213.

153. Coates, G. W.; Hustad, P. D.; Reinartz, S. Catalysts for the Living Insertion Polymerization of Alkenes: Access to New Polyolefin Architectures Using Ziegler–Natta Chemistry. *Angewandte Chemie International Edition* **2002**, *41*, 2236.
154. Meyers, A. I.; Temple, D. L.; Nolen, R. L.; Mihelich, E. D. Oxazolines. IX. Synthesis of homologated acetic acids and esters. *The Journal of Organic Chemistry* **1974**, *39*, 2778.
155. Gant, T. G.; Meyers, A. I. The chemistry of 2-oxazolines (1985–present). *Tetrahedron* **1994**, *50*, 2297.
156. Penczek, S.; Cypryk, M.; Duda, A.; Kubisa, P.; Słomkowski, S. Living ring-opening polymerizations of heterocyclic monomers. *Progress in Polymer Science* **2007**, *32*, 247.
157. Tomalia, D. A.; Sheetz, D. P. Homopolymerization of 2-alkyl- and 2-aryl-2-oxazolines. *Journal of Polymer Science Part A-1: Polymer Chemistry* **1966**, *4*, 2253.
158. Seeliger, W.; Aufderhaar, E.; Diepers, W.; Feinauer, R.; Nehring, R.; Thier, W.; Hellmann, H. Recent Syntheses and Reactions of Cyclic Imidic Esters. *Angewandte Chemie International Edition in English* **1966**, *5*, 875.
159. Konradi, R.; Pidhatika, B.; Mühlebach, A.; Textor, M. Poly-2-methyl-2-oxazoline: A Peptide-like Polymer for Protein-Repellent Surfaces. *Langmuir* **2008**, *24*, 613.
160. Verbraeken, B.; Monnery, B. D.; Lava, K.; Hoogenboom, R. The chemistry of poly(2-oxazoline)s. *European Polymer Journal* **2017**, *88*, 451.
161. Hrkach, J. S.; Matyjaszewski, K. Reaction of 2-methyl-2-oxazoline with trimethylsilyl initiators: an unusual mode of ring opening. *Macromolecules* **1992**, *25*, 2070.
162. Glassner, M.; Vergaelen, M.; Hoogenboom, R. Poly(2-oxazoline)s: A comprehensive overview of polymer structures and their physical properties. *Polymer International* **2018**, *67*, 32.
163. Monnery, B. D.; Jerca, V. V.; Sedláček, O.; Verbraeken, B.; Cavill, R.; Hoogenboom, R. Defined High Molar Mass Poly(2-Oxazoline)s. *Angewandte Chemie International Edition* **2018**, *57*, 15400.
164. Hadjichristidis, N.; Pitsikalis, M.; Pispas, S.; Iatrou, H. Polymers with Complex Architecture by Living Anionic Polymerization. *Chemical Reviews* **2001**, *101*, 3747.
165. Anastasaki, A.; Nikolaou, V.; Nurumbetov, G.; Wilson, P.; Kempe, K.; Quinn, J. F.; Davis, T. P.; Whittaker, M. R.; Haddleton, D. M. Cu(0)-Mediated Living Radical Polymerization: A Versatile Tool for Materials Synthesis. *Chemical Reviews* **2016**, *116*, 835.
166. Braunecker, W. A.; Matyjaszewski, K. Controlled/living radical polymerization: Features, developments, and perspectives. *Progress in Polymer Science* **2007**, *32*, 93.
167. Grubbs, R. B. Nitroxide-Mediated Radical Polymerization: Limitations and Versatility. *Polymer Reviews* **2011**, *51*, 104.
168. Truong, N. P.; Jones, G. R.; Bradford, K. G. E.; Konkolewicz, D.; Anastasaki, A. A comparison of RAFT and ATRP methods for controlled radical polymerization. *Nature Reviews Chemistry* **2021**, *5*, 859.
169. Zard, S. Z. Discovery of the RAFT/MADIX Process: Mechanistic Insights and Polymer Chemistry Implications. *Macromolecules* **2020**, *53*, 8144.
170. Zard, S. Z. The Genesis of the Reversible Radical AdditionFragmentationTransfer of Thiocarbonylthio Derivatives from the BartonMcCombie Deoxygenation: A Brief Account and Some Mechanistic Observations. *Australian Journal of Chemistry* **2006**, *59*, 663.
171. Barton, D. H. R.; McCombie, S. W. A new method for the deoxygenation of secondary alcohols. *Journal of the Chemical Society, Perkin Transactions 1* **1975**, 1574.

172. Barker, P. J.; Backwith, A. L. J. E.S.R. Identification of Alkoxythiocarbonyl Radicals as Possible Intermediates in Barton Deoxygenation of Alcohols. *Journal of the Chemical Society, Chemical Communications* **1984**, 683.

173. Barton, D. H. R.; Crich, D.; Löbberding, A.; Zard, S. Z. On the mechanism of the deoxygenation of secondary alcohols by the reduction of their methyl xanthates by tin hydrides. *Tetrahedron* **1986**, *42*, 2329.

174. Scaiano, J. C.; Ingold, K. U. Kinetic applications of electron paramagnetic resonance spectroscopy. 25. Radicals formed by spin trapping with di-tert-butyl thioketone. *Journal of the American Chemical Society* **1976**, *98*, 4727.

175. Perrier, S. 50th Anniversary Perspective: RAFT Polymerization—A User Guide. *Macromolecules* **2017**, *50*, 7433.

176. Perrier, S.; Takolpuckdee, P. Macromolecular design via reversible addition–fragmentation chain transfer (RAFT)/xanthates (MADIX) polymerization. *Journal of Polymer Science Part A: Polymer Chemistry* **2005**, *43*, 5347.

177. Dommanget, C.; D'Agosto, F.; Monteil, V. Polymerization of Ethylene through Reversible Addition–Fragmentation Chain Transfer (RAFT). *Angewandte Chemie International Edition* **2014**, *53*, 6683.

178. Keddie, D. J. A guide to the synthesis of block copolymers using reversible-addition fragmentation chain transfer (RAFT) polymerization. *Chemical Society Reviews* **2014**, *43*, 496.

179. Willcock, H.; O'Reilly, R. K. End group removal and modification of RAFT polymers. *Polymer Chemistry* **2010**, *1*, 149.

180. Curran, D. P. The Design and Application of Free Radical Chain Reactions in Organic Synthesis. Part 2. *Synthesis* **1988**, *1988*, 489.

181. Matyjaszewski, K.; Spanswick, J. *Atom Transfer Radical Polymerization (ATRP)*. Elsevier 2016. DOI:10.1016/B978-0-12-803581-8.01354-0

182. Wang, J.-S.; Matyjaszewski, K. Controlled/"living" radical polymerization. atom transfer radical polymerization in the presence of transition-metal complexes. *Journal of the American Chemical Society* **1995**, *117*, 5614.

183. Ribelli, T. G.; Lorandi, F.; Fantin, M.; Matyjaszewski, K. Atom Transfer Radical Polymerization: Billion Times More Active Catalysts and New Initiation Systems. *Macromolecular Rapid Communications* **2019**, *40*, 1800616.

184. Kato, M.; Kamigaito, M.; Sawamoto, M.; Higashimura, T. Polymerization of Methyl Methacrylate with the Carbon Tetrachloride/Dichlorotris- (triphenylphosphine)ruthenium(II) /Methylaluminum Bis(2,6-di-tert-butylphenoxide) Initiating System: Possibility of Living Radical Polymerization. *Macromolecules* **1995**, *28*, 1721.

185. Kamigaito, M.; Ando, T.; Sawamoto, M. Metal-Catalyzed Living Radical Polymerization. *Chemical Reviews* **2001**, *101*, 3689.

186. O'Reilly, R. K.; Gibson, V. C.; White, A. J. P.; Williams, D. J. Design of Highly Active Iron-Based Catalysts for Atom Transfer Radical Polymerization: Tridentate Salicylaldiminato Ligands Affording near Ideal Nernstian Behavior. *Journal of the American Chemical Society* **2003**, *125*, 8450.

187. Uegaki, H.; Kotani, Y.; Kamigaito, M.; Sawamoto, M. NiBr2(Pn-Bu3)2-Mediated Living Radical Polymerization of Methacrylates and Acrylates and Their Block or Random Copolymerizations. *Macromolecules* **1998**, *31*, 6756.

188. Percec, V.; Barboiu, B.; Neumann, A.; Ronda, J. C.; Zhao, M. Metal-Catalyzed “Living” Radical Polymerization of Styrene Initiated with Arenesulfonyl Chlorides. From Heterogeneous to Homogeneous Catalysis. *Macromolecules* **1996**, *29*, 3665.

189. Lecomte, P.; Drapier, I.; Dubois, P.; Teyssié, P.; Jérôme, R. Controlled Radical Polymerization of Methyl Methacrylate in the Presence of Palladium Acetate, Triphenylphosphine, and Carbon Tetrachloride. *Macromolecules* **1997**, *30*, 7631.

190. Kotani, Y.; Kamigaito, M.; Sawamoto, M. Re(V)-Mediated Living Radical Polymerization of Styrene: ReO2I(PPh3)2/R−I Initiating Systems. *Macromolecules* **1999**, *32*, 2420.

191. Brandts, J. A. M.; van de Geijn, P.; van Faassen, E. E.; Boersma, J.; van Koten, G. Controlled radical polymerization of styrene in the presence of lithium molybdate(V) complexes and benzylic halides. *Journal of Organometallic Chemistry* **1999**, *584*, 246.

192. Lin, C. Y.; Coote, M. L.; Gennaro, A.; Matyjaszewski, K. Ab Initio Evaluation of the Thermodynamic and Electrochemical Properties of Alkyl Halides and Radicals and Their Mechanistic Implications for Atom Transfer Radical Polymerization. *Journal of the American Chemical Society* **2008**, *130*, 12762.

193. Nicolaÿ, R.; Kwak, Y.; Matyjaszewski, K. Synthesis of poly(vinyl acetate) block copolymers by successive RAFT and ATRP with a bromoxanthate iniferter. *Chemical Communications* **2008**, 5336.

194. Tong, Y.-Y.; Dong, Y.-Q.; Du, F.-S.; Li, Z.-C. Synthesis of Well-Defined Poly(vinyl acetate)-b-Polystyrene by Combination of ATRP and RAFT Polymerization. *Macromolecules* **2008**, *41*, 7339.

195. Percec, V.; Guliashvili, T.; Ladislaw, J. S.; Wistrand, A.; Stjerndahl, A.; Sienkowska, M. J.; Monteiro, M. J.; Sahoo, S. Ultrafast Synthesis of Ultrahigh Molar Mass Polymers by Metal-Catalyzed Living Radical Polymerization of Acrylates, Methacrylates, and Vinyl Chloride Mediated by SET at 25 °C. *Journal of the American Chemical Society* **2006**, *128*, 14156.

196. Konkolewicz, D.; Wang, Y.; Krys, P.; Zhong, M.; Isse, A. A.; Gennaro, A.; Matyjaszewski, K. SARA ATRP or SET-LRP. End of controversy? *Polymer Chemistry* **2014**, *5*, 4396.

197. Matyjaszewski, K.; Coca, S.; Gaynor, S. G.; Wei, M.; Woodworth, B. E. Zerovalent Metals in Controlled/“Living” Radical Polymerization. *Macromolecules* **1997**, *30*, 7348.

198. Queffelec, J.; Gaynor, S. G.; Matyjaszewski, K. Optimization of Atom Transfer Radical Polymerization Using Cu(I)/Tris(2-(dimethylamino)ethyl)amine as a Catalyst. *Macromolecules* **2000**, *33*, 8629.

199. Zhang, Y.; Wang, Y.; Matyjaszewski, K. ATRP of Methyl Acrylate with Metallic Zinc, Magnesium, and Iron as Reducing Agents and Supplemental Activators. *Macromolecules* **2011**, *44*, 683.

200. Konkolewicz, D.; Wang, Y.; Zhong, M.; Krys, P.; Isse, A. A.; Gennaro, A.; Matyjaszewski, K. Reversible-Deactivation Radical Polymerization in the Presence of Metallic Copper. A Critical Assessment of the SARA ATRP and SET-LRP Mechanisms. *Macromolecules* **2013**, *46*, 8749.

201. Gao, Y.; Zhao, T.; Wang, W. Is it ATRP or SET-LRP? part I: Cu0&CuII/PMDETA – mediated reversible – deactivation radical polymerization. *RSC Advances* **2014**, *4*, 61687.

202. Lyu, J.; Miao, Y.; Li, Z.; Li, Y.; Gao, Y.; Johnson, M.; Tai, H.; Wang, W. Where is the induction from? Effect of disproportionation and comproportionation in Cu(0)-mediated reversible deactivation radical polymerization. *Polymer* **2023**, *280*, 126055.

203. Bolger, J.; Gourdon, A.; Ishow, E.; Launay, J.-P. Mononuclear and Binuclear Tetrapyrido[3,2-a:2‘,3‘-c:3‘‘,2‘‘-h:2‘‘‘,3‘‘‘-j]phenazine (tpphz) Ruthenium and Osmium Complexes. *Inorganic Chemistry* **1996**, *35*, 2937.

204. Scipioni, R.; Boero, M.; Richards, G. J.; Hill, J. P.; Ohno, T.; Mori, T.; Ariga, K. Tautomerism in Reduced Pyrazinacenes. *Journal of Chemical Theory and Computation* **2010**, *6*, 517.

205. Scipioni, R.; Hill, J. P.; Richards, G. J.; Boero, M.; Mori, T.; Ariga, K.; Ohno, T. Tautomers of extended reduced pyrazinacenes: a density-functional-theory based study. *Physical Chemistry Chemical Physics* **2011**, *13*, 2145.

206. Richards, G. J.; Hill, J. P.; Labuta, J.; Wakayama, Y.; Akada, M.; Ariga, K. Self-assembled pyrazinacene nanotubes. *Physical Chemistry Chemical Physics* **2011**, *13*, 4868.

207. Liu, Y.; Hammitt, R.; Lutterman, D. A.; Joyce, L. E.; Thummel, R. P.; Turro, C. Ru(II) Complexes of New Tridentate Ligands: Unexpected High Yield of Sensitized 1O2. *Inorganic Chemistry* **2009**, *48*, 375.

208. Liu, H.-K.; Sadler, P. J. Metal Complexes as DNA Intercalators. *Accounts of Chemical Research* **2011**, *44*, 349.

209. Troian-Gautier, L.; Moucheron, C. RutheniumII Complexes bearing Fused Polycyclic Ligands: From Fundamental Aspects to Potential Applications. *Molecules* **2014**, *19*, 5028.

210. Sun, Y.; Collins, S. N.; Joyce, L. E.; Turro, C. Unusual Photophysical Properties of a Ruthenium(II) Complex Related to [Ru(bpy)2(dppz)]2+. *Inorganic Chemistry* **2010**, *49*, 4257.

211. Juris, A.; Balzani, V.; Barigelletti, F.; Campagna, S.; Belser, P.; von Zelewsky, A. Ru(II) polypyridine complexes: photophysics, photochemistry, eletrochemistry, and chemiluminescence. *Coordination Chemistry Reviews* **1988**, *84*, 85.

212. Yellappa, S.; Webre, W. A.; Gobeze, H. B.; Middleton, A.; KC, C. B.; D'Souza, F. Phenothiazine-Sensitized Solar Cells: Effect of Number of Cyanocinnamic Acid Anchoring Groups on Dye-Sensitized Solar Cell Performance. *ChemPlusChem* **2017**, *82*, 896.

213. Bräutigam, M.; Kübel, J.; Schulz, M.; Vos, J. G.; Dietzek, B. Hole injection dynamics from two structurally related Ru–bipyridine complexes into NiOx is determined by the substitution pattern of the ligands. *Physical Chemistry Chemical Physics* **2015**, *17*, 7823.

214. Hu, Y.; Yellappa, S.; Thomas, M. B.; Jinadasa, R. G. W.; Matus, A.; Shulman, M.; D'Souza, F.; Wang, H. β-Functionalized Push–Pull opp-Dibenzoporphyrins as Sensitizers for Dye-Sensitized Solar Cells. *Chemistry – An Asian Journal* **2017**, *12*, 2749.

215. Stumper, A.; Pilz, T. D.; Schaub, M.; Görls, H.; Sorsche, D.; Peuntinger, K.; Guldi, D.; Rau, S. Efficient Access to 5-Bromo- and 5,6-Dibromophenanthroline Ligands. *European Journal of Inorganic Chemistry* **2017**, *2017*, 3799.

216. Spiccia, L.; Deacon, G. B.; Kepert, C. M. Synthetic routes to homoleptic and heteroleptic ruthenium(II) complexes incorporating bidentate imine ligands. *Coordination Chemistry Reviews* **2004**, *248*, 1329.

217. Aslan, J. M.; Boston, D. J.; MacDonnell, F. M. Photodriven Multi-electron Storage in Disubstituted RuII Dppz Analogues. *Chemistry – A European Journal* **2015**, *21*, 17314.

218. Sorsche, D.; Schaub, M.; Heinemann, F. W.; Habermehl, J.; Kuhri, S.; Guldi, D.; Guthmuller, J.; Rau, S. π-Stacking attraction vs. electrostatic repulsion: competing supramolecular interactions in a tpphz-bridged Ru(II)/Au(III) complex. *Dalton Transactions* **2016**, *45*, 12846.

219. Majewski, M. B.; de Tacconi, N. R.; MacDonnell, F. M.; Wolf, M. O. Long-Lived, Directional Photoinduced Charge Separation in RuII Complexes Bearing Laminate Polypyridyl Ligands. *Chemistry – A European Journal* **2013**, *19*, 8331.

220. Schindler, J.; Zhang, Y.; Traber, P.; Lefebvre, J.-F.; Kupfer, S.; Demeunynck, M.; Gräfe, S.; Chavarot-Kerlidou, M.; Dietzek, B. A $\pi\pi^*$ State Enables Photoaccumulation of Charges on a π-Extended Dipyridophenazine Ligand in a Ru(II) Polypyridine Complex. *The Journal of Physical Chemistry C* **2018**, *122*, 83.

221. Pashaei, B.; Shahroosvand, H.; Graetzel, M.; Nazeeruddin, M. K. Influence of Ancillary Ligands in Dye-Sensitized Solar Cells. *Chemical Reviews* **2016**, *116*, 9485.

222. Happ, B.; Winter, A.; Hager, M. D.; Schubert, U. S. Photogenerated avenues in macromolecules containing Re(i), Ru(ii), Os(ii), and Ir(iii) metal complexes of pyridine-based ligands. *Chemical Society Reviews* **2012**, *41*, 2222.

223. Tschierlei, S.; Dietzek, B.; Karnahl, M.; Rau, S.; MacDonnell, F. M.; Schmitt, M.; Popp, J. Resonance Raman studies of photochemical molecular devices for multielectron storage. *Journal of Raman Spectroscopy* **2008**, *39*, 557.

224. Chiorboli, C.; Rodgers, M. A. J.; Scandola, F. Ultrafast Processes in Bimetallic Dyads with Extended Aromatic Bridges. Energy and Electron Transfer Pathways in Tetrapyridophenazine-Bridged Complexes. *Journal of the American Chemical Society* **2003**, *125*, 483.

225. Kuhnt, C.; Karnahl, M.; Rau, S.; Schmitt, M.; Dietzek, B.; Popp, J. The impact of bromine substitution on the photophysical properties of a homodinuclear Ru–tpphz–Ru complex. *Chemical Physics Letters* **2011**, *516*, 45.

226. Singh, S.; de Tacconi, N. R.; Diaz, N. R. G.; Lezna, R. O.; Muñoz Zuñiga, J.; Abayan, K.; MacDonnell, F. M. Photochemical Two-Electron Reduction of a Dinuclear Ruthenium Complex Containing a Bent Tetraazatetrapyridopentacene Bridging Ligand: Pushing Up the LUMO for Storing More Energy. *Inorganic Chemistry* **2011**, *50*, 9318.

227. Jiang, J.; Tong, X.; Morris, D.; Zhao, Y. Toward Photocontrolled Release Using Light-Dissociable Block Copolymer Micelles. *Macromolecules* **2006**, *39*, 4633.

228. Huo, H.; Ma, X.; Dong, Y.; Qu, F. Light/temperature dual-responsive ABC miktoarm star terpolymer micelles for controlled release. *European Polymer Journal* **2017**, *87*, 331.

229. Soliman, S. M. A.; Nouvel, C.; Babin, J.; Six, J.-L. o-nitrobenzyl acrylate is polymerizable by single electron transfer-living radical polymerization. *Journal of Polymer Science Part A: Polymer Chemistry* **2014**, *52*, 2192.

230. Nguyen, N. H.; Percec, V. Dramatic acceleration of SET-LRP of methyl acrylate during catalysis with activated Cu(0) wire. *Journal of Polymer Science Part A: Polymer Chemistry* **2010**, *48*, 5109.

231. Blahut, J.; Benda, L.; Kotek, J.; Pintacuda, G.; Hermann, P. Paramagnetic Cobalt(II) Complexes with Cyclam Derivatives: Toward 19F MRI Contrast Agents. *Inorganic Chemistry* **2020**, *59*, 10071.

232. Yu, X.; Tanaka, A.; Tanaka, K.; Tanaka, T. Phase transition of a poly(acrylic acid) gel induced by polymer complexation. *The Journal of Chemical Physics* **1992**, *97*, 7805.

233. Guillier, F.; Orain, D.; Bradley, M. Linkers and Cleavage Strategies in Solid-Phase Organic Synthesis and Combinatorial Chemistry. *Chemical Reviews* **2000**, *100*, 2091.

234. Sedláček, O.; Jirák, D.; Gálisová, A.; Jäger, E.; Laaser, J. E.; Lodge, T. P.; Štěpánek, P.; Hrubý, M. 19F Magnetic Resonance Imaging of Injectable Polymeric Implants with Multiresponsive Behavior. *Chemistry of Materials* **2018**, *30*, 4892.

235. Bak, J. M.; Kim, K.-B.; Lee, J.-E.; Park, Y.; Yoon, S. S.; Jeong, H. M.; Lee, H.-i. Thermoresponsive fluorinated polyacrylamides with low cytotoxicity. *Polymer Chemistry* **2013**, *4*, 2219.

236. Du, B.; Jiang, X.; Das, A.; Zhou, Q.; Yu, M.; Jin, R.; Zheng, J. Glomerular barrier behaves as an atomically precise bandpass filter in a sub-nanometre regime. *Nature Nanotechnology* **2017**, *12*, 1096.

237. Bertrand, N.; Fleischer, J. G.; Wasan, K. M.; Leroux, J.-C. Pharmacokinetics and biodistribution of N-isopropylacrylamide copolymers for the design of pH-sensitive liposomes. *Biomaterials* **2009**, *30*, 2598.

238. Bogomolova, A.; Kaberov, L.; Sedláček, O.; Filippov, S. K.; Štěpánek, P.; Král, V.; Wang, X. Y.; Liu, S. L.; Ye, X. D.; Hrubý, M. Double stimuli-responsive polymer systems: How to use crosstalk between pH- and thermosensitivity for drug depots. *European Polymer Journal* **2016**, *84*, 54.

239. Myles, B. J.; Jarrett, L. A.; Broom, S. L.; Speaker, H. A.; Sabol, K. E. The effects of methamphetamine on core body temperature in the rat—PART 1: chronic treatment and ambient temperature. *Psychopharmacology* **2008**, *198*, 301.

240. Hrubý, M.; Kučka, J.; Mackova, H.; Koňák, C.; Vetrík, M.; Kozempel, J.; Lebeda, O. New binary thermoresponsive polymeric system for local chemoradiotherapy. *Journal of Applied Polymer Science* **2009**, *111*, 2220.

241. Gil, E. S.; Hudson, S. M. Stimuli-reponsive polymers and their bioconjugates. *Progress in Polymer Science* **2004**, *29*, 1173.

242. Lubach, J.; Drenth, W. Enolization and oxidation: II. Oxidation of ferrocene by molecular oxygen and hydrogen peroxide in acidic media. *Recueil des Travaux Chimiques des Pays-Bas* **1973**, *92*, 586.

243. Epton, R.; Hobson, M. E.; Marr, G. Oxidation of ferrocene and some substituted ferrocenes in the presence of horseradish peroxidase. *Journal of Organometallic Chemistry* **1978**, *149*, 231.

244. Traverso, O.; Scandola, F. Photooxidation of ferrocene in halocarbon solvents. *Inorganica Chimica Acta* **1970**, *4*, 493.

245. Bao, D.; Millare, B.; Xia, W.; Steyer, B. G.; Gerasimenko, A. A.; Ferreira, A.; Contreras, A.; Vullev, V. I. Electrochemical Oxidation of Ferrocene: A Strong Dependence on the Concentration of the Supporting Electrolyte for Nonpolar Solvents. *The Journal of Physical Chemistry A* **2009**, *113*, 1259.

246. Ganta, S.; Devalapally, H.; Shahiwala, A.; Amiji, M. A review of stimuli-responsive nanocarriers for drug and gene delivery. *Journal of Controlled Release* **2008**, *126*, 187.

247. Chatterjee, S. Chapter Two - Oxidative Stress, Inflammation, and Disease. In *Oxidative Stress and Biomaterials*, Dziubla, T., Butterfield, D. A. Eds.; Academic Press, 2016; pp 35.

248. Jirák, D.; Gálisová, A.; Kolouchová, K.; Babuka, D.; Hrubý, M. Fluorine polymer probes for magnetic resonance imaging: quo vadis? *Magnetic Resonance Materials in Physics, Biology and Medicine* **2019**, *32*, 173.

249. Babuka, D.; Kolouchová, K.; Groborz, O.; Tošner, Z.; Zhigunov, A.; Štěpánek, P.; Hrubý, M. Internal Structure of Thermoresponsive Physically Crosslinked Nanogel of Poly[N-(2-hydroxypropyl)methacrylamide]-Block-Poly[N-(2,2-difluoroethyl)acrylamide], Prominent 19F MRI Tracer. *Nanomaterials* **2020**, *10*, 2231.

250. Jóhannesson, G.; Stefánsson, E.; Loftsson, T. Microspheres and Nanotechnology for Drug Delivery. In *Retinal Pharmacotherapeutics*, Nguyen, Q. D., Do, D. V., Farah, M. E., Mieler, W. F., Rodrigues, E. B. Eds.; Vol. 55; S.Karger AG, 2015; p 0.

251. Kranzler, H. R.; Wesson, D. R.; Billot, L.; Group, D. S. N. D. S. Naltrexone Depot for Treatment of Alcohol Dependence: A Multicenter, Randomized, Placebo-Controlled Clinical Trial. *Alcoholism: Clinical and Experimental Research* **2004**, *28*, 1051.

252. Park, E. J.; Amatya, S.; Kim, M. S.; Park, J. H.; Seol, E.; Lee, H.; Shin, Y.-H.; Na, D. H. Long-acting injectable formulations of antipsychotic drugs for the treatment of schizophrenia. *Archives of Pharmacal Research* **2013**, *36*, 651.

253. Davis, J. M.; Metalon, L.; Watanabe, M. D.; Blake, L. Depot Antipsychotic Drugs. *Drugs* **1994**, *47*, 741.

254. Roese, E.; Bunjes, H. Drug release studies from lipid nanoparticles in physiological media by a new DSC method. *Journal of Controlled Release* **2017**, *256*, 92.

255. Nounou, M.; El-Khordagui, L. K.; Khalafallah, N. A.; Khalil, S. A. In vitro drug release of hydrophilic and hydrophobic drug entities from liposomal dispersions and gels. *Acta Pharmaceutica* **2006**, *56*, 311.

256. Washington, C. Drug release from microdisperse systems: a critical review. *International Journal of Pharmaceutics* **1990**, *58*, 1.

257. Fu, C.; Zhang, C.; Peng, H.; Han, F.; Baker, C.; Wu, Y.; Ta, H.; Whittaker, A. K. Enhanced Performance of Polymeric 19F MRI Contrast Agents through Incorporation of Highly Water-Soluble Monomer MSEA. *Macromolecules* **2018**, *51*, 5875.

258. Huque, F. T. T.; Jones, K.; Saunders, R. A.; Platts, J. A. Statistical and theoretical studies of fluorophilicity. *Journal of Fluorine Chemistry* **2002**, *115*, 119.

259. Maschke, M.; Alborzinia, H.; Lieb, M.; Wölfl, S.; Metzler-Nolte, N. Structure–Activity Relationship of Trifluoromethyl-Containing Metallocenes: Electrochemistry, Lipophilicity, Cytotoxicity, and ROS Production. *ChemMedChem* **2014**, *9*, 1188.

260. Filler, R.; Schure, R. M. Highly acidic perhalogenated alcohols. A new synthesis of perfluoro-tert-butyl alcohol. *The Journal of Organic Chemistry* **1967**, *32*, 1217.

261. Chang, I. S.; Price, J. T.; Tomlinson, A. J.; Willis, C. J. Studies on Fluorinated Vinylic and Aromatic Alcohols and Esters. *Canadian Journal of Chemistry* **1972**, *50*, 512.

262. Vuluga, D.; Legros, J.; Crousse, B.; Slawin, A. M. Z.; Laurence, C.; Nicolet, P.; Bonnet-Delpon, D. Influence of the Structure of Polyfluorinated Alcohols on Brønsted Acidity/Hydrogen-Bond Donor Ability and Consequences on the Promoter Effect. *The Journal of Organic Chemistry* **2011**, *76*, 1126.

263. Sobociková, M.; Štěpnička, P.; Ramella, D.; Kotora, M. Synthesis of 1-Alkanoyl-1'-(trifluoroacetyl)ferrocenes. *Collection of Czechoslovak Chemical Communications* **2006**, *71*, 190.

264. Sanders, R.; Mueller-Westerhoff, U. T. The lithiation of ferrocene and ruthenocene: a retraction and an improvement. *Journal of Organometallic Chemistry* **1996**, *512*, 219.

265. Gosselin, F.; O'Shea, P. D.; Roy, S.; Reamer, R. A.; Chen, C.-y.; Volante, R. P. Unprecedented Catalytic Asymmetric Reduction of N−H Imines. *Organic Letters* **2005**, *7*, 355.

266. Bouten, P. J. M.; Hertsen, D.; Vergaelen, M.; Monnery, B. D.; Boerman, M. A.; Goossens, H.; Catak, S.; van Hest, J. C. M.; Van Speybroeck, V.; Hoogenboom, R. Accelerated living cationic

ring-opening polymerization of a methyl ester functionalized 2-oxazoline monomer. *Polymer Chemistry* **2015**, *6*, 514.

267. Filippov, S. K.; Verbraeken, B.; Konarev, P. V.; Svergun, D. I.; Angelov, B.; Vishnevetskaya, N. S.; Papadakis, C. M.; Rogers, S.; Radulescu, A.; Courtin, T.; Martins, J. C.; Starovoytova, L.; Hrubý, M.; Štěpánek, P.; Kravchenko, V. S.; Potemkin, I. I.; Hoogenboom, R. Block and Gradient Copoly(2-oxazoline) Micelles: Strikingly Different on the Inside. *The Journal of Physical Chemistry Letters* **2017**, *8*, 3800.

268. Loukotová, L.; Švec, P.; Groborz, O.; Heizer, T.; Beneš, H.; Raabová, H.; Bělinová, T.; Herynek, V.; Hrubý, M. Direct Comparison of Analogous Amphiphilic Gradient and Block Polyoxazolines. *Macromolecules* **2021**.

269. Steckhan, E. In *Organic Electrochemistry*, 4th ed.; Lund, H., Hammerich, O., Speiser, B. Eds.; Dekker, 2001; pp 545.

270. Zotti, G.; Schiavon, G.; Zecchin, S.; Favretto, D. Dioxygen-decomposition of ferrocenium molecules in acetonitrile: The nature of the electrode-fouling films during ferrocene electrochemistry. *Journal of Electroanalytical Chemistry* **1998**, *456*, 217.

271. Tabbì, G.; Cassino, C.; Cavigiolio, G.; Colangelo, D.; Ghiglia, A.; Viano, I.; Osella, D. Water Stability and Cytotoxic Activity Relationship of a Series of Ferrocenium Derivatives. ESR Insights on the Radical Production during the Degradation Process. *Journal of Medicinal Chemistry* **2002**, *45*, 5786.

272. Zhang, J.; Ren, L.; Hardy, C. G.; Tang, C. Cobaltocenium-Containing Methacrylate Homopolymers, Block Copolymers, and Heterobimetallic Polymers via RAFT Polymerization. *Macromolecules* **2012**, *45*, 6857.

273. Hurvois, J. P.; Moinet, C. Reactivity of ferrocenium cations with molecular oxygen in polar organic solvents: Decomposition, redox reactions and stabilization. *Journal of Organometallic Chemistry* **2005**, *690*, 1829.

274. Prins, R.; Korswagen, A. R.; Kortbeek, A. G. T. G. Decomposition of the ferricenium cation by nucleophilic reagents. *Journal of Organometallic Chemistry* **1972**, *39*, 335.

275. Chen, W.-Y.; Alexandridis, P.; Su, C.-K.; Patrickios, C. S.; Hertler, W. R.; Hatton, T. A. Effect of Block Size and Sequence on the Micellization of ABC Triblock Methacrylic Polyampholytes. *Macromolecules* **1995**, *28*, 8604.

276. Cheng, Y.; Grigorieff, N.; Penczek, Pawel A.; Walz, T. A Primer to Single-Particle Cryo-Electron Microscopy. *Cell* **2015**, *161*, 438.

277. Franken, L. E.; Boekema, E. J.; Stuart, M. C. A. Transmission Electron Microscopy as a Tool for the Characterization of Soft Materials: Application and Interpretation. *Advanced Science* **2017**, *4*, 1600476.

278. Kumar, B.; Koul, S.; Khandrika, L.; Meacham, R. B.; Koul, H. K. Oxidative Stress Is Inherent in Prostate Cancer Cells and Is Required for Aggressive Phenotype. *Cancer Research* **2008**, *68*, 1777.

279. Gasser, G.; Ott, I.; Metzler-Nolte, N. Organometallic Anticancer Compounds. *Journal of Medicinal Chemistry* **2011**, *54*, 3.

280. Neuse, E. W. Macromolecular Ferrocene Compounds as Cancer Drug Models. *Journal of Inorganic and Organometallic Polymers and Materials* **2005**, *15*, 3.

281. Salmain, M.; Metzler-Nolte, N. Bioorganometallic Chemistry of Ferrocene. In *Ferrocenes*, Štěpnička, P. Ed.; John Wiley & Sons, 2008; pp 499.

282. Morrison, C. A.; Bone, S. F.; Rankin, D. W. H.; Robertson, H. E.; Parsons, S.; Coxall, R. A.; Fraser, S.; Howell, J. A. S.; Yates, P. C.; Fey, N. Conformational Properties of Substituted Ferrocenes: Experimental and Theoretical Studies of the Molecular Structures of 1,1'-Di-tert-butylferrocene and Isopropylferrocene. *Organometallics* **2001**, *20*, 2309.

283. Pell, A. J.; Pintacuda, G.; Grey, C. P. Paramagnetic NMR in solution and the solid state. *Progress in Nuclear Magnetic Resonance Spectroscopy* **2019**, *111*, 1.

284. Tanaka, K.; Kitamura, N.; Takahashi, Y.; Chujo, Y. Reversible signal regulation system of 19F NMR by redox reactions using a metal complex as a switching module. *Bioorganic & Medicinal Chemistry* **2009**, *17*, 3818.

285. Bergin, C. J.; Pauly, J. M.; Macovski, A. Lung parenchyma: projection reconstruction MR imaging. *Radiology* **1991**, *179*, 777.

286. Robson, M. D.; Gatehouse, P. D.; Bydder, M.; Bydder, G. M. Magnetic Resonance: An Introduction to Ultrashort TE (UTE) Imaging. *Journal of Computer Assisted Tomography* **2003**, *27*, 825.

287. Xing, L.; Blakemore, D. C.; Narayanan, A.; Unwalla, R.; Lovering, F.; Denny, R. A.; Zhou, H.; Bunnage, M. E. Fluorine in Drug Design: A Case Study with Fluoroanisoles. *ChemMedChem* **2015**, *10*, 715.

288. Zafrani, Y.; Yeffet, D.; Sod-Moriah, G.; Berliner, A.; Amir, D.; Marciano, D.; Gershonov, E.; Saphier, S. Difluoromethyl Bioisostere: Examining the "Lipophilic Hydrogen Bond Donor" Concept. *Journal of Medicinal Chemistry* **2017**, *60*, 797.

289. Hodgson, H. H. The Sandmeyer Reaction. *Chemical Reviews* **1947**, *40*, 251.

290. Clayden, J.; Greeves, N.; Warren, S. In *Organic Chemistry*, 2nd ed.; Oxford University Press, 2012; pp 520.

291. Loukotová, L.; Švec, P.; Groborz, O.; Heizer, T.; Beneš, H.; Raabová, H.; Bělinová, T.; Herynek, V.; Hrubý, M. Direct Comparison of Analogous Amphiphilic Gradient and Block Polyoxazolines. *Macromolecules* **2021**, *54*, 8182.

292. Witte, H.; Seeliger, W. Cyclische Imidsäureester aus Nitrilen und Aminoalkoholen. *Justus Liebigs Annalen der Chemie* **1974**, *1974*, 996.

293. Meyer, V. E.; Lowry, G. G. Integral and differential binary copolymerization equations. *Journal of Polymer Science Part A: General Papers* **1965**, *3*, 2843.

294. Hoogenboom, R.; Thijs, H. M. L.; Fijten, M. W. M.; van Lankvelt, B. M.; Schubert, U. S. One-pot synthesis of 2-phenyl-2-oxazoline-containing quasi-diblock copoly(2-oxazoline)s under microwave irradiation. *Journal of Polymer Science Part A: Polymer Chemistry* **2007**, *45*, 416.

295. Fijten, M. W. M.; Hoogenboom, R.; Schubert, U. S. Initiator effect on the cationic ring-opening copolymerization of 2-ethyl-2-oxazoline and 2-phenyl-2-oxazoline. *Journal of Polymer Science Part A: Polymer Chemistry* **2008**, *46*, 4804.

296. Blankenburg, J.; Wagner, M.; Frey, H. Well-Defined Multi-Amino-Functional and Stimuli-Responsive Poly(propylene oxide) by Crown Ether Assisted Anionic Ring-Opening Polymerization. *Macromolecules* **2017**, *50*, 8885.

297. Skeist, I. Copolymerization: the Composition Distribution Curve. *Journal of the American Chemical Society* **1946**, *68*, 1781.

298. Kagiya, T.; Matsuda, T.; Nakato, M.; Hirata, R. Polymerization of 2-Oxazolines. IV. The Structure and the Reactivity of 2-Substituted-2-oxazolines and Oxazolinium Perchlorates. *Journal of Macromolecular Science: Part A - Chemistry* **1972**, *6*, 1631.

299. Chen, Y.; Chen, H.; Feng, M.; Dong, Y. Amphiphilic gradient copolymers: Synthesis, self-assembly, and applications. *European Polymer Journal* **2016**, *85*, 489.

300. Rossi Sebastiano, M.; Doak, B. C.; Backlund, M.; Poongavanam, V.; Over, B.; Ermondi, G.; Caron, G.; Matsson, P.; Kihlberg, J. Impact of Dynamically Exposed Polarity on Permeability and Solubility of Chameleonic Drugs Beyond the Rule of 5. *Journal of Medicinal Chemistry* **2018**, *61*, 4189.

301. Chiu, P.-L.; Kelly, D. F.; Walz, T. The use of trehalose in the preparation of specimens for molecular electron microscopy. *Micron* **2011**, *42*, 762.

302. Tanford, C. *The Hydrophobic Effect: Formation of Micelles and Biological Membranes*; Wiley, 1973.

303. Manohar, C.; Narayanan, J. Average packing factor approach for designing micelles, vesicles and gel phases in mixed surfactant systems. *Colloids and Surfaces A: Physicochemical and Engineering Aspects* **2012**, *403*, 129.